Target and Laser Pulse Optimization for Laser-Driven Ion Acceleration

Permogorov, Alexander

2021

Document Version:
Publisher's PDF, also known as Version of record

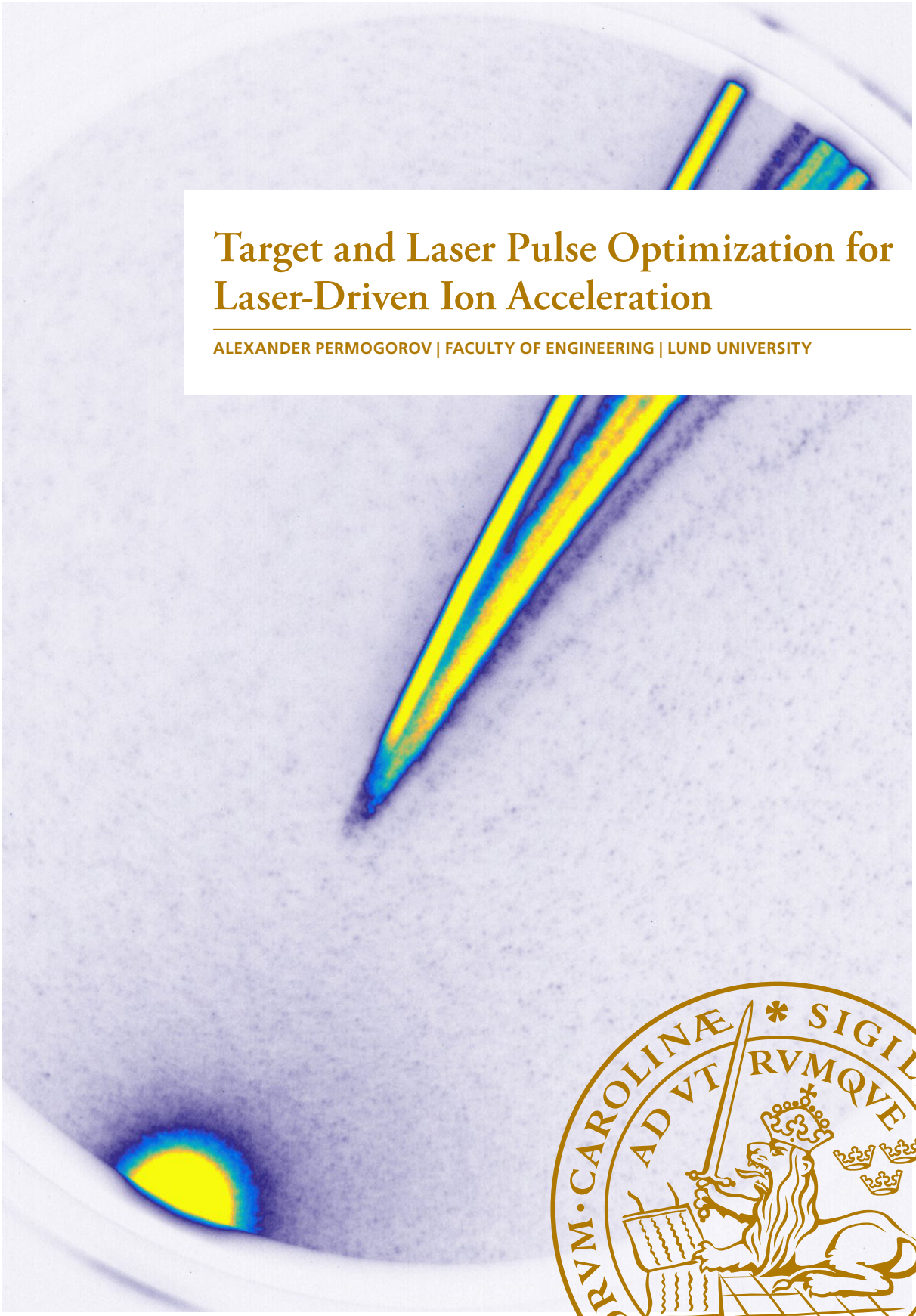

Target and Laser Pulse Optimization for Laser-Driven Ion Acceleration

ALEXANDER PERMOGOROV | FACULTY OF ENGINEERING | LUND UNIVERSITY

Printed by Media-Tryck, Lund 2021 NORDIC SWAN ECOLABEL 3041 0903

LUND UNIVERSITY
Faculty of Engineering, LTH
Department of Physics
Divison of Atomic Physics

ISBN: 978-91-7895-989-1 (print)
ISBN: 978-91-7895-990-7 (pdf)
ISSN 0281-2762
Lund Reports on Atomic Physics, LRAP 573 (2021)

Target and Laser Pulse Optimization for Laser-Driven Ion Acceleration

by Alexander Permogorov

Doctoral Dissertation
2021

LUND
UNIVERSITY

Cover illustration front: The first trace obtained with the Lund TPS ©Alexander Permogorov 2021

Faculty of Engineering, Department of Physics

ISBN: 978-91-7895-989-1 (print)
ISBN: 978-91-7895-990-7 (pdf)
ISSN: 0281-2762
Lund Reports on Atomic Physics, LRAP 573 (2021)

Printed in Sweden by Media-Tryck, Lund University, Lund 2021

Media-Tryck is a Nordic Swan Ecolabel certified provider of printed material. Read more about our environmental work at www.mediatryck.lu.se

MADE IN SWEDEN

Abstract

The research presented in this thesis is primarily focused on experimental investigations of laser-driven ion acceleration from solid targets via the target normal sheath acceleration mechanism. In particular, ways of optimizing the absorption of the laser pulse energy by free plasma electrons in the target, or modifying the shape of the accelerating electron sheath were addressed. The aim of this work was to increase the efficiency, and maximum proton energy that could be obtained with a given laser system, and to reduce the divergence of the beams of accelerated protons.

The shape of the electrostatic sheath was indirectly influenced by using laser micromachining to modify the front surface of the target, on which the laser pulse is incident. The absorption of the laser pulse was enhanced by either placing nanostructures, such as nanowires, foams, or nanoholes, on the front side of the foil target, or by manipulating the temporal profile of the ultrafast part of the laser pulse before its interaction with an ultrathin target.

Such studies require precise control and characterization of the laser pulse driving the acceleration. It is especially important to ensure the survival of the target before the arrival of the main laser pulse by using a laser pulse with very high temporal contrast. A double plasma mirror (DPM) was designed and implemented for this purpose. Design considerations and the optimization of the performance of the DPM, which is now used routinely at the Lund High-Power Laser Facility during laser–solid interaction studies, are discussed. This discussion is centered on the laser pulse fluence (and consequently peak intensity) on the reflective substrates of the DPM, and its effects on the spectral and spatial properties of the temporally cleaned laser pulse.

Sufficiently high temporal contrast was achieved, and an increase was seen in the maximum proton kinetic energy when using targets with nanowire and foam structures on the surface. The temporal contrast was also found to be sufficient for efficient ion acceleration from ultrathin targets with a thickness down to 10 nm.

When an ultrafast laser pulse interacts with an ultrathin foil, the temporal shape of the

electric field of the pulse (i.e. the pulse chirp) affects the laser–solid interaction, and a slightly positively chirped pulse was found to increase the maximum kinetic energy of the accelerated protons. In order to obtain information on the electric field of the high-intensity part of the laser pulse, part of the laser beam was intercepted immediately before being focused onto the target, and characterized by single-shot frequency-resolved optical gating (FROG) technique.

Laser–solid interactions at very high intensities are known to have shot-to-shot instabilities, motivating the use of single-shot diagnostics. As part of this work, a comprehensive range of simultaneous interaction diagnostic tools was implemented. The ion spectra in the forward direction were recorded using a Thomson parabola spectrometer, and in the backward direction with a magnetic dipole spectrometer. The intensities of the reflected and transmitted fractions of the laser pulse were also recorded on a shot-to-shot basis. In addition, a proton spatial profile monitor could be inserted to spatially characterize the proton bunch accelerated in the forward direction.

Popular Scientific Summary

Fast-moving charged particles, such as protons or other ions, are used in many applications, both in science and everyday life. Examples include material sciences, to determine properties of various compounds, particle physics, to study element transmutation, for radiotherapy in tumor treatment, and potentially in the field of fusion energy.

In order to generate these fast-moving particles, particle accelerators are required. Fundamentally, all particle accelerators are based on the same principle, – namely transferring the energy of an electric field into kinetic energy of the charged particles. Thus, the higher the electric field, the faster the particles can be accelerated.

Conventional proton accelerators that use either electrostatic or radio-frequency fields would have to be extremely large to achieve high proton energies since the construction materials can only withstand a certain strength of electric field, which can usually not exceed a hundred million volts (100 MV) per meter.

Advances in laser technology have made it possible to use a very short, tightly focused laser pulse (almost a millionth of billionth of a second long, or a few tens of femtoseconds) to generate electric fields that are at least a thousand times stronger. One example of such a laser is the Terawatt Laser at the Lund High-Power Laser Facility that was used for the work presented in this thesis.

But how can one transfer the electric field energy from a laser pulse to the kinetic energy of the protons? It is not possible to do that directly. The electric field of the laser changes its direction hundreds of trillions times a second, and even protons are too heavy to keep up with such rapid changes. Electrons, however, are light enough to be moved directly by the laser field and can be used as a mediator to accelerate protons.

At first, the laser is directed onto the front of a thin solid target foil, causing its ionization and leading to the formation of a plasma. This is a type of ionized matter consisting essentially of a mixture of positive ions and negative electrons, which can sustain those extremely high electric fields on the timescale of the laser pulse. Since the atoms in a solid are densely

packed, the resulting plasma also has a high density and partly reflects the laser pulse. The laser is aligned such that a component of the electric field that points into the target upon reflection. This component of the electric field is absorbed, transferring some of the energy of the laser pulse to the electrons, making their kinetic energy high. These high energy (hot) electrons travel through the target at almost the speed of light, and when they exit the target from the back they drag and accelerate protons and other positive ions with them, affording them with high velocities.

The field of laser-driven ion acceleration is still young, and this approach cannot yet be used to achieve the energies possible with conventional accelerators. Many significant challenges remain to be overcome such as increasing the speed of the ions and decreasing the spatial divergence of the ion beam.

The work presented in this thesis is concerned with one of the ways of achieving those goals. This involved changes in the the way the laser pulse interacts with the front surface of the target foil, in order to increase the fraction of the laser pulse that is absorbed. This was done by either changing the properties of the laser pulse itself, or by placing different structures on the front surface or inside the target inside the interaction region.

It was found that the divergence of the proton beam could be dramatically reduced when pits were 'drilled' in the target using a weaker laser beam. It was also found that growing a nanoscale structure on the front of the target could trap the laser pulse, resulting in a larger fraction of the pulse being absorbed. However, it was also found that some nanostructures did not behave as predicted by theory when investigated under realistic experimental conditions.

Several changes were made to the laser pulse itself, for example, the contrast of the pulse. The contrast is the ratio between the peak of the laser pulse and the light 'pedestal' preceding it and originating from the laser system itself. Increasing the contrast makes more electrons in the target available to absorb the laser light. The shape of the most intense part of the pulse was also modified. This led to differences in the amount of the laser pulse absorbed, and thus in the speed of the accelerated protons.

List of Publications

This thesis is based on the following publications, referred to in the text by their Roman numerals:

I **Influence of micromachined targets on laser accelerated proton beam profiles**

M. Dalui, A. Permogorov, H. Pahl, A. Persson, and C.-G. Wahlström
Plasma Physics and Controlled Fusion **60** 035014 (2018)

II **Enhanced laser-driven proton acceleration using nanowire targets**

S. Vallières, M. Salvadori, A. Permogorov, G. Cantono, K. Svendsen, Z. Chen, S. Sun, F. Consoli, E. d'Humières, C.-G. Wahlström and P. Antici
Scientific Reports 11:2226 (2021)

III **Laser-driven proton acceleration from ultrathin foils with nanoholes**

G. Cantono, A. Permogorov, J. Ferri, E. Smetanina, A. Dmitriev, A. Persson, T. Fülöp, and C.-G. Wahlström
Scientific Reports 11:5006 (2021)

IV **Effects of pulse chirp on laser-driven proton acceleration**

A. Permogorov, G. Cantono, D. Guenot, A. Persson and C.-G. Wahlström
Manuscript in preparation

Contents

Chapter 1

Introduction

Moving charged particles have been widely used in scientific applications since the famous Rutherford experiment, more than a century ago, where alpha particles from a radioactive source were used, and the first cathode ray tubes. They are used in materials science to characterize and modify the properties of matter that cannot be investigated using techniques that rely on photons. Some of these applications include studies of the structure and composition of solids, using techniques such as electron microscopy and electron diffraction, or the modification of materials my bombarding them with ions that are either deposited in the material (ion implantation) or used to precisely remove part of the sample (known as ion milling).

The applications mentioned above differ considerably, but their common feature is that the particle kinetic energies at which they operate are moderate. particles with higher kinetic energy can be used for a manifold of other applications, such as particle-induced X-ray emission [1], fast ignition in laser-driven nuclear fusion [2], radiation therapy of cancer tumors [3], all of which drove the development of particle accelerators that emerged in the middle of the twentieth century.

Particle accelerators convert the energy contained in electric fields into the kinetic energy of particles. The amount of energy transferred to the particles from the electric field is proportional to the strength of the field and the length of the acceleration region. In conventional accelerators, the electric field is created by applying high voltages to electrodes or by using radio-frequency cavities. The maximum strength of the electric fields in such approaches is limited to fields on the order of tens of MV/m, since stronger fields cause dielectric breakdown of the materials used for accelerator construction. Therefore, in order to obtain higher particle energies the length of the accelerator has to be increased, which increases the cost and complexity of the apparatus. For example, the length of the linear

proton accelerator at the European Spallation Source in Lund, accelerating protons to 2 GeV, is five hundred meters. Plasmas, on the other hand, can sustain much higher electric fields for a finite time, which makes them good candidates as a particle acceleration medium.

Very strong electric fields can now be produced using high-intensity lasers. This has been made possible by advances in laser technology such as chirped pulse amplification (CPA) [4], as illustrated in Figure 1.1. In this technique, short pulses (usually a few tens of femtoseconds) are stretched in time, and these stretched pulses are then amplified. The long duration of the pulses at this stage allows for strong amplification without reaching an intensity that damages the components of the laser system. Finally, the pulses are compressed back to their original duration, leading to very high peak power of the laser pulses [5, 6, 7], and consequently remarkably high intensities when the laser pulses are focused.

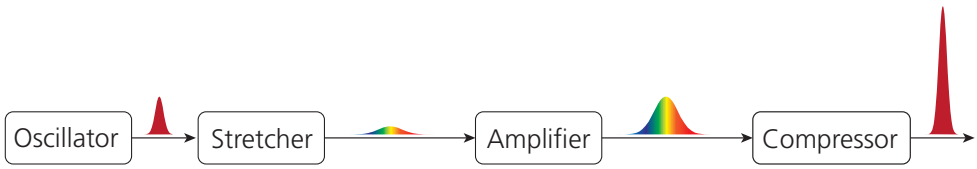

Figure 1.1: Schematic illustration of the chirped pulse amplification process.

When such a focused laser pulse interacts with a medium, it almost immediately ionizes it (see Section 2.1.3), and the major part of the pulse thus interacts with a plasma, as described in Section 2.2. Depending on the initial density of the medium, the laser can propagate through the resulting plasma (in the case of an underdense plasma), or be reflected from it (in an overdense plasma).

If the density is low, the propagating laser pulse can excite longitudinal waves in the plasma behind the laser pulse, which in turn can be used for electron acceleration. This mechanism is called laser wakefield acceleration [8, 9], and can produce electron beams, with kinetic energies of up a few GeV over distances of only a few tens of centimeters [10]. In the case of a target with a high density, such as a solid, the laser pulse is reflected from the target while some of the energy is transferred to the electrons forming the overdense plasma. If the target is sufficiently thin (usually not exceeding a few tens of micrometers), the hot electrons can form an electrostatic sheath and transfer their kinetic energy to ions, accelerating them in the direction of the local target normal [11, 12] to energies up to a few tens of MeV, increasing with the power of the laser system used [13]. One of the highest cut-off energies reported is approaching 100 MeV [14, 15]. This mechanism is called target-normal sheath acceleration (see Section 2.3.1), and is the main theme of the work presented in this thesis.

Beams of ions accelerated using TNSA, and protons in particular, have remarkable properties. Firstly, the accelerated protons form a bunch that has short duration (but is being

temporally stretched while propagating in vacuum). Proton bunches as short as 6 ps have been reported [16]. Secondly, although the beams are divergent, they exhibit spectacular laminarity [17], exceeding that of beams from conventional accelerators. These properties make TNSA protons very appealing for applications in, for example, time-resolved radiography [18, 19].

Since the discovery of TNSA over two decades ago, considerable effort has been devoted to increasing the maximum proton energy and improving the spatial properties of the accelerated proton bunches. The properties of the accelerated ions depend strongly on the energetic and spatial properties of the electron sheath, accelerating them. This thesis presents experimental studies of TNSA, the main goal of which was to enhance the properties of the accelerated protons by either increasing the amount of energy transferred from the laser to the electrons (i.e. absorption enhancement) by introducing nanometer-scale structures on the front surface of the target (**Papers II – III**) or by chirping the laser pulse incident on an ultrathin target (10 nm). **Paper IV**). **Paper I** discusses restructuring of the target surface (laser micromachining) to reduce the divergence of the ion beam.

The theory of ultrafast laser pulses, plasmas, and their interaction is introduced briefly in Chapter 2. This chapter also explains the basics of laser pulse absorption in an overdense plasma, and includes an overview of the TNSA mechanism and the influence of the electron sheath on the spatial properties of the accelerated protons.

The experimental studies described in **Papers II – IV** rely on precise control of the temporal properties of the laser pulse to ensure the survival of the target until the arrival of the main (the most intense) part of the laser pulse. Chapter 3 provides a description of the methods and equipment used to characterize and manipulate the temporal profile of laser pulses, such as the temporal contrast and the chirp of the intense ultrafast pulse.

In order to characterize the interaction of the laser pulse with the overdense target, diagnostic tools are needed, including proton and ion spectrometers, spatial profilers, and laser pulse reflectivity measurement devices. Chapter 4 describes the principal components of the interaction diagnostic tools that were routinely used in the studies described in this work. Emphasis is placed on the ion spectrometer, known as the Thomson parabola spectrometer, which was designed, constructed and implemented by the author as part of this work.

Chapter 5 is devoted to the experimental results and provides an overview of the studies presented in detail in the papers. The results of two unpublished studies on targets with front surface structures, such as black silicon and foam targets, are also presented. Finally, Chapter 6 presents the conclusions of this work and together with an outlook on potential developments in the field of laser-driven ion acceleration.

Chapter 2

Theoretical Background

This chapter starts with an overview of the electromagnetic wave properties of a laser pulse, the fundamental ways of describing a laser pulse, and the main properties of the plasma state of matter. The interaction of a laser pulse with matter is then discussed, starting with the ionization of the medium, through the interaction of free electrons with the field of an ultra-intense laser pulse, such as single–electron motion and electron heating, and finally a description of the basics of the interaction between the electrons and plasma ions.

2.1 Laser Pulses

Any electromagnetic field propagating in vacuum must satisfy Maxwell's equations:

$$\begin{cases} \nabla \cdot \mathbf{E}(\mathbf{r}, t) = 0 \\ \nabla \cdot \mathbf{B}(\mathbf{r}, t) = 0 \\ \nabla \times \mathbf{E} = -\dfrac{\partial \mathbf{B}(\mathbf{r}, t)}{\partial t} \\ \nabla \times \mathbf{B} = \mu_0 \epsilon_0 \dfrac{\partial \mathbf{E}(\mathbf{r}, t)}{\partial t} \end{cases} \tag{2.1}$$

The simplest solution to this system of equations is a plane wave, mathematically described in complex notation as:

$$\mathbf{E}(r, t) = \mathbf{E}_0 e^{-i(\omega t - \mathbf{k}\cdot\mathbf{r})}, \tag{2.2}$$

where $\mathbf{k}$ is the wavevector, given by $k = \omega/c$, and the observed electric field is the real part of Equation 2.2. However, a plane wave is infinite temporally and spatially, so it cannot provide an accurate description of a laser pulse.

2.1.1 Gaussian Laser Pulses

A laser pulse is not a plane wave as it is finite in time, and its profile can be described by a complex temporal envelope. A Gaussian shape is often used to describe such an envelope (see Figure 2.1a), and can be written as:

$$\mathbf{E}(r,t) = \mathbf{E}_0(t)e^{-t^2/\tau^2}e^{-i(\omega t - \mathbf{k}\cdot\mathbf{r})}, \tag{2.3}$$

where $(\omega t - \mathbf{k}\cdot\mathbf{r}) = \phi(t)$ is the temporal phase of the pulse and τ is the time constant. For a Gaussian pulse it is convenient to introduce the full width at half maximum (FWHM) time duration $\tau_{FWHM} = 1.18\tau$.

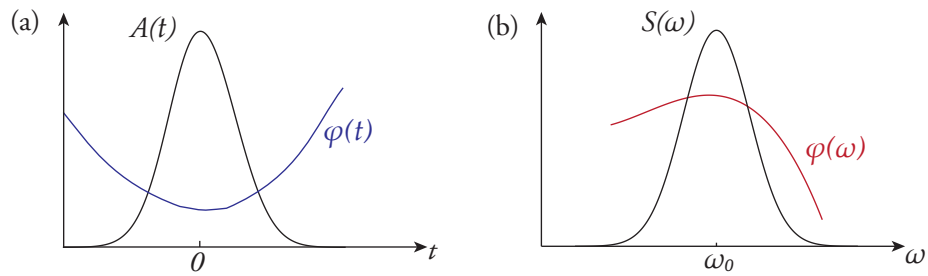

Figure 2.1: Temporal (a) and spectral (b) representation of an ultrafast pulse with arbitrary spectral and corresponding temporal phase

A Fourier transform of such an envelope will result in the complex spectrum of the pulse (Figure 2.1b), given as:

$$S(\omega) = S_{\omega_0}e^{-(\omega-\omega_0)^2/\Delta\omega^2}e^{-i\phi(\omega)}, \tag{2.4}$$

$\phi(\omega)$ being the spectral phase, ω_0 the central angular frequency, and $\Delta\omega$ the spectral FWHM. For a Gaussian pulse the relation $\tau_{FWHM}\Delta\omega = 2\pi \cdot 0.44$ holds.

Usually in an experiment one has a very limited control of the pulse spectral amplitude, but a much greater degree of freedom with the spectral phase of the pulse. It is therefore convenient to discuss how changes in the spectral phase affect the temporal properties of the pulse.

Any arbitrary spectral phase $\phi(\omega)$ can be Taylor–expanded to give a polynomial approximation around the central frequency, ω_0, as expressed below.

$$\phi(\omega) = \phi_0 + \frac{\phi(\omega)'}{1!}(\omega - \omega_0) + \frac{\phi(\omega)''}{2!}(\omega - \omega_0)^2 + \frac{\phi(\omega)'''}{3!}(\omega - \omega_0)^3 + \ldots \quad (2.5)$$

The first four terms of the expansion are enough for a simple discussion of the effects of the spectral phase of the pulse. When $\phi(\omega)$ is constant, the pulse is called 'transform-limited', and is the shortest possible for a given spectrum.

The term ϕ_0 is a constant and has no effect of the pulse in the temporal domain. The term ϕ' is the group delay, and in the temporal domain means a shift of the whole laser pulse in time. The third term, ϕ'', is the group velocity dispersion (GVD). When it is non–zero, the pulse in the temporal domain is chirped. This means that not only the pulse duration increases, but the frequency of the pulse changes with time. If GVD < 0 the pulse is positively chirped, and its instantaneous frequency increases with time. For the opposite case the chirp is negative, and the instantaneous frequency decreases. The last term in Equation 2.5, ϕ''', is called the third order dispersion (TOD) and in the temporal domain corresponds to an asymmetry of the pulse.

Since the laser pulse is confined in time and carries a finite amount of energy, E_l, it is possible to introduce the instantaneous power $P(t)$ and the peak power P_0. The instantaneous power can be obtained by integrating the pulse over time so that:

$$E_l = \int_{-\infty}^{+\infty} P(t)dt, \quad (2.6)$$

and the peak power is calculated simply as $P_0 = P(0)$.

2.1.2 Gaussian Beams

A laser pulse is not only confined in time, but also in space. The spatial distribution of the laser pulse is mostly determined by the design of the oscillator cavity, which is commonly operated in the fundamental transverse mode, and can be described by a Gaussian function. If we consider a laser beam propagating in the z direction and having a rotational symmetry with respect to the propagation axis, with $r = \sqrt{x^2 + y^2}$ being the radial coordinate, the spatial transverse envelope of the pulse can be written in terms of the complex amplitude as

$$\mathbf{E}(r,z) = \mathbf{E}_0 \frac{w_0}{w(z)} \exp\left(-\frac{r^2}{w(z)^2}\right) \exp\left(-ikz - ik\frac{x^2}{2R(z)} + i\zeta(z)\right). \tag{2.7}$$

The transverse electric field distribution of the beam is a Gaussian function at any point along the propagation axis, and the beam radius, $w(z)$, is defined at the point where the amplitude of the envelope has decreased by a factor of e compared to its on-axis value. $R(z)$ is the wavefront curvature, which changes along the propagation direction, and $\zeta(z)$ is the Gouy phase.

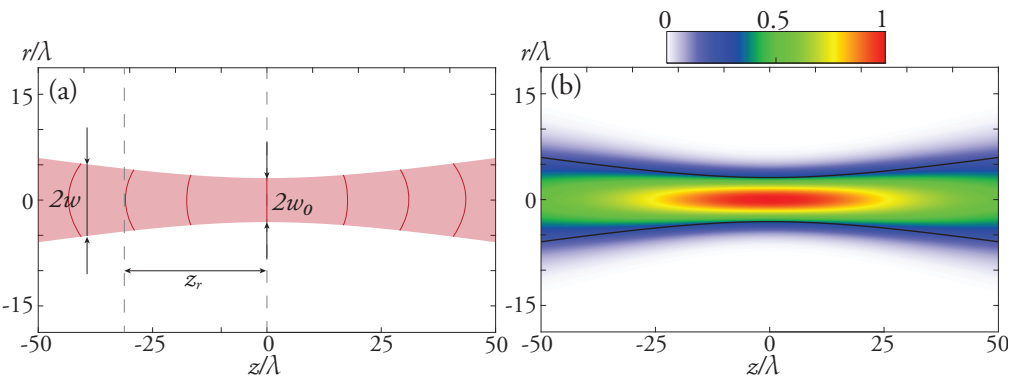

Figure 2.2: Wavefronts (a) and normalized amplitude (b) of a Gaussian beam.

Figure 2.2a shows the wavefronts of a Gaussian beam. One can see that at the beam width is minimum at the focal plane ($z = 0$) and the wavefront is flat. This is called the beam waist and is denoted w_0. Away from the focal plane the wavefront becomes curved, and the curvature is given by the radius of curvature $R(z) = z(1 + (z_r/z)^2)$ and the Gouy phase $\zeta(z) = \tan^{-1}(z/z_r)$ (see Equation 2.7). The parameter z_r is called the Rayleigh range and defines the distance from the focal plane at which the beam width has increased by a factor of $\sqrt{2}$ compared to the beam waist.

Since the laser pulse is confined in space, it makes sense to introduce the quantity of power per unit area, i.e. the intensity, so that $I(x,y) = \sqrt{\frac{\mu_0}{\epsilon_0}}|\mathbf{E}(x,y)|^2$. The peak power obtained from Equation 2.6 can be used to obtain the peak intensity distribution, expressed as:

$$I(r,z,t) = \frac{2P(t)}{\pi w(z)^2} \exp\left(-\frac{2r^2}{w(z)^2}\right) \tag{2.8}$$

with peak intensity $I_0 = 2P_0/\pi w_0^2$.

It can be seen from this equation that the intensity of an ultrashort pulse changes in time and space. Integrating the intensity over space results into the instantaneous power of the laser pulse. Integrating the intensity over time results in a metric Γ referred to as the fluence of the laser pulse, describing the amount of energy the laser pulse carries per unit area.

2.1.3 Ionization

Ionization can take place through several different mechanisms, as illustrated in Figure 2.3.

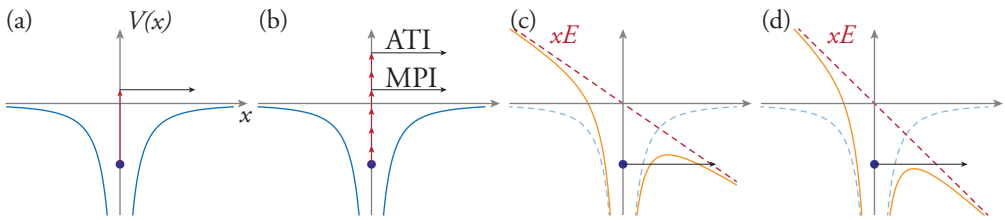

Figure 2.3: Different ionization mechanisms: *(a)* single photon ionization, *(b)* Multi-Photon and Above Threshold Ionization, *(c) tunneling ionization* and *(d)* over-the-barrier ionization

The simplest ionization mechanism is perhaps the single–photon ionization, as illustrated in Figure 2.3a. In this case, a photon with energy $\hbar\omega$ being equal to, or greater than, the electron binding energy can transfer its energy to the electron and remove it from the atom. This process usually requires photons with a fairly high energy. For example, the binding energy of a hydrogen atom is 13.6 eV, and the corresponding longest wavelength capable of ionizing it is thus approximately 91 nm. A similar wavelength is required to create a C^{1+} ion, but in order to create a C^{6+} ion from a C^{5+} ion, a photon with an energy of 490 eV is needed, which corresponds to a wavelength of 2.5 nm or shorter. Such short wavelengths are found in the soft X-ray spectral region.

However, if the intensity of the incident light is sufficiently high, multiple photons of lower energy can be absorbed and the electron can overcome the binding energy via virtual states. The simplest case of this is multiphoton ionization (MPI), as shown in Figure 2.3b [20]. The electron can absorb even more photons than needed to just overcome the binding energy and thus gain kinetic energy equal to the excess photon energy absorbed. This phenomenon is called above–threshold ionization (ATI)(Figure 2.3b)[21]. It has been shown experimentally that MPI and ATI process are dominant at intensities below 10^{13} W/cm^2 [22].

When the laser intensity is increased further, the electric field of the laser is strong enough to bend the electric potential of the atom sufficiently to cause a significant change in the potential barrier seen by the electron. Two cases are then possible depending on the strength

of the electric field. A strong external electric field (such as that of a laser pulse) can bend the Coulomb field of the atom so that the barrier seen by the electron becomes finite, and there is a probability that the electron will tunnel through the barrier (see Figure 2.3c). If the external electric field strength is further increased, the field of the atom can be bent so much that the potential barrier becomes lower than the bound state energy of the electron, and the electron can freely escape. This latter mechanism is called over-the-barrier ionization (OTBI) and is schematically illustrated in Figure 2.3*d*.

It is possible to calculate the electric field and thus appearance intensity of the laser pulse necessary to create an ion with a charge state of Z starting from an ion with a charge state of $Z-1$[23]:

$$I_{app} = \frac{c\left(E_{ion}^{Z-1\to Z}\right)^4}{128\pi Z^2 q_e^6} \approx 4\times 10^9 \left(\frac{E_{ion}^{Z-1\to Z}}{\text{eV}}\right)^4 Z^{-2}\left[\frac{\text{W}}{\text{cm}^2}\right], \tag{2.9}$$

where q_e is the charge of an electron. For example, a hydrogen atom will be ionized through OTBI at an intensity of 1.4×10^{14} W/cm^2, and a carbon atom can be fully ionized when the laser intensity reaches 6.4×10^{18} W/cm^2.

2.1.4 Plasma Density and Frequency

When a material is ionized, free electrons are created, and their number density can be denoted n_e. The electrons in a plasma are not stationary, and move with a thermal velocity $v_t = \sqrt{k_B T_e/m_e}$, m_e being the mass of the electron. When a plasma is subjected to a local electromagnetic disturbance, its effect will be completely screened by the electrons over a distance called the Debye length:

$$\lambda_D = \sqrt{\frac{\epsilon_0 k_B T_e}{q_e^2 n_e}}. \tag{2.10}$$

The electrons move with a finite velocity, and the shielding requires a time $t_D = \lambda_D/v_t$. Taking the reciprocal value of this time yields the expression for the classical plasma (electron) angular frequency:

$$\omega_p = \frac{1}{t_D} = \sqrt{\frac{q_e^2 n_e}{\epsilon_0 m_e}}. \tag{2.11}$$

In the relativistic case, the mass of the electron increases and becomes γm_e. The 'electron plasma frequency' is what is usually implied by the term 'plasma frequency'. However, the collective ion motion in the plasma can also be described by its own plasma frequency, defined as:

$$\omega_{pi} = \sqrt{\frac{q_e^2 n_i Z^2}{\epsilon_0 m_i}}, \tag{2.12}$$

where n_i is the ion number density, m_i is the mass of the ion, and Z is the charge state. The ion plasma frequency is much lower than the electron plasma frequency, but in some cases it is relevant, as discussed in Section 2.3.1.

It is worth noting that the plasma frequency depends only on the density of the plasma. The refractive index , η, of the plasma for an incident electromagnetic wave with angular frequency ω_0 can then be introduced:

$$\eta = \sqrt{1 - \frac{\omega_p^2}{\omega_0^2}} = \sqrt{1 - \frac{n_e}{n_c}}. \tag{2.13}$$

When $\omega_p < \omega_0$ the refractive index is real, positive and less than 1. This is the case of underdense plasma, and thus light can propagate in it. When $\omega_p > \omega_0$, then η is not a real number, and no light propagation is possible. This is the case in an overdense plasma, and light of any frequency $\omega_0 < \omega_p$ is reflected. For light of any given frequency there is a plasma density at which $\eta = 0$ and $\omega_p = \omega_0$, and this density is called the critical plasma density and is defined as $n_c = \omega_0^2 m_e \epsilon_0 / q_e^2$. When the electrons in the plasma are relativistic, the critical density changes as $n_c \to \gamma n_c$, as further discussed in Section 2.4.

2.2 The Interaction of the Laser Pulse with Plasma

A short laser pulse can cause motion of the electrons in the plasma, but the ions have too much inertia to be affected to any significant degree by the rapidly oscillating electric field of the laser pulse. This section therefore focuses only on the interaction of laser radiation with the plasma electrons.

2.2.1 Electron Movement in the Laser Field

Plane Electromagnetic Wave

In the general case, the motion of an electron in an electromagnetic field is governed by the Lorentz force and the energy equation:

$$\frac{d\mathbf{p_e}}{dt} = -q_e(\mathbf{E} + \mathbf{v} \times \mathbf{B}), \qquad (2.14) \qquad\qquad \frac{d}{dt}(\gamma m_e c^2) = -q_e \mathbf{v} \cdot \mathbf{E}, \qquad (2.15)$$

where γ is the relativistic Lorentz factor. In the classical regime, when $v \ll c$ and $\gamma = 1$, the influence of the magnetic field of the electromagnetic wave is negligible, the electron motion is thus only affected by the electric field of the laser, and the equation of motion becomes simply

$$m_e \frac{d\mathbf{v}}{dt} = -q_e \mathbf{E}. \qquad (2.16)$$

This equation can easily be solved analytically, and the solution is an oscillatory motion of the electron in the polarization plane of the wave.

To solve the equation of motion in the relativistic case, it is useful to introduce the vector potential $\mathbf{A}$ of the electromagnetic field:

$$\begin{cases} \mathbf{E} = -\dfrac{\partial \mathbf{A}}{\partial t} \\ \mathbf{B} = \nabla \times \mathbf{A}. \end{cases} \qquad (2.17)$$

If we now consider a monochromatic plane wave propagating in the z direction and polarized in the x direction such that $\mathbf{A} = \hat{\mathbf{x}} A_0 \cos(-\omega_0 t + kz)$, Equation 2.14 can be written as a system of equations of motion independently for the coordinates employing the vector potential:

$$\begin{cases} \dfrac{dp_z}{dt} = -q_e v_x \dfrac{\partial A}{\partial z} \\ \dfrac{dp_x}{dt} = q_e \dfrac{\partial A}{\partial t} + q_e v_z \dfrac{\partial A}{\partial z} \end{cases} . \qquad (2.18)$$

The solution, in the frame of reference co-propagating with the light wavefront $\zeta = z - \omega_0 t/k$, is obtained for the momenta (Equation 2.19) and integration gives the parametric equations of the electron trajectories (Equation 2.20)

$$\begin{cases} p_z = \dfrac{m_e c a_0^2}{4}(1 + \cos 2k\zeta) \\ p_x = m_e c a_0 \cos k\zeta, \end{cases} \tag{2.19}$$

$$\begin{cases} z = \dfrac{c a_0^2}{4\omega_0}(k\zeta + \dfrac{1}{2}\sin 2k\zeta) \\ x = \dfrac{c a_0}{\omega_0}\sin k\zeta, \end{cases} \tag{2.20}$$

with a_0 being the normalized vector potential calculated from:

$$a_0 = \frac{q_e A_0}{m_e c} = \frac{q_e E}{m_e c \omega_0} = \sqrt{\frac{q_e^2}{2\pi^2 \epsilon_0 m_e^2 c^5}\lambda_0^2 I_0} \approx 0.86\lambda[\mu\text{m}]\sqrt{I_0[10^{18}\ \text{W/cm}^2]}. \tag{2.21}$$

The solution to Equation 2.20 is shown in Figure 2.4. It is important to note that for $a_0 = 4.5$, that corresponds to the intensity of approximately 5×10^{19} W/cm^2 at a wavelength of 800 nm, the electron excursion length in the direction of the electric field polarization can be almost 600 nm. While this value exceeds half the wavelength of the laser and implies, at first glance, that the electron is traveling faster than the speed of light, in reality the laser wavelength seen by the electron is redshifted since the electron is pushed forwards in the z direction, and there is no contradiction.

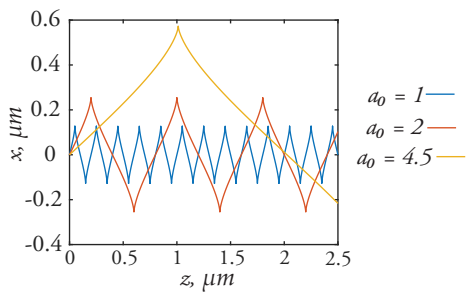

Figure 2.4: Electron trajectories in the laser field for selected values of a_0

Focused Beam and Ponderomotive Force

A tightly focused Gaussian laser beam, even despite having a flat wavefront, cannot be approximated by a plane wave since the amplitude of the electric field amplitude changes

transversely on a scale comparable to that of the wavelength of the laser. This means that if, during one half–cycle, an electron is displaced from a region close to the center of the beam, where the electric field (and thus the intensity) is high, to a region with lower intensity, during the next half–cycle, the restoring force will be lower, and the electron will not be completely driven back to its original position. This creates a net force pushing electrons away from regions of high intensity. This force is called the ponderomotive force and in the classical case, averaged over one light cycle, is expressed as [24]:

$$\mathbf{F_p} = -\frac{q^2}{2\omega_0^2 m}\nabla\langle\mathbf{E}^2\rangle \tag{2.22}$$

Closer inspection of this equation reveals that the ponderomotive force does not depend on the sign of the charge or the polarization direction of the laser pulse, and decreases as the mass of a particle increases. This means that electrons are affected significantly more by this force than protons and heavier ions. In quantitative terms, a proton is 1836 times heavier than an electron, and as the acceleration caused by the ponderomotive force is related to the square of the mass, an electron will be accelerated nearly 3.4 million times more than a proton. The force is also proportional to the gradient of the electric field, which means that the force is greater in the steep gradients found in tight beam foci.

The expression for the ponderomotive force given in Equation 2.22 is only valid for the non-relativistic case. In the relativistic case, the effect is the same qualitatively, and charged particles are pushed away from the region with higher intensity, but quantitatively it depends on the relativistic Lorentz factor γ, such that $\mathbf{F_p} \propto -\nabla\bar{\gamma}$ [25].

2.2.2 Hole Boring

Another important feature of a tightly focused high–power laser pulse is that it exerts significant light pressure on a surface that is reflecting or absorbing it. Assuming that the beam is incident on a surface at an angle θ, and that a fraction η_r of the beam is reflected, the light pressure on the target becomes:

$$P_L = (1+\eta_r)\frac{I}{c}\cos^2\theta, \tag{2.23}$$

where I is the intensity of the beam. For laser pulse intensities on the order of 5×10^{19} W/cm^2, such as those used in this work, the light pressure can exceed 10^{10} bar. If there is a pressure imbalance, and the reflective surface of the target cannot sustain the light pressure, the reflective surface will be pushed in the direction of laser pulse propagation, while the

bulk of the plasma will not move on the timescale of the laser pulse. In essence, the reflective layer is compressed into the target, and this effect is called hole boring.

When a relativistically intense ($a_0 > 1$) laser pulse hits a target with an exponential plasma density gradient of a characteristic length L at its front surface, it can only propagate until the layer of the plasma gradient with the corrected critical density of γn_c, where the Lorentz factor $\gamma = \sqrt{1 + (1 + \eta_r)a_0^2/2}$. At this point, the light is reflected and starts pushing the target electrons in front of it, locally increasing the plasma density at the reflection front. The resulting charge separation field causes the ions to follow the electrons, creating a 'hole' in the plasma that travels at the a velocity u_f. This process is illustrated schematically in Figure 2.5.

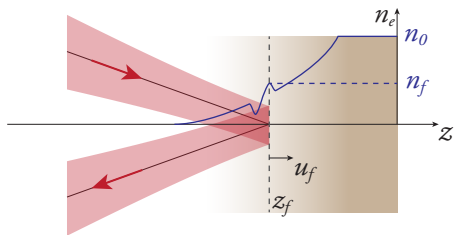

Figure 2.5: Schematic image of the hole boring mechanism. The blue curve shows the plasma density profile, including the disturbance at the pulse front, having a peak density n_f and moving under light pressure with the velocity of u_f

Assuming the light pressure is much greater than the plasma pressure, the pressure balance equation in the frame moving with the reflection front can be solved to obtain the velocity of the front [26]

$$\frac{u_f}{c} = \sqrt{\frac{(1+\eta_r)I_0 \cos\theta}{2\rho c}} \approx \sqrt{\frac{Zm}{M}\frac{n_c}{n_e}\frac{(1+\eta_r)\cos\theta}{4}\frac{I_{18}\lambda_\mu^2}{1.37}} \tag{2.24}$$

For example, if an 800 nm central wavelength laser pulse with an intensity $I_0 = 5 \times 10^{19}$ W/cm^2 is normally incident ($\theta = 0$) and totally reflected ($\eta_r = 1$) from a 'layer' of plasma with a density $n_0 = 3n_c$), the resulting velocity of the reflecting surface will be approximately 3% of the speed of light. For a laser pulse with a duration of 35 fs, the reflection front will have been pushed approximately 350 nm.

Although the approximation of a front moving with constant velocity described above agrees well with experiments [26] and simulations [27], it has been shown that hole boring not only gradually slows down [28], but in general the laser–plasma interaction depends non-linearly on the temporal and spatial properties of the laser pulse [29] and can only be roughly approximated by a simple analytical model.

2.2.3 Heating Mechanisms

The above description of the interactions of a laser pulse with an overdense plasma did not account for the absorption of light and did not depend on light polarization. In the context of ultra-intense laser interaction with an overdense plasma, the absorption of light translates into the transfer of laser energy to kinetic energy of the electrons forming the plasma. This energy transfer is commonly called electron heating. The exact mechanism of electron heating depends on the intensity of the laser pulse, the scale length of the plasma, the polarization of the laser, and its angle of incidence, and several different mechanisms often contribute to electron heating simultaneously.

Resonant Absorption

When a p–polarized laser pulse is obliquely incident at an angle θ onto a target surface with a long plasma gradient with a scale length L such that $n = n_0 \exp(-z/L)$, it can propagate through the underdense region, but starts turning away from the target due to the graded refractive index. The direction of laser pulse propagation becomes parallel to the target surface when it reaches a layer with a density of $n_t = n_c \cos^2\theta$, (see Figure 2.6). At this point, the electric field of the pulse is normal to the target (i.e. along the plasma gradient), and the evanescent wave reaches the critical layer of the plasma gradient.

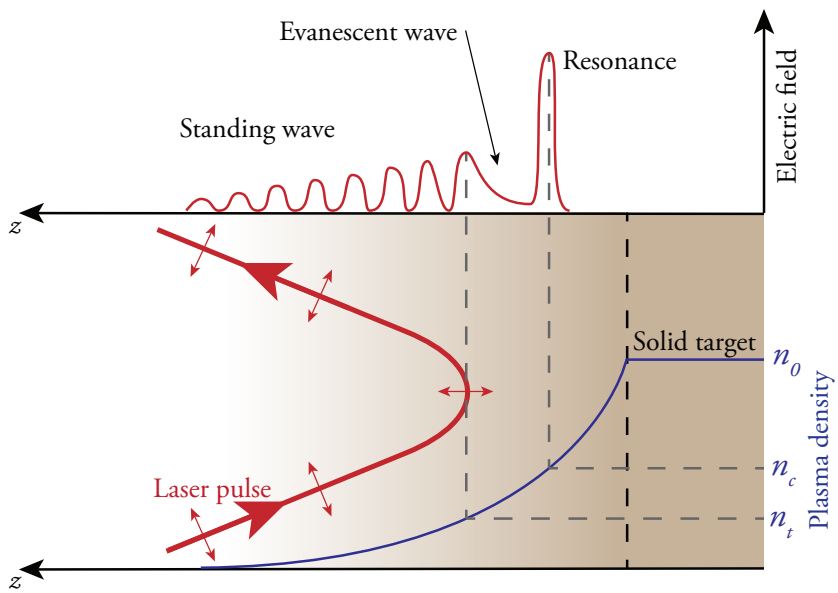

Figure 2.6: Schematic illustration of resonant absorption. n_0 is the solid plasma density, n_c is the critical density, and n_t is the 'turning point' density

Since the frequency of the laser is equal to the plasma frequency of the critical density layer, the evanescent wave resonantly drives this layer longitudinally, and the energy of this oscillation is transferred to other electrons through Landau damping [30] provided the electron temperature is sufficiently high, which was the case for all the studies presented in this thesis.

The temperature of the electrons can, in this case, be estimated as [31]:

$$k_B T_e = 100(I_{17}\lambda_\mu^2)^{1/3}[\text{keV}], \tag{2.25}$$

where I_{17} is the laser intensity normalized by 10^{17} W/cm^2 and λ_μ is the laser wavelength in µm.

When the incident pulse becomes relativistically intense ($a_0 > 1$), the critical layer density changes as $n_c \to \gamma n_c$, and thus the location of the resonant plasma layer also changes.

If a laser pulse interacts with an initially flat target, the fraction of the laser radiation absorbed, η_{ra}, depends on the wavelength of the laser, the front surface plasma scale length L, and the angle of incidence, θ, in a simple way [32]:

$$\eta_{ra} \approx 2.65\zeta^2 e^{-4\zeta^3/3}, \tag{2.26}$$

where $\zeta = (kL)^{1/3}\sin\theta$. For a given laser system the wavevector $k = 2\pi/\lambda$ is constant, so the above relation can be studied as a function of the angle of incidence, using only the plasma scale length as a parameter. The resulting absorption fraction curves for various scale lengths are plotted in Figure 2.7.

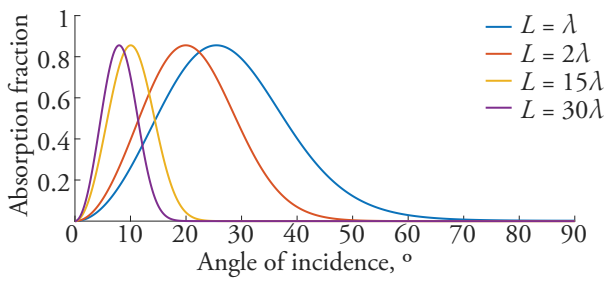

Figure 2.7: Solutions of Equation 2.26 for different values of the front surface plasma scale length

It can be seen from Figure 2.7 that the peak absorption remains at approximately 85% regardless of the scale length, while the optimal angle of incidence increases as the density gradient becomes steeper. The resonance absorption model can thus only be used for large

plasma gradient scale lengths. If the scale length L is smaller than the transverse electron excursion length in the laser field, the resonance breaks down, and other models must be used. In Section 2.2.1 the excursion length was calculated to be approximately 600 nm in the field of a focused laser pulse used in this work, which had a central wavelength of 800 nm, so the limit of the plasma scale length in the resonance absorption model is $L \approx \lambda$.

From an experimental point of view, a large plasma scale length corresponds to laser pulses with modest contrast, such as those used in **Paper I**. In this case, resonance absorption is believed to be the dominant mechanism of energy transfer from the laser to the plasma electrons. When the contrast of the laser pulse is higher, as was the case in **Papers II – IV**, other absorption mechanism are expected to dominate, and these will be discussed below.

Vacuum (Brunel) Heating

When the plasma gradient scale length on the front surface of the target is short ($L < v_{os}/\omega_0$ [33], v_{os} being the velocity obtained by the electron in the direction of laser pulse polarization), the p-polarized electric field of the laser can pull an electron from the surface of the target and eject it into vacuum during one half-cycle of the wave, and accelerate it back into the bulk of the target during the next half-cycle. The electron can then travel through the critical surface, becoming inaccessible to the laser field. A fraction of the electrons gain sufficient energy to completely leave the interaction area, but the rest remain electrostatically bound to the target and obtain a temperature given by [34]:

$$T_e \approx 7(I_{16}\lambda_\mu^2)^{1/3}[\mathrm{keV}], \tag{2.27}$$

and the fraction of absorbed light in the case of $a_0 \gg 1$ is:

$$\eta_a^{vb} = \frac{4\pi\alpha}{(\pi+\alpha)^2}, \tag{2.28}$$

where $\alpha = \sin^2\theta/\cos\theta$. Note that at very high laser intensities the fraction absorbed does not depend on the intensity of the light. To obtain a better picture of the dependence of the absorbed fraction on the angle of incidence, it is useful to plot as a function of the angle of incidence (Equation 2.28) as in Figure 2.8. In the ideal case described by the equation, the absorption can reach 100% at an incidence angle of $\theta = 73.06°$. However, in a realistic scenario, the absorption is lower [34].

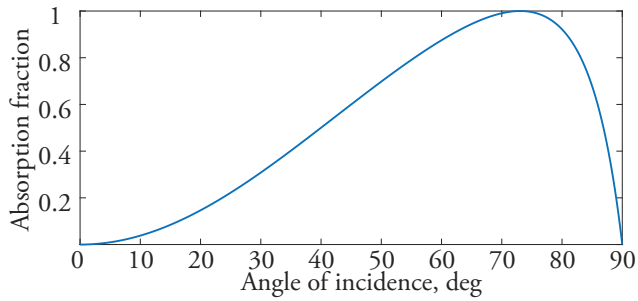

Figure 2.8: Fractional absorption via vacuum heating for intense laser pulses as a function of incidence angle

$\mathbf{j} \times \mathbf{B}$ Heating

One heating mechanism that does not require oblique incidence of a p-polarized wave and contributes to the heating at any angle of incidence and polarization (except for circular) is the $\mathbf{j} \times \mathbf{B}$ heating. Like the vacuum heating mechanism, it relies on a sharp ($L < \lambda$) plasma gradient on the front surface of the target. In this case the electrons are driven into the target by the $\mathbf{v} \times \mathbf{B}$ part of the Lorentz force (see Equation 2.14), acting in the direction of pulse propagation. This force is associated with the magnetic field of the incoming laser pulse and oscillates at twice the laser frequency[35]:

$$\mathbf{F}_{\mathbf{j}\times\mathbf{B}} = -\frac{q^2}{2\omega_0^2 m}\nabla\langle\mathbf{E}^2\rangle(1-\cos(2\omega_0 t)) = \mathbf{F}_{\mathbf{p}}(1-\cos(2\omega_0 t)). \tag{2.29}$$

This process is closely related to the hole boring effect (see Section 2.2.2), and it has been shown that the hot electrons are accelerated in a direction close to that of of the incident laser pulse [36, 37], and the temperature of the electrons is proportional to the relativistic ponderomotive potential.

$$T_e \approx mc^2(\gamma - 1) \approx 511\left(\sqrt{1 + \frac{I\lambda^2}{2.74\times10^{18}\mathrm{W/cm^2}\,\mu\mathrm{m}^2}} - 1\right)\,[\mathrm{keV}] \tag{2.30}$$

For an incident laser pulse with an intensity of 5×10^{19} W/cm^2 and a wavelength of 800 nm, the electrons will reach a temperature $k_B T_e$ of approximately 1.8 MeV as a result of $\mathbf{j} \times \mathbf{B}$ heating.

In a common scenario where the laser pulse has an oblique angle of incidence on the target surface, there is no analytical way of estimating the absorbed fraction of light. However, a

conversion of laser energy into kinetic energy of the electrons of 3% has been reported [36]. In order to estimate the full absorption in this case, the spatial distribution of the electrons is needed. A later study reported up to 70% absorption for intensities of approximately 5×10^{19} W/cm^2 in the case of thick (> 1 µm) targets and moderate contrast [38].

2.3 Ion Acceleration Mechanisms

While the electric field of the laser pulse is oscillating too fast to directly accelerate ions, due to their high inertia, ion acceleration can be mediated by the hot electrons that effectively rectify the laser field. When moving under the influence of the laser light, the electrons can create large quasi-static charge separation electric fields in the plasma, which can in turn accelerate the ions. There are a few different established mechanisms responsible for ion acceleration such as radiation pressure acceleration [39, 40], collisionless shock acceleration [41, 42], and breakout afterburner [43, 44]. In the scope of this work we will focus on the most mature and well-understood one, which is target–normal sheath acceleration.

2.3.1 Target–Normal Sheath Acceleration

Target normal sheath acceleration (TNSA) [45, 46] is one of the most studied laser-based ion acceleration mechanisms, and is the one investigated and optimized in this work. Simplistically, TNSA can be described in terms of four independent processes: ionization of the front surface of a solid target, heating of its electrons by the main part of the laser pulse, electron propagation through the bulk of the target, and the formation of an electron sheath field, which accelerates the ions.

Two scenarios are possible depending on the temporal contrast of the laser pulse (see Figures 2.9 and 2.10), which are fundamentally identical. In the case of a low temporal contrast laser pulse, the front surface of the target is ionized tens of picoseconds (or more) before the arrival of the main laser pulse, forming a long plasma gradient on the front surface of the target that prevents TNSA from occurring on that side, and limiting the minimal target thickness that can survive until the arrival of the main pulse to several micrometers. However, if the laser pulse has a sufficiently high temporal contrast, TNSA occurs on both sides of the target.

The case of low contrast laser pulse is illustrated in Figure 2.9. The initially solid target (a thin conducting foil in this work) is ionized on its front surface by the laser pulse pedestal, creating an expanding plasma (Figure 2.9a). The expansion velocity is very close to the ion speed of sound $c_s \approx \sqrt{Zk_BT_e/m_i}$, where Z is the ion charge state, T_e is the electron temperature, and m_i is the ion mass. The expansion velocity depends on the temporal

contrast of the pulse of a particular laser system, but it can reach hundreds of nm/ps for protons, and decreases for heavier ions.

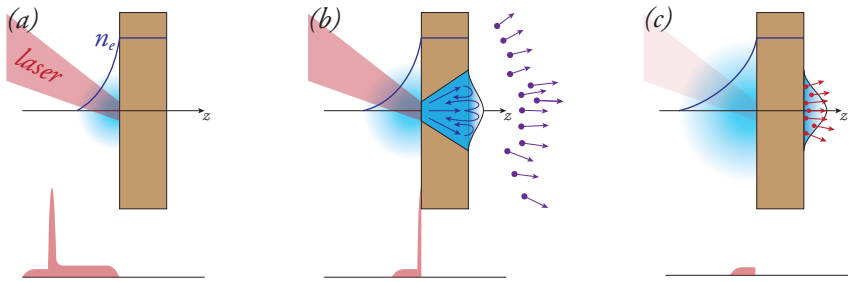

Figure 2.9: TNSA at low contrast. (a) Ionization and formation of the front surface expanding plasma by the pedestal of the pulse. (b) Heating of plasma electrons, their propagation through the target, and initial sheath formation. Electrons that leave the target are shown in purple. (b) Ion acceleration from the back surface of the target.

When the main part of the laser pulse arrives, it starts heating the electrons, primarily by the resonant absorption heating mechanism discussed above. Some electrons gain enough energy to escape the target, leaving it with a net positive charge, and these electrons play no further part in the processes related to TNSA. The rest of the electrons propagate through the target, but do not have enough momentum to overcome the resulting charge separation field and escape. These electrons form a layer in the vicinity of the initial target boundaries in vacuum, also known as a sheath (see Figure 2.9b). This transport is usually collisional, resulting in a divergent electron current [47]. The quasi-static electric field created by such a sheath can be on the order of TV/m, and is capable of field-ionizing any atoms on the rear surface of the target. Target foils that are not carefully prepared often have a contamination layer of water and hydrocarbons, which, when ionized, become the source of free protons.

Electrons arriving at the back of the target at a later time are reflected from the sheath, and propagate back to the front surface, where they can be reheated by the laser pulse (see Figure 2.9b). This process is called electron recirculation [48]. The electrons propagate through the target at relativistic velocities, so a rough estimate of the target thickness l that can support recirculation for a laser pulse of duration τ is $l \leqslant c\tau/2$. The laser pulses used in this work had a duration of 35 fs, and electron recirculation was thus expected to take place for targets thinner than approximately 5 µm.

The extremely high electron current inside the target (tens of megaamperes) leads to different effects related to the magnetic fields generated by the hot electrons and cold and hot return currents, such as magnetic reconnection [49] and electron beam filamentation [50], which are research topics on their own. These effects become less significant for thin

targets, motivating the use of ultra-high-contrast laser pulses that are able to efficiently interact with targets of subwavelength thicknesses, such as the studies presented in **Papers III – IV**.

One should note that the effects described above apply mainly to conducting targets. If the target is dielectric, there will be no free electrons in the conduction band that can support cold return currents, and the charge transport mechanism is even more complicated [51].

As soon as the electron sheath is formed on the rear surface of the target, it starts expanding and drags the ions formed on the back surface of the target with it in the target normal direction (see Figure 2.9c). Ions with a high charge-to-mass ratio (protons having the highest value) will be accelerated most rapidly, partly screening heavier ions from the accelerating field. Acceleration takes place as long as the sheath is sustained, which is closely related to the duration of the laser pulse.

In the case of low contrast, the layer of expanding plasma on the front surface of the target prevents efficient electron sheath formation there, and accelerated ions are mainly observed from the rear surface of the target. However, when the contrast is sufficiently high, a sheath is also formed on the front surface of the target, and this sheath will accelerate protons and other ions from the front surface in the direction opposite to the rear surface acceleration [52]. The case of the high–contrast TNSA is illustrated in Figure 2.10.

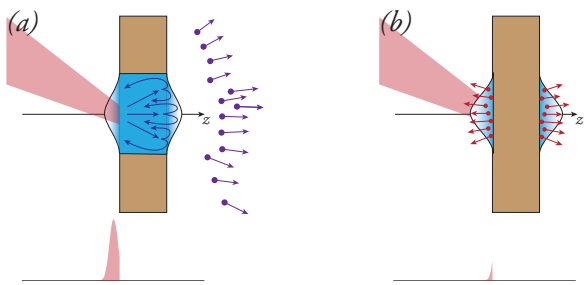

Figure 2.10: TNSA at high contrast. *(a)* Heating of the electrons, their propagation through the target, and initial sheath formation; *(b)* ion acceleration from the front and back surfaces of the target.

The expansion of the sheath can be crudely approximated as being isothermal [53], and the ion spectrum can thus be described by a Maxwell distribution:

$$\frac{dN_i}{dE} = \frac{n_{i0} t_{acc}}{\sqrt{2Em_i}} \exp\left(-\sqrt{\frac{2E}{Zk_B T_e}}\right), \tag{2.31}$$

having a cut-off ion energy that can be estimated from:

$$E_{max} \approx 2Zk_BT_e \left[\ln \left(\frac{2\omega_{pi}t_{acc}}{\sqrt{2\exp(1)}} \right) \right]^2, \tag{2.32}$$

where ω_{pi} is the ion plasma frequency.

The sheath temperature decreases during the acceleration process, and in order to account for this in the isothermal approximation the acceleration time is usually restricted to $t_{acc} = 1.3(\tau + 60[\text{fs}])$, where τ is the laser pulse duration [54].

From Equation 2.32 it can be seen that the cut-off energy is linearly proportional to the electron temperature, and increases slowly with the acceleration time, i.e. the laser pulse duration. By relating this expression to the heating mechanisms described in Section 2.2.3, it is possible to see that the cut-off energy scales with the normalized intensity ($I\lambda^2$) as $(I\lambda^2)^{1/3}$ when vacuum heating (Equation 2.27) or resonant absorption (Equation 2.25) are dominant, and as $(I\lambda^2)^{1/2}$ when the $\mathbf{j} \times \mathbf{B}$ mechanism is dominant (Equation 2.30). Such scaling laws are slow, and it is thus necessary to increase the conversion of the laser energy to the kinetic energy of the hot electrons.

In a real laser system, increasing the duration of the pulse inevitably leads to reduced intensity. It has been shown experimentally, using a laser system similar to the one used in this work, that for thick targets ($>$ 10 µm) and a high–contrast laser pulse there is an optimal laser pulse duration, longer than the transform–limited pulse of the laser system used [55, 56]. For thinner foil targets ($<$ 3 µm) the optimal pulse duration is usually the shortest possible [55]. Additionally, in a laser system based on chirped pulse amplification, increasing the pulse duration most commonly leads to a change in the pulse chirp, that may have other effects on the acceleration process. These possible effects were studied and are described in **Paper IV**.

The model discussed above is essentially one-dimensional, and does not account for the shape of the electron sheath (as illustrated in Figures 2.9 and 2.10). The curvature of the accelerating sheath directly affects the divergence of the accelerated ions, which can be as high as a few tens of degrees. The sheath is usually bell-shaped, and the highest target-normal accelerating electric fields are found close to the geometric center of the sheath. Therefore, in order to change the proton beam divergence, it is necessary to change the gradient of the accelerating electric field. This is commonly achieved by manipulating the laser beam profile on the target. For example, the proton beam divergence can be decreased by defocusing the laser on the target surface [57], using a speckle pattern of light on the target [58], or by using laser beams that have a singularity in the focus [59]. These methods cause an inevitable decrease of the intensity of the laser pulse on target for a fixed energy of a laser pulse, which leads to decreased proton cut-off energy. In **Paper I** we demonstrated a simple method to reduce the divergence of the proton beam without compromising the

cut-off energy.

2.4 Self-Induced (Relativistic) Transparency

The heating and acceleration mechanisms described above rely on the target being overdense. In this case $n_e > n_c$ and consequently $\omega_0 < \omega_p$, where ω_0 is the angular frequency of the laser. This means that the laser pulse cannot propagate through the plasma. However, when the plasma electrons are driven transversely by the extremely strong electric field of the laser, they quickly reach relativistic velocities, and their mass becomes γm_e. This leads to an effective decrease in the plasma frequency so that it becomes $\omega_p/\sqrt{\gamma}$. If the laser pulse intensity is sufficiently high, the electrons will move so fast that the effective plasma frequency will decrease to the extent that the plasma becomes transparent to the pulse. This phenomenon is known as the relativistic, or self-induced, transparency, and may have an important effect on the ion acceleration processes that are discussed in **Paper IV**.

In a realistic case with a finite laser pulse and complex target density profiles different portions of the laser pulse will interact with 'layers' of plasma that have different effective frequencies, complicating the analytical description of the effects. A very simple approximation of a threshold for relativistic transparency of $n_0 \leqslant \gamma n_c$ is not sufficiently accurate, and a slightly more complicated model is needed.

For a very thin target, with a non-relativistic electron density of $n_0 > n_c$ and a thickness l much smaller than the wavelength of the laser [60], one can derive an expression to estimate the intensity required to reach the onset of relativistic transparency. Such an assumption is reasonable if an ultrathin target is used, as in the experiments described in **Paper IV**.

The target is assumed to be irradiated by a plane monochromatic wave of wavelength λ, and a corresponding plasma critical density of n_c. To further simplify the analysis it was assumed that the electron motion caused by the electromagnetic wave occurred strictly along the target surface, thus restricting the laser pulse to be circularly polarized in order to suppress the $\mathbf{j} \times \mathbf{B}$ heating mechanism. The complete derivations are presented elsewhere [61], and they determine a simple expression for the determination of the onset of relativistic transparency:

$$a_0 \approx \pi \frac{n_0 l}{n_c \lambda}, \tag{2.33}$$

where a_0 is the normalized vector potential of the electromagnetic wave.

A few numerical estimates can help in understanding the intensities required to reach the onset of relativistic transparency for different target thicknesses. For example, we can con-

sider two carbon foils, both ionized to the C^{2+} state ($n_0 \approx 115 n_c$), having thicknesses of $l_1 = 100$ nm and $l_2 = 10$ nm, so they both satisfy the condition of $l \ll \lambda$. According to Equation 2.33, in the first case ($l_1 = 100$ nm) the target becomes transparent when $a_0 \approx 45$, while the thinner target only requires $a_0 \approx 4.5$. Equation 2.21 shows that $a_0 \propto \sqrt{I}$, and the peak intensity required for the 100 nm foil to become transparent is approximately 4×10^{21} W/cm^2, but 'only' 4×10^{19} W/cm^2 for the 10 nm foil, which is routinely accessible at Lund High-Power Laser Facility with a very high temporal contrast (see Section 3.3).

Chapter 3

Laser Pulse Characterization and Control

A powerful laser system is needed to obtain extremely high electric fields interacting with a solid target. The laser system used in this work is the Lund Multi-Terawatt Laser System, very schematically illustrated in Figure 3.1. The laser chain is a typical CPA system, starting with a Ti:Sapphire oscillator delivering 30 fs laser pulses at a repetition rate of 80 MHz. Pulses are picked at a repetition rate of 10 Hz and fed into a multipass amplifier (Preamp in Figure 3.1). The pulses are then stretched to approximately 450 ps, and their spectral phase can be controlled with an acousto-optic programmable dispersive filter (AOPDF). The pulses continue into the power amplifier which consists of a regenerative amplifier followed by a multipass amplifier, where the pulse energy is increased to approximately 400 mJ. These pulses are spatially cleaned with a spatial filter (SF) before they reach the final multipass amplifier, where their energy is further increased to up to 2 J.

The pulses are still stretched, and they cannot be compressed in air since the resulting peak power of the pulses would cause dielectric breakdown of air. The pulse compressor and the rest of the laser transport chain are therefore mounted in vacuum. The grating-based pulse compressor brings the duration of the laser pulses to close to their initial duration, of about 35 fs. Part of the beam from the compressor can be intercepted and sent to be characterized. After the pulse is compressed, it can be sent through a double plasma mirror (DPM, described in Section 3.3) to be temporally cleaned before it is focused onto a solid target with an off-axis parabolic mirror (OAP).

The amplification and transport chain of the laser system introduces imperfections into the spatial and temporal features of the laser pulse, making the laser–solid interaction sub–optimal. To measure and correct for these imperfections, a set of diagnostic tools and

correction devices is used at different locations throughout the laser chain, to the laser–solid interaction point. These are discussed in more detail later in this chapter.

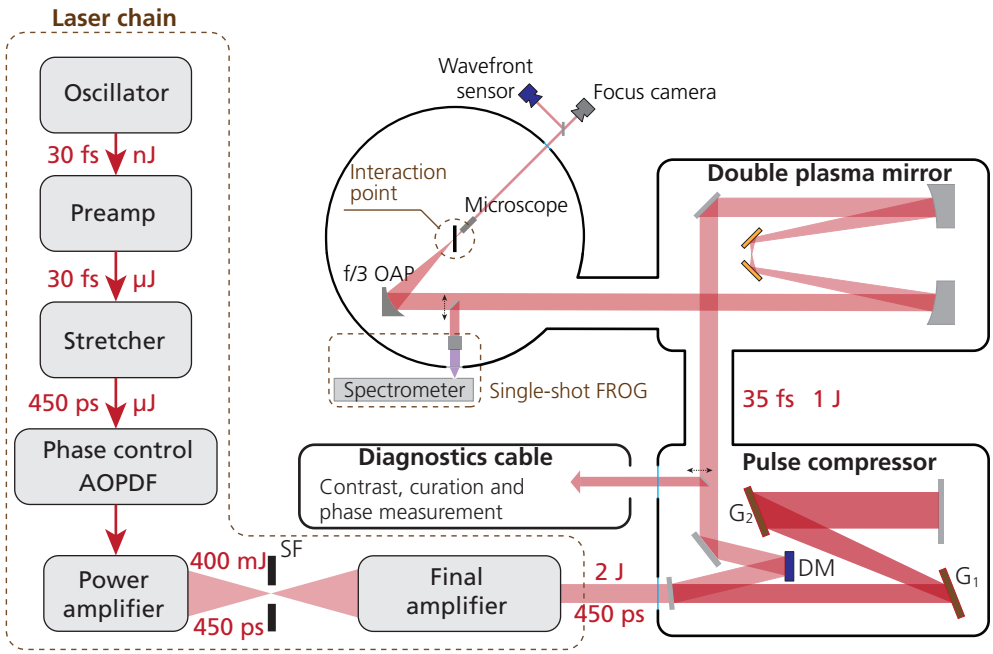

Figure 3.1: Schematic image of the laser chain and the pulse delivery chain of the Lund Multi-Terawatt Laser System. SF denotes spatial filter, DM – a deformable mirror, and G_1 and G_2 are compressor gratings.

3.1 Spatial Wavefront

The effective interaction of the laser pulse with the target relies on the ultrahigh intensity of the laser pulse. In order to achieve such high intensities, the laser beam must be tightly focused. However, the wavefront of the beam suffers aberrations due to beam propagation through the amplification chain of the laser system, where it is subjected to air inhomogeneities and imperfections in various optical components. In order to compensate these effects a wavefront sensor [62] and a deformable mirror [63] are used. A deformable mirror (DM) is a reflective membrane, allowing the principal curvature to be changed, an piezo-actuators (31 in the case of the DM used this work) that allow the shape of the mirror to be locally modified. A photograph of the DM used in the laser chain and the spatial arrangement of the actuators are shown in Figure 3.2.

The wavefront sensor and the DM are connected by software that forms a positive feedback

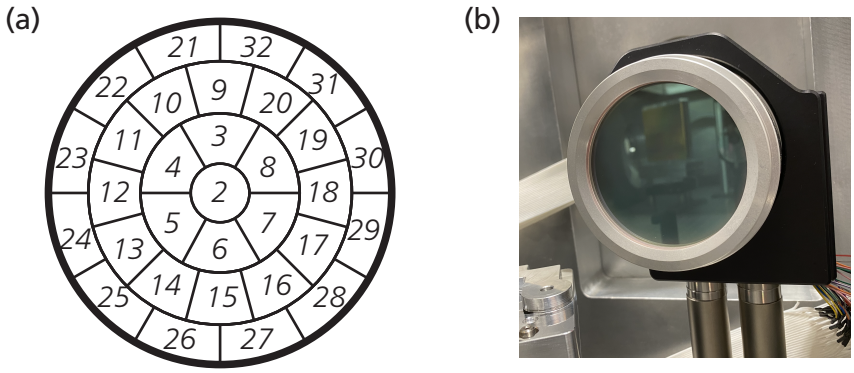

Figure 3.2: (a) Schematic illustration of the deformable mirror used in this work, with 32 electrodes. The first electrode, used for the adjustment of global curvature, is not shown in the illustration. (b) A photograph of the deformable mirror installed after the pulse compressor.

loop between them. This makes it possible to adjust the wavefront of the pulse to a desired arbitrary shape, including the corrections made for optical components downstream of the DM (allowing compensation for even small misalignments of the focusing OAP), provided the wavefront sensor is placed after the focal plane. The wavefront measured by the sensor is approximated by the software using a Zernike polynomial. After the polynomial is calculated and the desired wavefront is determined, the software sends information on the voltages required on the DM piezo-actuators based on an actuator response calibration.

In order to achieve the smallest possible focal spot size and thus the highest intensity on target, the wavefront is usually set to be flat. Figure 3.3 shows an example of the measured wavefront and recorded focal spot before and after the optimization of the laser pulse wavefront. Running the optimization loop enabled the intensity of the focused laser pulse to be increased by approximately 30% in the particular case depicted in Figure 3.3.

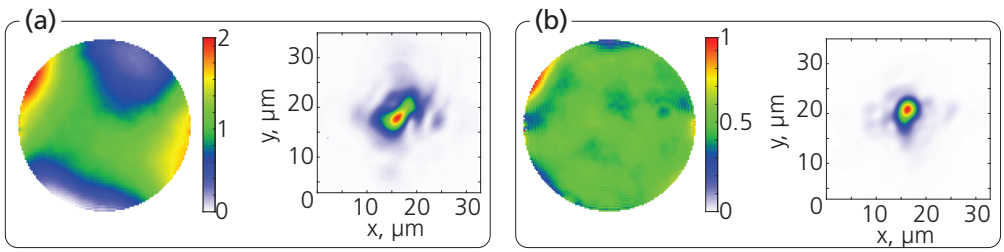

Figure 3.3: The spatial wavefront and focal spot measurement of the laser pulse before (a) and after (b) running the optimization loop.

3.2 Temporal Shape of the Laser Pulse

A laser pulse created by a real CPA system has a complicated temporal profile, as illustrated in Figure 3.4. For simplicity, it can be divided into three parts, each having different duration and intensity. The longest part of the pulse is called the pedestal. This typically originates from the amplifiers of the laser chain due to amplified spontaneous emission, cannot be compressed, and can last for several nanoseconds before (and after) the peak of the pulse. The next part is closer to the peak of the pulse, preceding it by tens of picoseconds and is commonly caused by imperfections of the optical elements in the stretcher, introducing random phase variation to pulse spectral components, which in turn makes them incompressible. In this thesis, this part of the laser pulse is referred to as the shoulder. Finally, the most intense part of the pulse, that is compressed to a duration of few tens of femtoseconds, will be referred to as the ultrafast part of the laser pulse, or the main pulse.

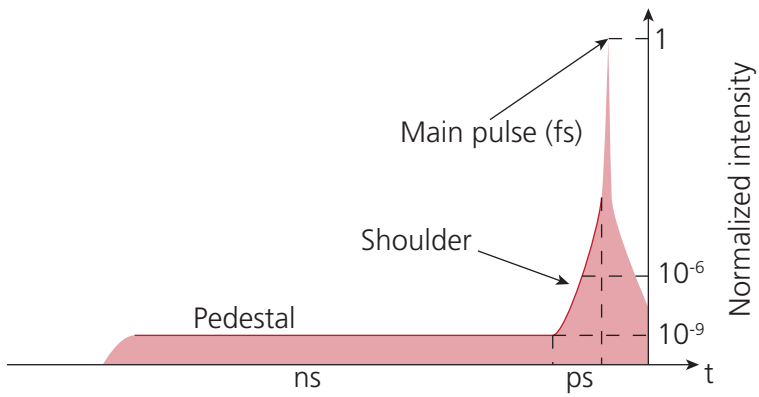

Figure 3.4: Schematic illustration of a realistic laser pulse. The duration of the main pulse is on the order of tens of femtoseconds.

Each part of the laser pulse differs in intensity by many orders of magnitude, and different tools are needed to characterize and control them. An overview of these tools is given below.

3.2.1 The Ultrafast Pulse

Let us start by describing the means of measuring and controlling the properties of the ultrafast laser pulse, as introduced in Section 2.1.1.

The intensity of a laser pulse is highest when the pulse is as short as possible, also known as the transform limit. In the work presented in this thesis, the pulse properties were routinely checked using a pick-up mirror in the pulse compressor (see Figure 3.1). However, in order to have information about the exact pulse properties during the laser-matter interaction,

it is useful to intercept and characterize the laser beam as close to the interaction point as possible.

The core element of the pulse characterization is a single-shot intensity autocorrelator, illustrated in Figure 3.5. The incoming laser pulse is spatially split by a knife-edge prism, forming the two arms of the autocorrelator. One of the arms includes a delay line so that the relative arrival times of the pulses at the non-linear crystal can be adjusted. When the two pulses overlap spatially and temporally in the crystal, a non-collinear second harmonic signal is generated. This signal is the autocorrelation of the pulse, and its width corresponds to the pulse duration. A common way of detecting the signal is to use a camera with an objective lens imaging the non-linear crystal.

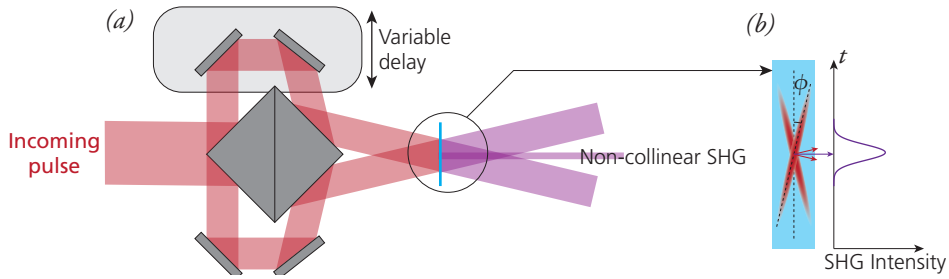

Figure 3.5: Schematic illustration of a prism single-shot autocorrelator (a) and delay introduction in a non-linear crystal (b).

While using an intensity autocorrelator is the simplest and fastest way to determine the duration of the main part of the laser pulse, the shape of the pulse has to be assumed, and no information is provided on the electric field of the pulse. One way of obtaining this information is by placing an imaging spectrometer in the non-collinear second harmonic beam to obtain a spectrogram of the autocorrelation of the laser pulse. This technique is known as frequency-resolved optical gating (FROG) [64]. More specifically, in the context of this work, a second harmonic FROG setup was used (SHG-FROG). When used in high-power applications, the setup can be arranged so that pulse splitting and second harmonic generation take place in vacuum, and only the low-intensity non-collinear second harmonic signal is transferred through an optical window to the spectrometer and the detectors placed in air.

The spectrograms obtained with the FROG setup can be used to determine the exact temporal shape and phase of the laser pulse by using well-known numerical retrieval algorithms, explained in detail in other works [64, 65].

The ability to determine the exact temporal shape of the pulse as it arrives at the target also allows the shape of the pulse to be controlled and adjusted to an arbitrary shape. The laser system used in this work includes an acousto-optic programmable dispersive filter, or

DAZZLER supplied by FastLite [66], (denoted AOPDF in Figure 3.1). Such a filter allows the spectral intensity and phase to be changed to obtain the desired temporal properties of the main laser pulse on target.

The spectral intensity and phase of the pulse are usually adjusted to achieve optimal amplification and to give the shortest pulse at the interaction point. Figure 3.6 shows an example of a spectrum and a temporal profile of the pulse with parameters optimized to achieve the shortest possible pulse, obtained during one of the experiments of this work.

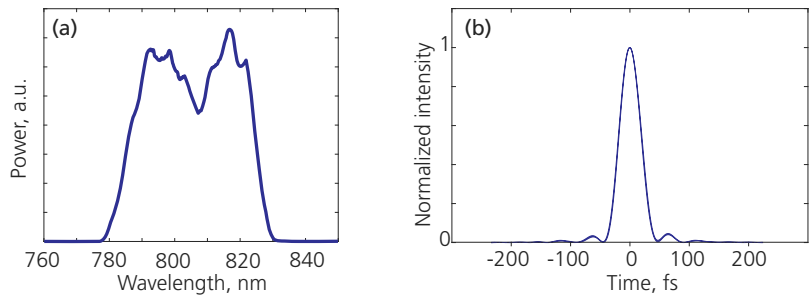

Figure 3.6: *(a)* The spectrum of the laser pulse and *(b)* the temporal intensity of the laser pulse, corresponding to the spectrum shown in *(a)*, at the interaction point.

3.2.2 Temporal Contrast

The temporal contrast of the pulse is usually defined as the ratio between the peak intensity of the ultrafast part of the pulse and the pedestal or the shoulder of the pulse. The intensity of pedestal in the laser system used in this work without the DPM is commonly 10^8–10^9 times lower than the peak of the pulse. However, bearing in mind that the peak intensity of the ultrafast part of the laser pulse on target is 10^{19} W/cm^2, the pedestal can ablate the target surface before the arrival of the main part of the pulse. In addition, the shoulder of the pulse being 10^5–10^6 times less intense than the peak of the pulse, will at least partly ionize the target.

If the target is thick enough to survive the interaction with the pedestal, the main part of the pulse will interact with a long plasma gradient produced by the pedestal and the shoulder on the front surface of the target. While this is not critical for some studies, experiments relying on the interaction of lasers with ultrathin targets (< 1 μm) or with nanoscale structures on the front surface of the target require very high contrast to ensure that the target remains unperturbed before the arrival of the main part of the pulse.

The level and duration of the pedestal can be estimated by using a fast photodiode and a fast oscilloscope when the diode is saturated by the main pulse. The timing of the the optical

pumping in the laser amplifiers or the pulse-cleaning Pockels cells can be changed to modify the duration of the pedestal. However, diodes are not sufficiently fast and lack the dynamic range needed to measure the properties of the shoulder of the laser pulse. To accurately estimate the contrast of the pulse on the picosecond timescale a device with a high dynamic range (at least 10^8) and subpicosecond temporal resolution is needed. One approach is to use self-referenced spectral interferometry [67, 68], which can also be used in its single-shot version, providing dynamic range covering 8 orders of magnitude [69]. Another approach is to use a third-order cross-correlator (TOCC). The contrast measurements reported in this work were obtained with a Sequoia scanning TOCC (Amplitude Technologies) that has a dynamic range of 10^{10}.

The Sequoia TOCC is routinely used on the diagnostics table (see Figure 3.1) to monitor the contrast of the compressed laser pulse. However, it can be moved to monitor the contrast of the pulse close to the interaction point. A typical contrast measurement is shown in Figure 3.7. It does not change significantly with the position of the measurement device. A common way of improving the pulse contrast is to use a plasma mirror. This is a passive

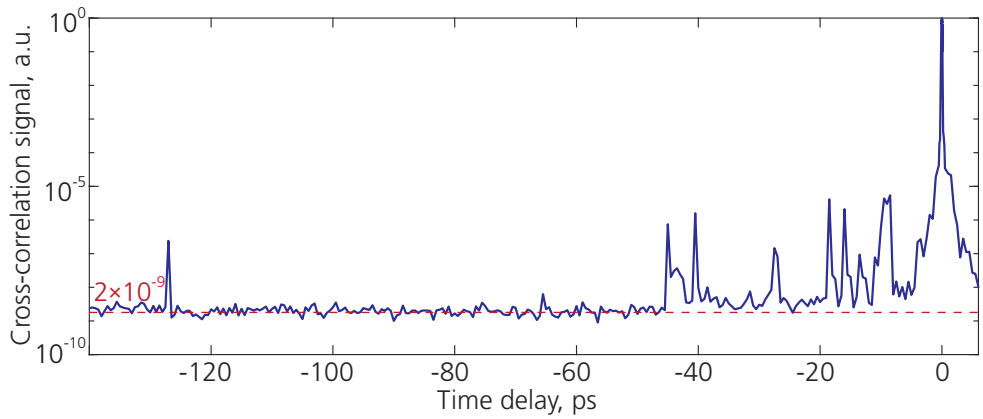

Figure 3.7: A typical contrast obtained from the Lund High Intensity laser system with the Sequoia TOCC. It should be noted that internal reflections in the device may cause parasitic prepulses in the measurement trace.

device that prevents the low-intensity pedestal from reaching the target at the interaction point. Plasma mirrors can be cascaded, and two are often used together. Such a DPM [70, 71] was designed, constructed, and used in the work presented in **Papers II–IV**. It is ddescribed in more detail in Section 3.3 below.

3.3 Double Plasma Mirror

3.3.1 Principle of Operation

The operating principle can be qualitatively discussed for the case of a single plasma mirror. The laser pulse is incident on a thick dielectric slab (substrate) that is typically anti-reflection–coated and for simplicity can be assumed to reflect no light in the linear regime. The pedestal of the pulse is transmitted through the substrate due to its low intensity. The shoulder of the pulse, on the other hand, is sufficiently intense to cause multiphoton ionization of the substrate, followed by avalanche ionization in the region close to the surface of the substrate [72, 73]. Once the plasma density reaches the critical density n_c, the substrate switches from being a perfectly transmitting window to a perfectly reflecting mirror. This interaction is illustrated schematically in Figure 3.8.

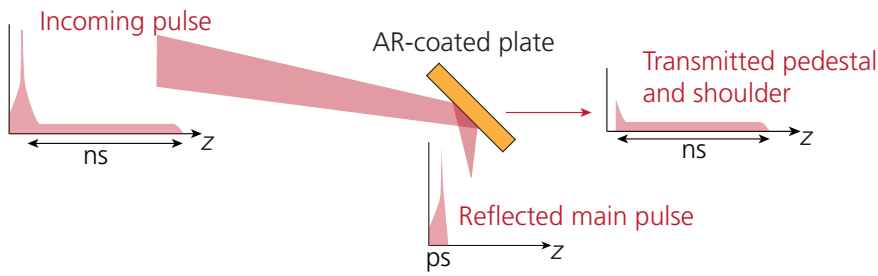

Figure 3.8: Illustration of the principle of a plasma mirror. AR denoted anti-reflection.

When the main part of the pulse is reflected, it is important to avoid heating the electrons as this would lead to absorption of the main part of the pulse. The simplest way to do this is to have the plasma mirror (PM) interact with s-polarized light, since this will eliminate both resonant absorption and vacuum heating, and limit the peak intensity on the substrate such that $\mathbf{j} \times \mathbf{B}$ heating will not be significant.

It is worth noting that although the triggering of a PM is directly related to the accumulated laser fluence on the substrate, it is very common for the pulse reaching the PM to be described in terms of its peak intensity.

3.3.2 The Double Plasma Mirror at the Lund High-Power Laser Facility

A design of a DPM is individual for any laser facility since it must take into consideration the properties the laser pulses produced by a particular system (i.e. pulse energy, pulse contrast) and possible space restrictions. However, a common starting point is the estimation of the fluence on the substrates of the DPM and the corresponding spot size. The front sur-

face plasma will have reached the critical density after the laser pulse has deposited fluence Γ_0 (for a glass substrate it is around 10 J/cm^2). In order to estimate the spot size on the substrate, the contrast measurement of the laser pulse must be analyzed. The contrast curve shown in Figure 3.7 gives the average intensity of the pedestal. Although the measurement is limited by the device time window of 150 ps prior to the peak of the pulse, it is possible to see the transition between the shoulder of the pulse and the pedestal.

One way of selecting the trigger time is to use an external laser pulse preceding the main part of the laser pulse by a certain controllable delay [74]. While this can improve the reflectivity of a single PM, the most common configuration utilizes a self-triggered scheme where the PM is triggered by the pedestal of the laser pulse, as was the case in this work. The fluence is then controlled by the spot size on the substrates of the DPM. Based on the assumptions above and considering the total energy of the laser pulse to be 1 J when it reaches the DPM substrates, the spot size on the substrates has to be approximately one mm in diameter for the plasma mirror to trigger just before the main part of the pulse. In this case the peak intensity on the substrates is on the order of 10^{15} W/cm^2.

To achieve these values,in the DPM setup used in this work, the laser was focused by a 1 m focal length off-axis parabolic mirror, and the substrates were placed 17 mm away from the focal plane. The focal plane is usually located midway between the reflective surfaces of the substrates as this has been shown to yield the highest transmission of the DPM, while providing significant contrast enhancement[75]. The substrates are moved by a combination of motorized stages, and the laser beam is recollimated after the cleaning with an off-axis parabolic mirror identical to the focusing one. The overview render of the DPM is presented in Figure 3.9

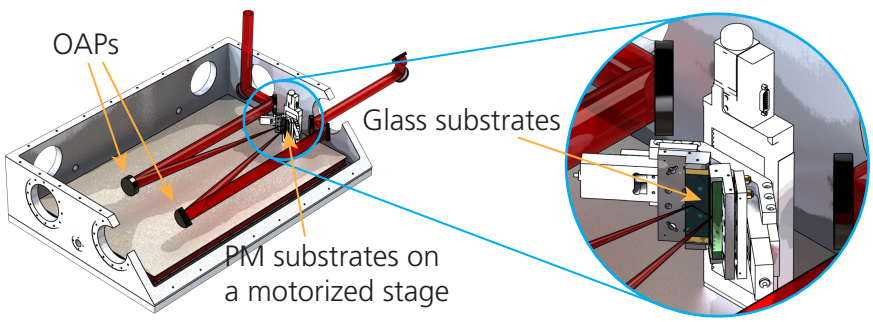

Figure 3.9: A render of the double DPM CAD assembly. OAP denotes off-axis parabolic mirror.

3.3.3 Optimization

Ideally, the DPM should be triggered immediately before the arrival of the main part of the laser pulse. However, it is difficult to achieve the optimal fluence on the substrates' surfaces in practice, and in some cases it has considerable consequences.

If the fluence is too low, the DPM turns on after the arrival of the leading edge of the main pulse. Such effects were explored in the sudy described in **Paper IV**. In that work, the main part of the pulse was temporally stretched to study the effects of pulse chirp on the protons accelerated from ultrathin foils, where high contrast was needed. Temporal stretching of the pulse caused the part of the spectrum of the pulse corresponding to its leading edge to be discarted by the DPM. The spectral transmission of the DPM for such a scenario is shown in Figure 3.10.

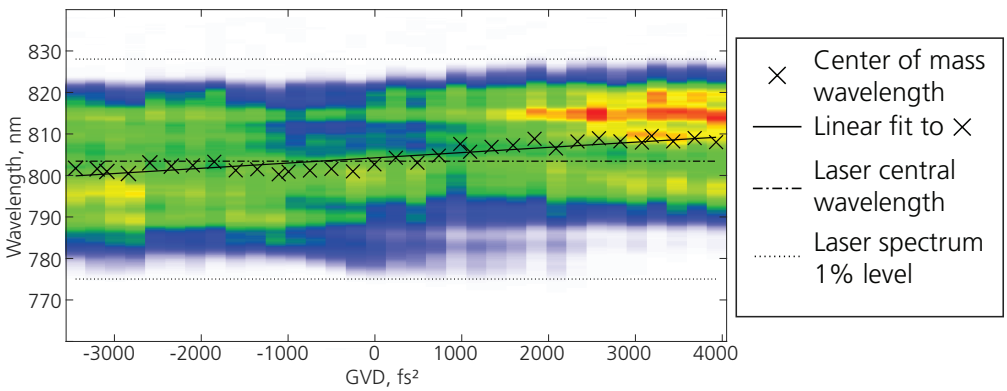

Figure 3.10: Spectral transmission of the DPM when triggered later than the optimal time, as a function of GVD (pulse chirp). The change in the GVD (resulting in a change in the pulse duration) was introduced by changing the pulse compression prior to the DPM.

It can clearly be seen from the figure that the central wavelength of the transmitted spectrum and its width depend on the GVD (chirp) of the laser pulse, causing a shift to shorter wavelengths for a positively chirped pulse, and to longer wavelengths in the case of a negative chirp. Such behavior is in agreement with what reported in other study on the temporal reflectivity of plasma mirrors [76]. The 'missing' parts of the spectrum lead to temporal modification of the laser pulse when it reaches the interaction point on the target, which can be crucial for studies relying on pulse chirp characterization.

If, on the other hand, the spot size on the substrates is too small, causing the fluence to be too high, the DPM will trigger too early. This will reduce the contrast enhancement provided by the plasma mirror but, more importantly, it will increase the peak intensity of the laser pulse on the substrates. The drawbacks of the intensity being too high can

be attributed partly to the hole boring effect (see Section 2.2.2) and partly to the plasma forming the reflecting surface getting enough time to evolve, affecting the wavefront of the reflected pulse.

If the intensity is too high, any deviation from the desired flat-top beam profile on the substrates will result in a non-uniform pressure on the plasma critical surface, causing it to move towards the substrate. If the non-uniformity of the beam intensity is high enough to significantly move part of the critical surface, it will essentially create a phase plate in a converging beam, resulting into intensity redistribution into Fresnel rings. In such a case the intensity in the central spot can be high enough to damage optical elements downstream. A normal and such a 'ring' nearfield spatial profile of the laser beam are shown in Figure 3.11 together with the beam imprint on the second substrate.

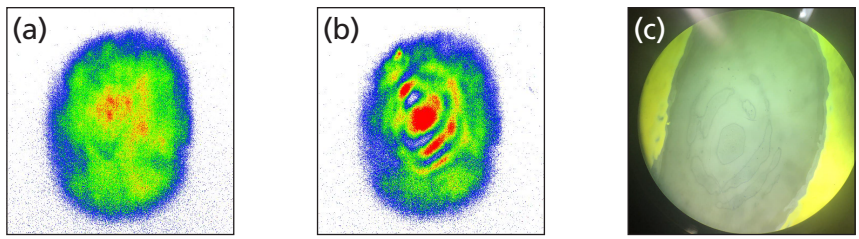

Figure 3.11: (a) Nearfield profile of a beam reflected by the DPM without surface distortion. (b) Nearfield profile of a beam reflected by the DPM with surface distortion on the first substrate, (c) A microscope image (x10) of the second substrate when hole boring occurred on the surface of the first substrate.

Although a non-flat plasma critical surface on the substrates can be highly destructive, if properly controlled it provide opportunities for interesting applications. For example, the reflecting surface of the PM can be shaped to constitute a phase plate in order to obtain angular momentum beams [77] or to assist in focusing the laser pulse [78, 79].

However, when the fluence on the DPM substrates (i.e. the distance between the focal spot and the substrate surface) is optimal, the spatial and spectral properties of the laser pulse are not affected, and the contrast is noticeably enhanced, while letting a significant fraction (50%) of laser pulse energy available for laser-solid interaction with the target.

The most important performance indicator of a plasma mirror is the enhancement of the temporal contrast of the laser pulse. Figure 3.12 shows a contrast enhancement measurement of two orders of magnitude until up to 2 ps prior to the main peak of the pulse. Such an improvement allows the investigation of the laser–matter interaction with nanostructured targets, as presented in **Papers II–III**, and with ultrathin targets with thicknesses down to 10 nm, as presented in **Paper IV**.

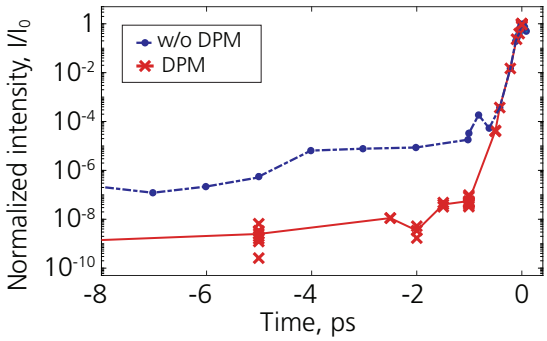

Figure 3.12: Measurements of the temporal contrast of the pulse, with and without DPM.

However, a pulse with high contrast is not in itself useful if the cleaned pulse cannot be tightly focused on the target, thus ensuring an optimal laser–solid interaction. Figure 3.13 shows that optimally configured plasma mirrors have no significant effect on the shape of the laser focal spot.

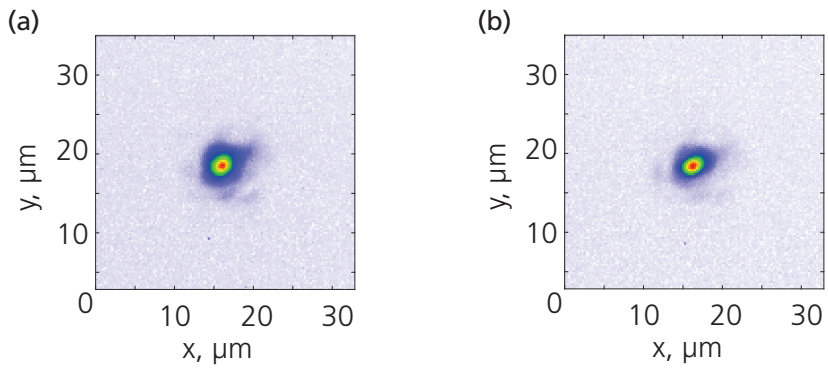

Figure 3.13: Images of the laser focal spot at the laser–solid interaction point, normalized to their respective maxima, when bypassing the DPM (a) and after being temporally cleaned by the DPM (b).

Chapter 4

Laser–Solid Interaction Characterization and Ion Detection

The laser pulse, with its wavefront and temporal shape adjusted to the desired values, is focused tightly onto the solid target surface at the center of the experimental chamber. A common way of studying such an interaction of a solid with extreme electric fields is to record and analyze the spectra and spatial distribution of accelerated ions, as well as the changes in the laser pulse. In the experimental setup used in this work (see Figure 4.1) a double-sided ion spectroscopy setup was implemented, consisting of two separate spectrometers simultaneously detecting particles accelerated in the forward and backward directions. The ions accelerated in the forward direction were detected with a Thomson parabola spectrometer (TPS), and protons traveling in the backward direction were detected with a simple dipole magnetic spectrometer. A proton spatial profile detector could be inserted into the forward direction ion beam.

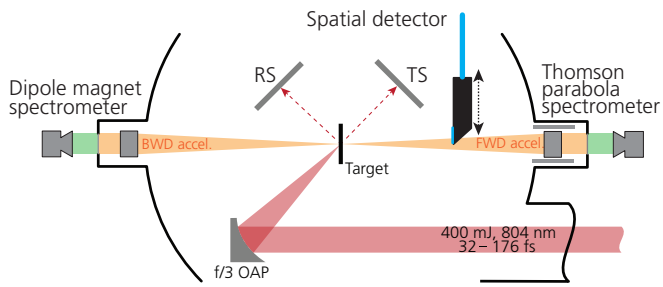

Figure 4.1: Illustration of the interaction characterization arrangement. FWD denotes forward, BWD backward, TS transmission scatter screen, RS reflection scatter screen, and OAP off-axis parabolic mirror.

4.1 Balanced Light Reflection and Transmission Detector

Changes in the amount of reflected and transmitted laser radiation can be recorded by placing Spectralon scattering screens (LabSphere, SRT-99-050) in the reflected and transmitted laser beams, and using cameras equipped with appropriate neutral density filters and a bandpass filter at the laser wavelength. observing the screens, one can record changes in the amount of reflected and transmitted laser radiation. Such an arrangement was used in the work presented in **Papers II–III**

In order to be able to directly compare the reflected and transmitted signals, the two sides (reflection and transmission) of the detector must be cross-calibrated. This can be performed by recording the images produced on each of the screens when they are illuminated (one at a time) by a reference laser beam of the same power, usually using a helium-neon laser, and setting the same integration time on the cameras. This method inherently accounts for the angles of observation and the responses of the cameras.

When studying the interaction at full power, different sets of calibrated filters are placed in front of the two cameras. Knowing the transmission of these filters, it is then possible to directly compare the reflection and transmission signals normalized to the counts of a 'blank shot', obtained by measuring the transmission signal when no target is placed in the focus of the laser.

4.2 Ion Spatial Detector

A specialized detector was introduced in order to monitor the spatial profile of the accelerated ion beam. Such a detector was used in the experiment presented in **Paper I**.

The spatial profile detector consisted of a scintillator screen, the front of which is protected by an aluminum foil to shield the scintillator from laser and plasma light and debris originating from the laser–solid interaction. The foil thickness was chosen such that the protons could pass through to the scintillator, but heavier ions were stopped. Furthermore, an aluminum grid was placed in front of the detector, allowing for the electron background to be subtracted [80]. The light produced by the scintillator was collected by an objective lens and transferred via a fiber bundle to a camera outside the vacuum chamber.

The scintillator and the objective lens were enclosed in a light-tight box in order to avoid light pollution, and the box was placed on a translation stage so that the spatial detector could be moved in and out of the ion beam. A more detailed description of the spatial detector can be found in other work [81].

4.3 Magnetic Dipole Spectrometer

Ions accelerated in the backward direction were were detected with a dipole magnet spectrometer. The principle of such a device is very simple, and is shown schematically in Figure 4.2.

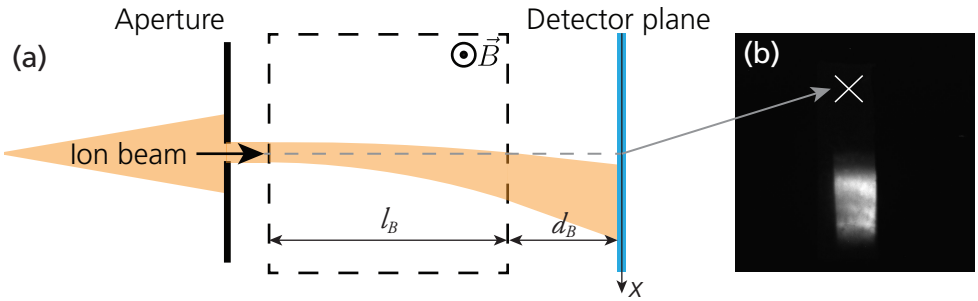

Figure 4.2: Schematic illustration of a dipole magnetic spectrometer (a) and a spectrometer trace observed in the detector plane (b).

An ion with charge q and mass m passing with velocity v through an entrance slit is subjected to a uniform magnetic field of strength B. If the magnetic field acting on the particle has a length l_B and the field-free particle propagation distance is d_B, then the particle displacement in the detection plane, x, can be calculated as:

$$x = R - \sqrt{R^2 - l_B^2} + \frac{l_B d_B}{\sqrt{R^2 - l_B^2}}, \tag{4.1}$$

where R is the radius of the circular trajectory of a particle moving in a uniform magnetic field due to the Lorentz force. The radius can be analytically expressed as:

$$R = \frac{mv}{qB}. \tag{4.2}$$

As follows from Equation 4.1, all charged particles entering the spectrometer will be dispersed along the same line (see Figure 4.2b), and it cannot therefore be used to simultaneously determine the energy spectra of different ion species. The spectrometer used in this setup was designed to detect only protons. Practical considerations regarding its design, resolution and calibration have been discussed previously [81, 82].

This spectrometer was used in the studies presented in **Paper I** to detect forward-accelerated protons and in **Papers III–IV** to detect protons in the backward direction.

4.4 Thomson Parabola Spectrometer

In order to obtain information on the accelerated ion species, the magnetic field can be complemented with an electric field parallel to the magnetic field. Such a device is called a Thomson parabola spectrometer (TPS), after the name of its inventor [83], and it can spatially separate ions with different charge-to-mass ratios.

Let us first consider an idealized case where both the electric and magnetic fields are uniform, as illustrated in Figure 4.3. The electric and magnetic parts of the Lorentz force, $\mathbf{F} = q(\mathbf{E} + \mathbf{v} \times \mathbf{B})$, acting on the charged particle are perpendicular to each other and can be treated independently. The coordinate axes can be defined such that the magnetic deflection is in the xz plane, and the electric fields acts on the particle along y.

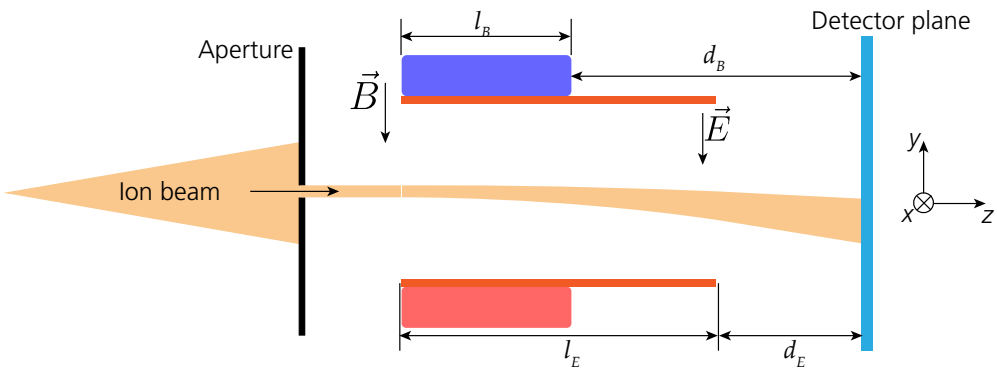

Figure 4.3: Thomson Parabola Spectrometer schematic illustration. The effective magnetic and electric field effective length is l_B and l_E, respectively. In the same fashion, d_B and d_E are the field-free lengths

The deflection of a particle with mass m and charge q in the detection plane can be solved analytically. The magnetic deflection is explicitly given by Equation 4.1. However, the magnetic field inside a TPS is usually low, and the circular trajectory of a charged particle under the influence of the magnetic field can be approximated by a parabolic one (i.e. $v_z \approx v$), yielding:

$$x = -\frac{qB}{mv} \cdot l_B \left[d_B + \frac{l_B}{2} \right]. \tag{4.3}$$

Correspondingly, the particle deflection by the electric field can be calculated as:

$$y = -\frac{qE}{mv^2} \cdot l_E \left[d_E + \frac{l_E}{2} \right]. \tag{4.4}$$

The parameters l and d in Equations 4.3 and 4.4 define the geometry of the spectrometer (see Figure 4.3), where l is the length of the field, and d is the field-free length.

Combining Equations 4.3 and 4.4 gives the shape of the ion trace in the detection plane.

$$y = -\frac{m}{q}\frac{El_E(d_E + l_E/2)}{B^2 l_B^2 (d_B + l_B/2)^2}x^2. \tag{4.5}$$

This equation shows that the ion trace in the detection plane has the shape of a parabola, and the slope of the tangent for a spectrometer of fixed geometry is inversely proportional to the charge-to-mass ratio of the ion. This makes it possible to distinguish between most ion species in the detection plane. However, ions that have the same charge-to-mass ratio will have the same geometrical trace.

The expressions given above were derived in terms of particle velocity, while in the field of particle acceleration it is more common to use the kinetic energy, which in the case of non-relativistic particles is given simply by $E_k = mv^2/2$. It should also be noted that the above expressions provide only a simplified picture. In a real spectrometer the fields are not perfectly homogeneous, and numerical solutions are needed to examine their interaction with charged particles. Such an analysis is discussed in the following sections.

4.4.1 The Thomson Parabola Spectrometer at the Lund High-Power Laser Facility and Practical Design Considerations

The range of particle energies (velocities) and energy resolution in a real spectrometer are affected by its geometry (i.e.the parameters l and d, the detector size and entrance aperture diameter), and the strengths of the electric and magnetic fields. Naturally, a unique design is required for each acceleration facility. The spectrometer described in this section was used to detect forward-accelerated ions, as presented in **Papers II–IV**.

A significant part of the author's work presented in this thesis was dedicated to the design, construction and commissioning of the TPS, including a novel approach for the analysis of digitally recorded TPS traces, motivating a detailed presentation of the topic here.

The ion spectrometer used at the Lund High-Power Laser Facility is designed to accommodate for accelerated protons with energies from 1 MeV up to 10 MeV (15% of the speed of light), while maintaining a sub-MeV energy resolution at the maximum energy. The trade-off between the resolution and the energy acceptance range is ultimately determined by the size of the particle detector which in this case is a 40 mm diameter micro-channel plate (MCP), and the field strengths and the geometry of the spectrometer have to be tailored to meet the design goal. The dispersion element of such a spectrometer often consists of

permanent magnets enclosed in an iron yoke to guide the magnetic field, and a pair of electrodes connected to a high voltage source. A cross-section of the spectrometer CAD assembly and the magnet and electrodes are illustrated in Figure 4.4.

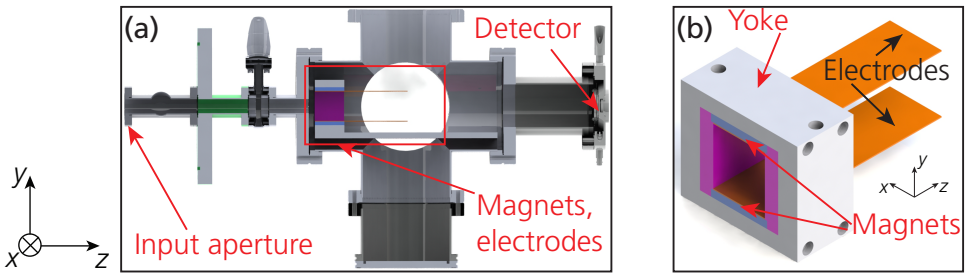

Figure 4.4: (a) The cross-section of the Lund TPS, and (b) the dispersion element assembly.

It is possible that the extents of electrodes shade the particle trace in the detector, and edge effects arising from the electrodes may cause severe disturbance of the electric field. Shading can be overcome, for example, by using electrodes in a wedged configuration [84] or using trapezoidal electrodes [85]. One approach to mitigate edge effects, proposed by Cobble *et al.* [86], uses non-flat electrodes whose boundary follows the equipotential lines of the generated electric field. However, both edge effects and shading can be avoided if the electrodes can be placed (transversely) far enough away from the path of the particles, provided that the strength of the electric field remains sufficient. This approach simplifies the assembly, and was used in the spectrometer design in this work.

The last crucial component of the spectrometer is the particle detector itself. Micro-channel plate detectors with a phosphor screen are commonly used due to their high sensitivity. Such a detector is active and operated under vacuum at high voltage, which makes it possible to gate it. Since the accelerated ions are non-relativistic and arrive at the detector at different times, gating the detector to detect only specific ions can significantly reduce the noise [87].

The resolution of the spectrometer is limited by the spot size in the detector plane. The spot is usually determined by the size of the entrance aperture (usually circular). Denoting the diameter of the aperture d_a, the distance from the source to the aperture L_a, and the distance between the aperture and the detector L_s, the spot size on the detector can be simply obtained as:

$$\delta = d_a \frac{L_a + L_s}{L_a}. \tag{4.6}$$

The finite spot size in the detection plane corresponds to the uncertainty in the retrieval of the particle energy. If particles of energy E_0 reach the detector at a transverse position $[x(E_0), y(E_0)]$, lying on a parabolic trace $[x(E), y(E)]$ (see Equations 4.3 and 4.4), then the

experimental trace will form a circle around that point with a radius of $\delta/2$, and the edges of the circle will intersect the trace at a point $[x(E_0) \pm \delta/2, y(E_0) \pm \delta/2]$ corresponding to $[x(E_0 \pm \Delta E/2), y(E_0 \pm \Delta E/2)]$.

Since the spot size is constant, and $[x(E), y(E)]$ is not linear, the uncertainty in the energy, ΔE, is a function of the particle energy, and can be easily calculated numerically. Decreasing the size of the aperture increases the resolution of the spectrometer at the cost of the signal in the MCP. The smallest possible diameter of the spot on the detector is determined by the spatial resolution of the MCP and its phosphor screen, which is usually on the order of few tens of µm. For the geometry of the TPS used in this work the optimal aperture size was found to be 100 µm, and the energy uncertainty, ΔE, for protons with a kinetic energy of 10 MeV was only 0.5 MeV, or 5%.

4.4.2 Energy Calibration

As mentioned above, the magnetic and electric fields in the spectrometer are not completely homogeneous, and a simple analytical estimate of the fields is not sufficiently accurate, motivating the use of other methods of quantifying the influence of the fields on the particle trajectories.

One approach is to probe the fields directly with mono-energetic beams of charged particles, as presented by Schillaci *et al.* [88]. This provides a direct measurement of particle deflection as a function of particle kinetic energy, and the effective fields can then be estimated. However, a drawback of such an approach is that the calibration is only valid for the ion species used for the measurement. Different ion species will follow a different path through the spectrometer and will experience different deflection fields.

Another approach is to use numerical simulations of the fields inside the spectrometer, as was done in this work. A useful software tool for performing such simulations is COMSOL [89, 90], and it has been used for this purpose previously [91]. An advantage of this tool is its ability to calculate the electric and magnetic fields inside the spectrometer and solve the charged particle trajectories in these fields. The simulation setup geometry was exported from the CAD model shown in Figure 4.4, and simplified by removing elements far from the dispersive element to reduce the calculation time. The calculated electric and magnetic fields are shown in Figure 4.5.

It can be seen that close to the axis of the spectrometer the fields are approximately uniform, and the peak field strengths along the axis are 0.19 T for the magnetic field and 105 kV/m for the electric field.

An asymmetry can be seen in the fringe electric field outside the electrodes in Figure 4.5b. This is determined by the geometry of the vacuum chamber enclosing the dispersive ele-

ment, and further stresses the benefits of using the whole geometry of the spectrometer for the numerical simulations.

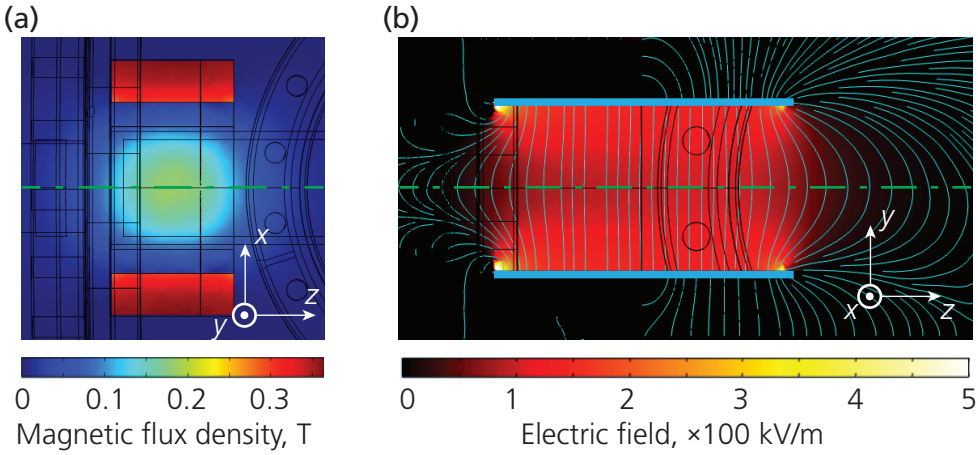

Figure 4.5: (a) The magnetic field distribution in the magnet and the yoke of the magnet and (b) the electric field created by the electrodes in the direction perpendicular to the electrodes. The heavy blue lines indicate the electrodes and light blue lines show the lines of the electric field. The axis of the spectrometer is indicated by the dashed green line. The black lines indicate the outline of the imported CAD geometry used in the simulations.

The calculated field distribution is then used in the particle propagation simulation. In a simplified geometry, the charged particles were released from a source in a virtual plane at the same position and of the same size as the aperture of the spectrometer, and stopped at a virtual plane representing the detector. The simulations provide information on the particle position as a function of time, and an example of three-dimensional calculated particle trajectories is shown in Figure 4.6 for different particle energies. Propagation simulations can be performed for various ion species, resulting in a comprehensive deflection map.

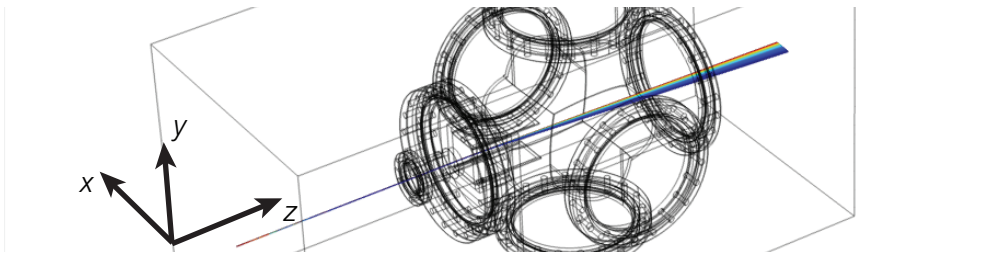

Figure 4.6: Simulated trajectories of protons with kinetic energies from 1 MeV (blue) to 10 MeV (red). The outline of the simulation setup is shown in black.

4.4.3 Particle Flux Calibration

Operating at its full potential, a spectrometer has to should give a reasonable estimate of the number of particles as a function of energy. An MCP with a phosphor screen does not have a linear response, and is dependent on the velocity of the impacting particles and their mass.

A well-established way of calibrating any particle detector is to simultaneously record a spectrum in the detector in question, and a detector with a known absolute response such as radio-chromic film or a CR-39 nuclear track detector [92, 93]. In this work, calibration was performed according to the approach described by Prasad *et al.* [94], where a milled CR-39 detector was placed directly in front of the MCP. In this case each of the parabolic traces on the detector is periodically interrupted. An example of the resulting traces is shown in Figure 4.7.

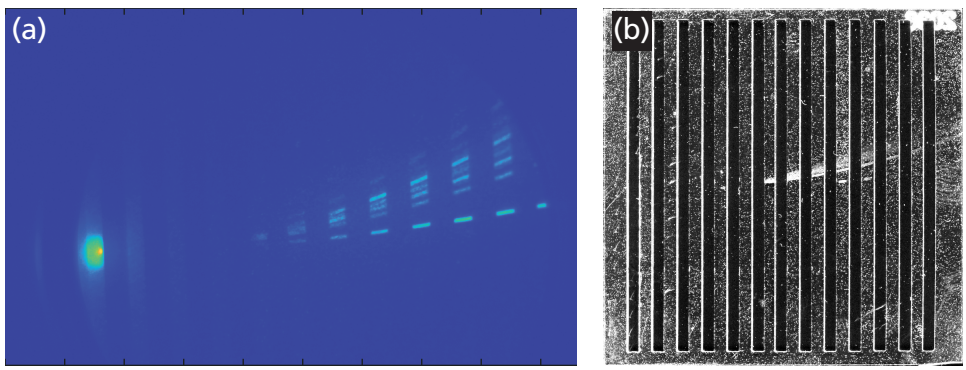

Figure 4.7: (a) Image of a calibration shot recorded with the MCP detector, and (b) a contrast–enhanced image of the same calibration shot recorded with the CR-39 nuclear track detector. Note that the images are not shown on the same scale.

The CR-39 detector is then removed and etched in a hot NaOH solution, after which the pits produced in the detector can be counted in each of the milled slots for different ion traces using an optical microscope. The same approach is utilized for the traces recorded with the MCP. The total number counts can then be interpolated along the traces to fill the the regions which have no signal in both the CR-39 and the MCP detectors. The energy-dependent calibration for ions, having different charge-to-mass ratios, can also be interpolated along the milled slots to obtain estimates of a calibration for ions not present in the calibration shot. However, while interpolation of the calibration is very straightforward, extrapolation to ions with low charge-to-mass ratios absent in the calibration shot is generally not reliable. In this work, the ion species with the lowest charge-to-mass ratio, found in the traces, were C^{4+}, so the two-dimensional calibration is only valid for ions with higher charge-to-mass ratios, such as, for example p+, C^{5+} and O^{6+}.

4.4.4 Ion Trace Processing

When the spectrometer is fully calibrated, it is possible to analyze the ion traces to fully retrieve the spectra. Figure 4.8shows the initial trace and the calibrated trace from the spectrometer. These traces were recorded in preparation for the experiment described in **Paper IV**, using a high-contrast 400 mJ laser pulse and a 10 nm amorphous carbon foil as the target. Apart from the ion traces, a bright spot can be seen on the axis of the spectrometer. This spot is is the result of neutral particles created during the laser-solid interaction (neutral atoms and photons) [95, 96], and is be referred to as the 'zero order' of the spectrometer. This defines the origin of the $[x, y]$ coordinate system.

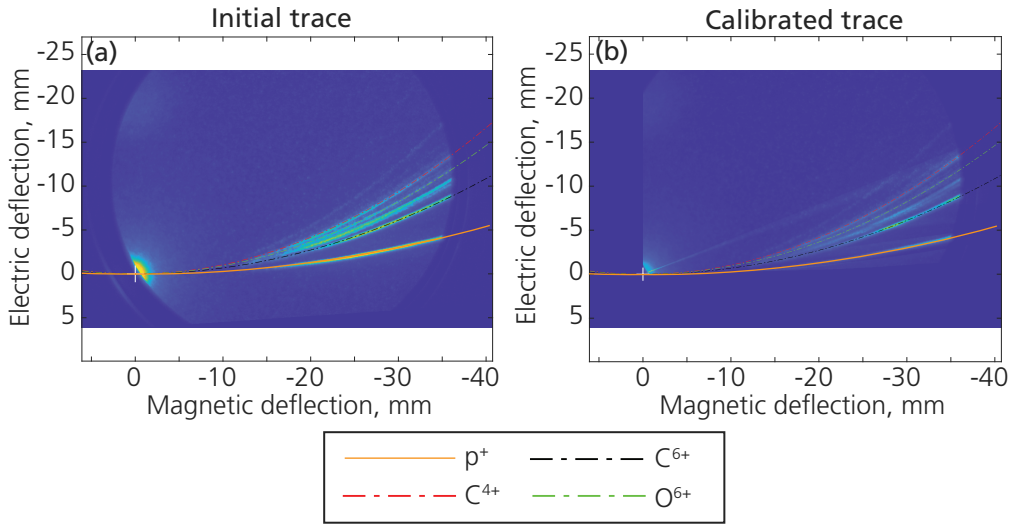

Figure 4.8: Initial (a) and calibrated (b) spectra obtained by the TPS. The lines show the traces of selected ion species, and the white cross indicates the axis of the spectrometer.

The next step is to perform the ion flux calibration. The calibrated trace is shown in Figure 4.8 on the right. The calibrated image is then used in further analysis.

These parabolic traces are inconvenient to be spatially selected for isolating single ion traces. Therefore, a new coordinate system is introduced, in which the parabolic traces become straight. Introducing a simplification so that G_B and G_E are the geometric constants of the magnetic and electric field arrangements, respectively, and defining $\sigma = q/m$ as the charge-to-mass ratio of an ion, Equations 4.3 and 4.4 can be rewritten as:

$$\begin{cases} x = -\dfrac{\sigma}{v} G_B B \\ y = -\dfrac{\sigma}{v^2} G_E E \end{cases} . \tag{4.7}$$

This system can be solved for v and σ giving:

$$\begin{cases} v = \dfrac{x}{y} G_E E \\ \sigma = -\dfrac{x^2}{y} \dfrac{G_E E}{G_B B} \end{cases} . \tag{4.8}$$

It can be seen from these equations that a TPS trace $T(x, y)$ is a set of parabolic lines, but after the space coordinates $[x, y] \rightarrow [v, \sigma]$, as in Equation 4.8, the new trace $T'(v, \sigma)$ becomes a set of horizontal straight lines. Such a transformation is called species mapping. The result of species mapping is presented in Figure 4.9. For simplicity, the charge-to-mass ratio is expressed as a unitless value considering the charge of a proton and the mass of a nucleon (proton or neutron) to be equal to 1.

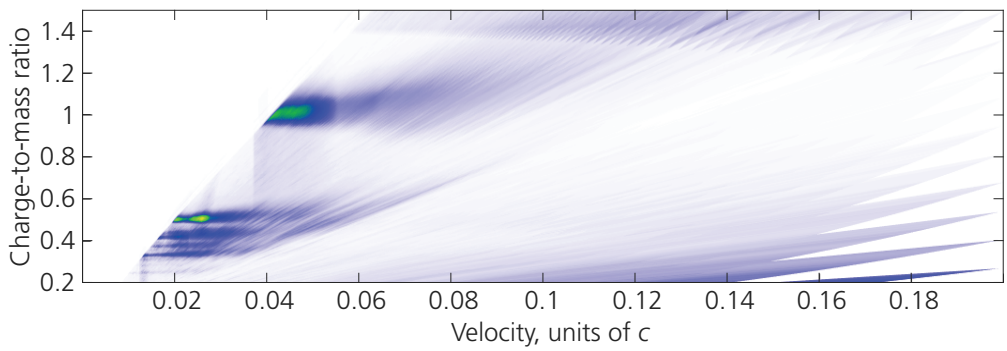

Figure 4.9: Result of species mapping transform result of the calibrated trace in Figure 4.8b.

Figure 4.9 shows values of charge-to-mass ratio that are larger than one. While this is mathematically possible, there will be no ion traces in that region. It can also be seen that the widths of the ion traces in the new coordinate space are not constant. This is because species mapping is not a linear transformation. When the coordinates are transformed, the distances between neighboring points (i.e. the geometrical width of the trace) in $[x, y]$ increase in $[v, \sigma]$ as σ increases. Furthermore, the image boundaries cease to be rectangular, and the lowest velocity detected by the spectrometer depends on the ion species.

Representing ion traces in this way also allows for direct comparison of the velocities of different ion species and facilitates integration to retrieve the total ion content. When the trace is integrated over v ion species distributions are produced, each of the species having a bell-shaped peak. Knowing the charge-to-mass ratio of each abundant ion in the range $[\sigma(C^{4+}), \sigma(p^{+})]$, one can simply fit a sum of Gaussian curves to the measured distribution, as shown in Figure 4.10. The Gaussian peaks have determined position and width, corresponding to the species of the ion and the geometric width of the trace in the spectrometer. This effectively reduces the fitting to only the amplitudes of the peaks.

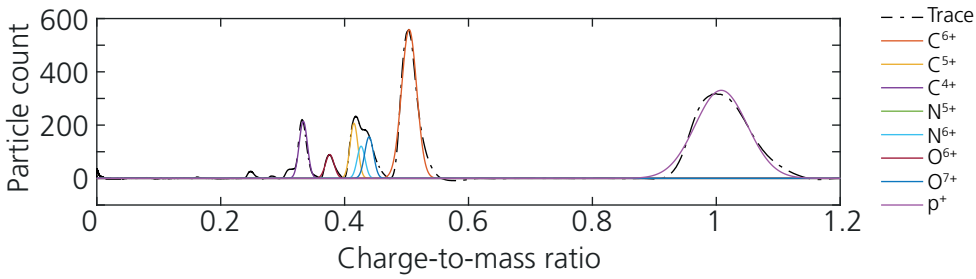

Figure 4.10: Ion distributions, produced from the calibrated trace in Figure 4.8b.

As a result it is possible to extract individual ion species contents even if the corresponding trace separation is below the spatial resolution of the spectrometer. The total ion content can be obtained by integrating each Gaussian peak individually. The result of such an integration is shown in Figure 4.11.

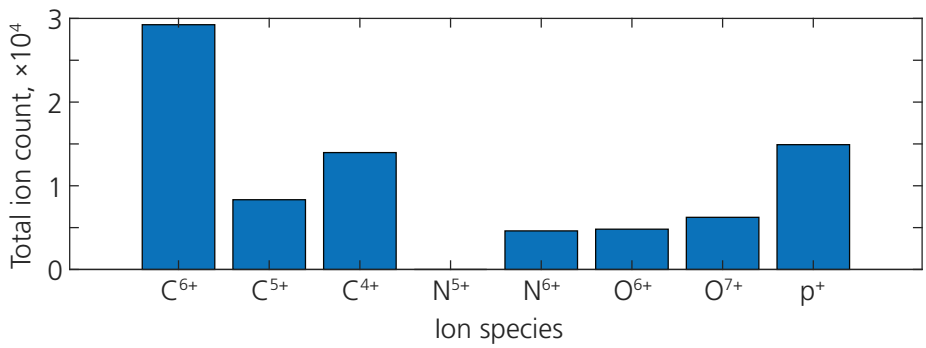

Figure 4.11: Integrated ion counts, obtained from the trace shown in 4.8b.

The geometrically resolved ion traces can be filtered by the value of σ and then integrated over σ. This results in the conventional one-dimensional spectrum, and the velocity of each ion species can be easily converted into energy. A selection of spectra for fully geometrically resolved ion traces is shown in Figure 4.12.

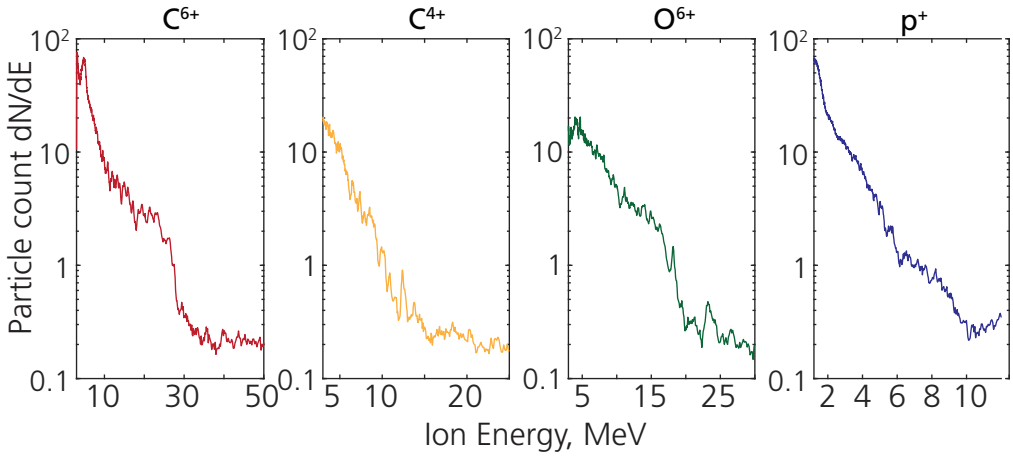

Figure 4.12: The final spectra for selected ion species, corresponding to the traces in figure 4.8b.

While the processing algorithm provides valuable insight into the properties of different ion species, the work presented in **Papers II–IV** focused primarily on proton acceleration. Detailed investigations of the changes in the properties of other ion species when varying target and laser parameters will be a subject of future research.

Chapter 5

Proton Acceleration Optimization

The main goal of this part of my work was to find ways of increasing the cut-off energy of the accelerated protons or improving proton beam quality, for example, better collimation.

As mentioned previous chapters, the ion beam properties are determined by the energetic and spatial properties of the electrons forming the acceleration sheath, heated directly by the laser pulse. In this chapter the target and laser pulse manipulation presented in **Papers I–IV** in pursuit of optimization of the electron distribution will be discussed. **Papers I–III** describe the manipulation of the front surface of the target in order to increase the conversion of the laser pulse energy to the kinetic energy of the accelerated protons. The results of unpublished investigations on black silicon and foam targets are also presented in this chapter. **Paper IV** focuses on tailoring the temporal properties of the main part of the laser pulse that affects the electric field distribution on the front surface of the target.

5.1 Front Surface Laser Machining

Paper I describes a study in which the microscopic structure of the front surface of the target was related to the properties of the proton beam. Low-energy femtosecond laser pulses were used to to machine (drill) a pit in the target, to a determined depth, prior to sending a fully amplified pulse into the preformed pit on the target to study the interaction.

It was found that shallow pits ($0.1 - 0.5$ μm) laser-machined on the front surface of a 3μm thick aluminum target reduced the proton beam divergence by a factor of three, without significantly reducing the proton cut-off energy.

Using the same laser system for the low-intensity machining pulses and the high intensity

pulses used for acceleration removes the necessity of re-aligning the machined structure. Furthermore, using femtosecond laser pulses for material machining is beneficial since such short pulses do not cause melting of the material being processed [97].

5.2 Improvement of Target Absorption

Placing nanostructures on the front surface of the target is a common way of increasing the conversion of the laser energy to hot electrons. Such structures can also be used for other purposes, such as efficient high-order harmonic or terahertz generation [98], and enhancement of X-ray production [99].

Nanostructures can be manufactured to produce regular structures, such as the nanowires described in **Paper II**, or irregular structures, such as black silicon, foams and nanoholes (**Paper III**). These structures and their performance are discussed below.

5.2.1 Black silicon

Black silicon is a common structure that is used to increase absorption on the surface of a material, and can be simply fabricated over large areas [100]. It is known for its extremely high absorption in the low–intensity regime in the spectral range corresponding to the absorption band of Si (approximately from 300 nm to 900 nm). In the work presented in this thesis the fractional absorption of black silicon was investigated at high intensity and compared to that of aluminum.

The black silicon surface was fabricated on a 0.2 mm thick silicon wafer, and the reference aluminum plate had a thickness of 1 mm. These thicknesses ensured that there was no transmission of the laser radiation through the sample, and thus the absorbed fraction is $A = 1 - R$, where R is the amount of reflected light.

A schematic illustration of the experimental setup used for these measurements is shown in Figure 5.1. The laser pulse was incident on the target at an angle of 45°. The specularly reflected light was recollimated with an off-axis parabolic mirror and sent outside the interaction chamber onto a single-shot energy meter. The light originating from diffuse reflection was collected with a lens placed in the surface–normal direction and covering a solid angle of approximately 0.2 sr and focused onto a calibrated photodiode with appropriate filters in front of it. The diffuse reflection source was assumed to be Lambertian, allowing the total energy diffusely scattered from the target to be extrapolated based on the fraction sampled by the lens.

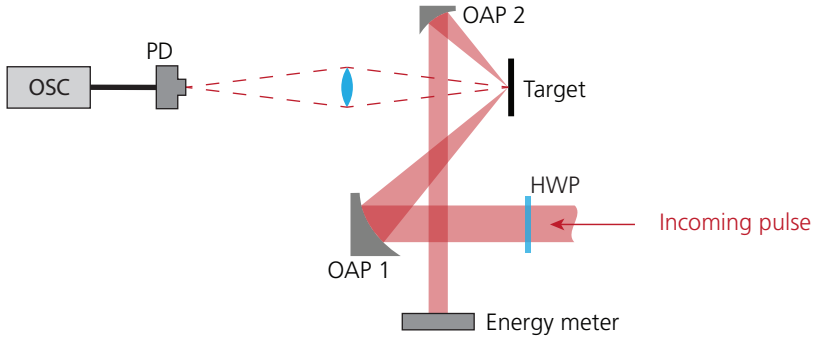

Figure 5.1: Schematic illustration of the experimental arrangement used for absorption measurements of black silicon. OAP 1 is the focusing mirror, OAP 2 is the recollimating mirror, HWP denotes the half-wave plate, and PD the photodiode, which is connected to a digital oscilloscope, OSC.

The amount of the laser pulse reflected was studied as a function of the laser pulse peak intensity on the target. The intensity was changed by moving the target along the axis of the focused laser beam, and the energy of the specularly reflected and diffusely scattered light was recorded. Measurement were made for both s– and p–polarization by rotating the half-wave plate before focusing the pulse onto the target, as shown in Figure 5.1. The total reflection is shown in figure 5.2.

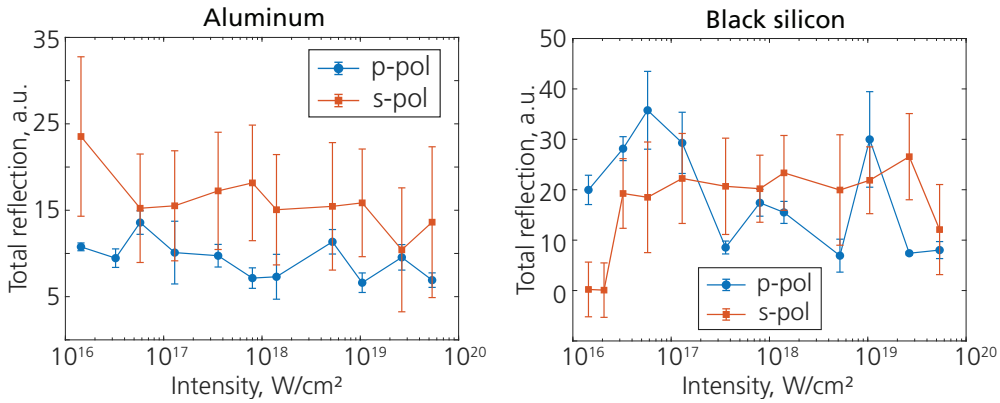

Figure 5.2: Total reflection by aluminum and black silicon.

Although the reflection is expressed in arbitrary units, it is possible to study the trends. It can be seen from Figure 5.2 that and one can observe that both black silicon and aluminum reflect very similar amounts of light at high intensities. The reflection of the aluminum sample does not change with intensity within the errors, as expected, while the reflection of p–polarized light is higher than that of s–polarized light due to the resonant absorbtion process.

Black silicon showed a less uniform behavior. In the case of a p–polarized light, there was no noticeable trend with intensity, and the dependence of the laser reflection on the light intensity seemed rather stochastic. The case of s–polarization, on the other hand, showed a more stable behavior. At higher intensities the reflected portion of the laser pulse was very similar to that observed in the case of the aluminum target, but at low intensities on the order of 10^{16} W/cm^2, it was 0.

The abrupt decrease in the reflectivity of black silicon can be attributed to the scale of the structure of black silicon, which is on the order of a few µm and the moderate contrast of the laser pulses used during this study(10^{-8} at 100 ps prior to the peak of the pulse) . At high peak intensities (i.e. tighter focus on the target surface) the pedestal and the shoulder of the pulse ionize the surface structure prior to the arrival of the main part of the laser pulse. The preplasma then expands for a longer time, causing the front surface structures to vanish. furthermore, reducing the intensity on the target in this study corresponds to a proportional increase in the irradiated area. This means that reducing the intensity of the peak of the pulse not only facilitates the survival of the fabricated structure, but also increases the amount of structural features irradiated that contribute to light absorption.

Although this study is an important step towards understanding the behavior of targets with a surface structure, it clearly shows the need for very-high-contrast laser pulses to investigate the interaction of ultra-intense laser pulses with structured targets. At the time the study was performed, the double plasma mirror was not yet available at Lund High-Power Laser Facility, but it would be interesting to repeat the study using the high-contrast pulses provided by the DPM.

5.2.2 Nanowires

High–contrast laser pulses were used to investigate the enhancement of laser-accelerated protons by regular copper nanowire structures on the front surface of the target. The details of this study are presented in **Paper II**.

The nanowire structures were defined by a set of geometric parameters such as the length of the nanowires, their diameter, and the distance between the individual nanowires. Different combinations of these parameters were investigated both numerically and experimentally to determine the values giving the best performance.

The targets were fabricated off-site and required preparation in order to transfer them to a dedicated target holder for the study of laser-solid interaction. A thick aluminum oxide layer that acted as a long-term support for the nanowires was etched away with a NaOH solution. The unsupported targets were then rinsed with distilled water, dried and mounted on the target holder, which was then placed in the experimental vacuum chamber.

A major disadvantage of this process is that water became trapped in the nanowire 'forest', and did not evaporate within even 24 hours deemed reasonable during the experimental campaign. When such a nanowire target was placed in the evacuated vacuum chamber, the water quickly evaporated, leading to destruction of the target. This problem could be solved by a longer drying time of the target or possible modification of the transfer procedure such that it is both acceptably quick and still non-destructive to the target.

Despite the complications associated with target handling, it was shown that a forest of copper nanowires on the front surface of the target increased the absorption of the laser light compared to a solid copper target of the same thickness. This resulted in a higher temperature of the electrons forming the accelerating sheath and consequently higher accelerated proton energies. The best nanowire geometry showed an enhancement of almost factor of two, compared to a solid copper target of the same thickness as the length of the nanowires.

5.2.3 Nanoholes

The study presented in **Paper III** was performed to investigate the potential of increasing the energy of the accelerated proton energy using a thin target (a few hundred nm) with a non-periodic array of perforating nanoholes. Previous simulation studies have shown that when an infinitely high-contrast laser pulse is used, such a perforated target can increase the cut-off energy of the laser-accelerated protons by almost a factor of two compared to a non-perforated target of the same composition and thickness [101]. Such targets can easily be fabricated in a cleanroom facility, and their handling does not differ from that of conventional metallic foils with sub-micron thickness, which makes their use very appealing.

In the present experimental study, the cut-off energy obtained with nanohole gold targets of different thicknesses, hole density, and hole diameter, was compared with that of unperforated gold foils. The results of the experimental study and follow-up particle-in-cell simulations suggest that despite the very high contrast of the laser pulse (10^{-8} at 1 ps prior to the peak of the pulse, see Figure 3.12), the shoulder of the laser pulse ionized the target prior to the peak of the laser pulse, and plasma expansion caused the nanohole structures to be filled with overdense plasma before the arrival of the main part of the laser pulse. This means that there was very little structural difference between the nanohole target and a flat foil when heating of the electrons took place. The enhancement predicted by the simulations was therefore not observed experimentally even with very-high-contrast laser pulses delivered by the DPM.

5.2.4 Foam Targets

Non-periodic structures are often grown on the front surface of a target, creating a porous layer with a very low (mg/cm^3) average density. One of the most common ways of making these structures is in the form of a foam [102, 103]. In theory, the low density of a uniform foam layer provides a controlled near-critical density layer of plasma interacting with the laser pulse. This should result in enhanced heating of the electrons on the front surface of the target, in turn leading to higher energies of the accelerated ions.

However, other structures than foams can be used to achieve the same effects. One such structure can be formed by growing grass-like structures of zinc oxide on the surface of an aluminum foil. The thickness of the layer is determined by the growing time. This was studied in the present work, and a scanning electron microscope image of the surface structure is shown in figure 5.3. The structures were named 'haystack targets' due to their resemblance to freshly cut grass in a meadow.

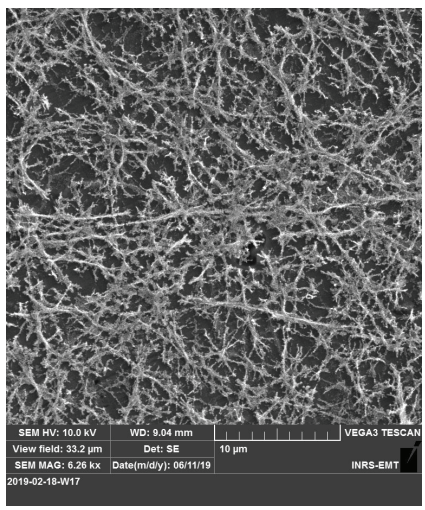

Figure 5.3: A scanning electron microscope image of the surface of a haystack target.

A range of haystack thicknesses was used, from 0 (bare Al foil) to 45 μm, and the targets were irradiated with a high-contrast laser pulse (10^{-8} at 1 ps prior to the peak of the pulse, see Figure 3.12) that reached a peak intensity of 5×10^{19} W/cm^2. The spectra of accelerated protons were recorded with the TPS, described in Section 4.4, in the forward direction, and with a magnetic dipole spectrometer in the backward direction.

Such high intensities can be achieved by very tight focusing of the laser pulse on the surface of the target. The size of the focal spot was 2.8 µm FWHM. Close examination of the structure shown in Figure 5.3 revealed that the haystack structure was not uniform on the

length scale of the focal spot, and its density can therefore not be approximated by an average density. In fact, there are empty spaces that could allow a tightly focused beam to propagate through without interacting with the hays, while the plasma density would be almost solid if the laser impinged on a solid straw in the hay structure.

This could lead to very unstable performance of the target, however, the measurements performed in the course of this work suggest that the laser-target interaction is fairly repeatable. The proton cut-off energies measured during this experiment are shown in figure 5.4.

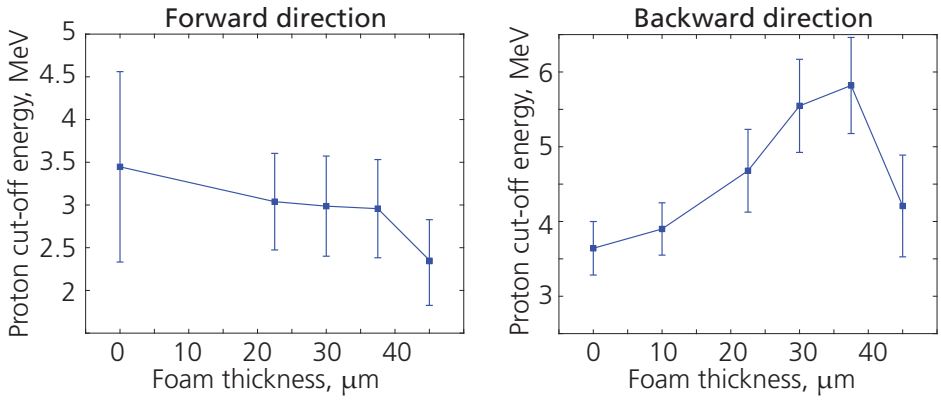

Figure 5.4: The dependence of average proton cut-off energy on the thickness of the haystack layer. The error bars represent shot-to-shot variations in the proton cut-off energy.

It can be seen that in the forward direction, the cut-off energy decreases with increasing deposited layer thickness, as expected [104, 105]. However, in the backward direction, an increase in cut-off energy is seen with increasing thickness of the haystack up to 37.5 μm, after which there is a sharp decrease.

The reason for the noticeable increase in energy of the protons accelerated in the backward direction is not yet known. However, the increase in the proton cut-off energy, proportional to the haystack thickness is in direct contrast to the behavior observed for flat foil targets in both the forward and backward directions [105].

5.3 Pulse Chirp

The effects of laser pulse chirp on protons accelerated from ultrathin carbon foils (10 nm and 100 nm) were investigated with a high contrast laser pulse. The chirp of the laser pulse was changed by varying the grating separation in the laser pulse compressor, and the

occurring asymmetries of the pulse were compensated for with the AOPDF (see Section 3.2.1). The proton cut-off energy was found to be dependent on the sign of the pulse chirp for the 100 nm target in the backward direction. In the case of 10 nm target, a strong correlation was observed between the time derivative of the pulse instantaneous wavelength and the proton cut-off energy in both the forward and backward directions. Further details can be found in **Paper IV**, but some additional observations outside of the scope of the paper are presented below.

One of these observations is the influence of the DPM on the main laser pulse. In order to determine the temporal shape of the laser pulse, as seen by the target, the laser pulse could be intercepted immediately before being focused on the target and sent to a single-shot, second-harmonic FROG measurement setup. The spectrograms were recorded and the temporal shape of the laser pulse was then retrieved.

For convenience, and to save space on the substrates of the DPM, the pulse properties (GVD and TOD) were first determined when bypassing the DPM, and the pulses were then fine–tuned when the laser propagated through the DPM. This gave the opportunity to compare the laser pulses as they leave the compressor and the way they exit the DPM. Raw FROG spectrograms are shown in Figure 5.5 for comparison.

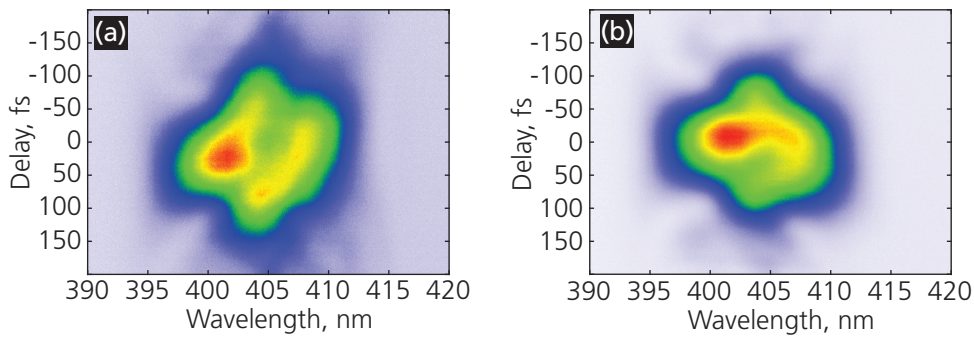

Figure 5.5: FROG traces of positively chirped pulse when it: (a) bypassing the DPM, and (b) passes through the DPM.

There is a small, but noticeable difference between the two recorded spectrograms. The retrieved temporal profiles show that the temporal shape of the laser pulses are very similar (see Figure 5.6), suggesting that the temporal modifications of the laser pulse introduced by the DPM are extremely small.

The balanced reflection/transmission detector (see Section 4.1) with Spectralon scatter screens provided complementary data on the intensity of the light, transmitted and reflected from the target. The results for the cross-calibrated measurements for the 10 nm and 100 nm targets are shown in Figure 5.7.

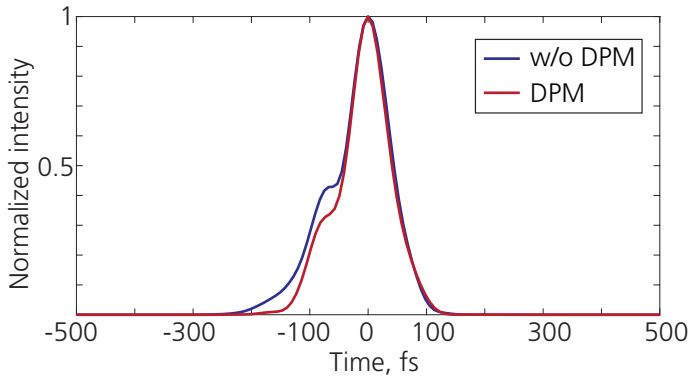

Figure 5.6: Retrieved temporal profiles of the laser pulse when bypassing and passing through the DPM.

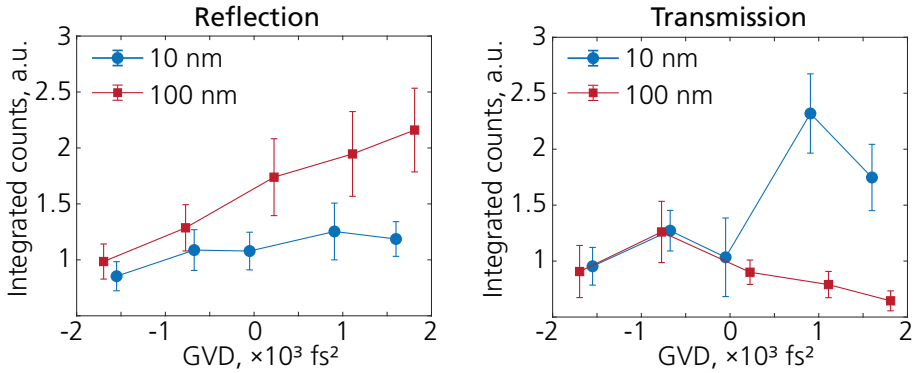

Figure 5.7: Reflection and transmission measured with the Spectralon scatter screens as a function of GVD for the 10 nm and 100 nm targets.

Despite the use of arbitrary units, it is possible to make observations related to the trends of reflection and transmission for the two different targets, however, quantitative comparisons between reflection and transmission are not possible.

The fraction of reflected light increases with increasing group velocity dispersion for both targets. In other words, less light is reflected from the target when the pulse is positively chirped than when it is transform-limited or negatively chirped, and the dependence is approximately linear. The amount of light reflected from the two targets is very similar when the pulse is positively chirped (GVD $\leqslant 0$ fs^2). However, the fraction of light reflected by the 100 nm foil increases faster than for the 10 nm foil as the GVD is increased.

The amount of light transmitted by the two different targets is almost identical when the pulse is transform-limited or positively chirped (GVD $\leqslant 0$). When GVD $\geqslant 0$ the fraction

of transmitted light is vastly different for the two targets. In the case of the 100 nm target there is a linear decrease in the transmitted light, while for the thinner target there is a two-fold increase in transmission of a slightly negatively chirped (GVD $\approx$ 900 fs^2) pulse and then decreases.

Another finding of this study is a correlation between the temporal evolution of the standing wave formed in front of the front surface of the target and the maximum kinetic energy of the protons, accelerated from the 10 nm target. The standing wave is formed in the overlap of the incident and the reflected parts of the laser pulse.

The laser pulses used in this this study were p–polarized. In order to simplify the analysis, the case of a plane wave will be considered, when it is obliquely incident on a flat perfect conductor, which is used to approximate the plasma. In this case the real part of the total electric field in the overlap can be expressed as:

$$\mathbf{E}(x,z,t) = 2E_0(\hat{\mathbf{x}}\cos\theta\sin(k_z z)\sin(\omega t - k_x x) - \hat{\mathbf{z}}\sin\theta\cos(k_z z)\cos(\omega t - k_x x)), \quad (5.1)$$

where $\hat{\mathbf{x}}$ is directed along the reflecting surface and lies in the plane of incidence, $\hat{\mathbf{z}}$ normal to the surface, and θ is the angle of incidence. The real part of the total magnetic field is expressed as:

$$\mathbf{B}(x,z,t) = \frac{2E_0}{c}\hat{\mathbf{y}}\cos(k_z z)\cos(\omega t - k_x x), \quad (5.2)$$

where $\hat{\mathbf{y}}$ points along the reflecting surface and normal to the plane of incidence, and c is the speed of light. The distribution of the magnetic field inside the overlap is rather simple. In the x direction it is a running wave, and in the z direction a standing wave. Such a standing wave has its nodes where $B = 0$, and the spacing between these nodes is $\lambda/(2\cos\theta)$.

The electric field distribution, however, is not as simple. As shown in Equation 5.1, the resulting field in the vicinity of the reflection surface will have components in the plane of incidence, and this is more easily understood when visualized as in Figure 5.8.

One can see that the z and x components of the field (Figure 5.8 a and b, respectively) are shifted by $\pi/2$ relative to each other, which means that the resulting field has circular polarization with the electric field vector rotating in the plane of incidence. In Figure 5.8c the outlines of the z and x components of the field as a function of z are plotted for different values of the oscillatory term of the resulting field. The field will be a running wave in the x direction and a standing wave in the z direction, with the nodes defined at either $E_x = 0$ or $E_z = 0$. The spacing between the nodes is once again $\lambda/(2\cos\theta)$.

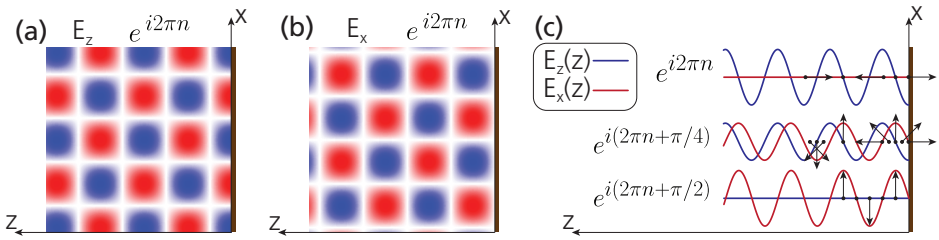

Figure 5.8: Electric fields in the overlap of the incident and the reflected plane waves in the vicinity of the reflective surface. (a) shows the z component of the resulting field, (b) the x component, and (c) outlines of both components for selected values of the oscillation term. The arrows show the direction of the total electric field in the xz coordinate space.

While the solutions given above are explicitly true for plane waves only, it is worth noting that, in general, the amplitude of the electric field E_0 is the complex amplitude, defining the spatial and temporal properties of the laser pulse. Following this consideration, for a short Gaussian laser pulse, the overlap of the laser beam upon reflection from the target surface will be finite in size and exist only for a short time. Furthermore, if the laser pulse is chirped, its instantaneous wavelength changes with time, resulting in a standing wave pattern in which the wavelength changes over time, and the nodes of the standing wave are thus moving.

Chapter 6

Conclusions and Outlook

The aim of the work presented in this thesis was to find ways of optimizing the properties of protons, accelerated by the TNSA mechanism. The properties of main interest were the maximum kinetic energy of the protons and the spatial divergence of the proton beam.

In the experiments, presented in **Paper I** the effect of laser machining of the front surface of aluminum foil targets was investigated. The study showed that machining a shallow (0.15 – 0.3 μm deep) pit in a 3 μm foil reduced the divergence of the proton beam by a factor of three, without compromising the proton cut-off energy. This decrease was attributed to a spatial modification of the accelerating sheath field. The machined pit on the front surface of the target was deemed to change the divergence of the hot electron current, in turn affecting the shape of the sheath.

A simple way of reducing the proton beam divergence, as described in **Paper I**, might be useful in the applications of laser-accelerated protons. The protons are usually focused on the point of application with solenoid or quadrupole magnets [106]. Such focusing is complicated by the high chromaticity of the laser-accelerated protons and their high divergence, and reducing the divergence directly from the source could potentially simplify the design of the magnetic lens.

The studies presented in **Papers II–III**, and unpublished studies on black silicon and foam targets, were performed to investigate the effects of nanostructures on the front surface of flat foil targets. The combined results of these studies emphasize the utmost importance of using laser pulses with sufficiently high temporal contrast to ensure the survival of the nanostructures before the arrival of the main pulse of the laser. When the nanostructures consisted of nanowires normal to the target surface, the contrast was sufficient when using the double plasma mirror, resulting in a notable increase in the electron temperature and the proton spectra cut-off energy, indicating enhanced energy conversion between the

laser pulse and the electrons (**Paper II**). Enhancement of the maximum proton energy in the backward direction was also seen in the study on the haystack targets. On the other hand, the results of the studies on black silicon and the studies reported in **Paper III**, where the nanostructures consisted of non-periodic perforations, suggest that insufficient contrast (even with the DPM) caused the manufactured structures to be filled with overdense plasma, essentially making the target appear flat before the arrival of the main part of the laser pulse.

The finding of these studies can stimulate a discussion on the use of nanostructured targets in the growing novel and exciting field of ion acceleration with petawatt-class lasers. Numerical studies have already been conducted to investigate the interaction of structured targets with such laser pulses. One study based on computer simulations has shown that placing nanospheres on the laser-irradiated surface of a thin plastic foil in the PW regime (10 PW) should increase the proton cutoff-energy from 600 to 650 MeV [107]. Another numerical study showed a 30% increase in the proton cut-off energy when hollowed thin targets were used [108], which were very similar geometrically to the targets described in **Paper III**. However, infinite laser pulse contrast was assumed in both these studies.

Compared to a 50 TW laser system, as was used in the experimental work presented in this thesis, PW peak powers require at least a twenty-fold increase in the energy of the laser pulse, assuming that the pulse duration and the focal spot size are unchanged. Thus, a corresponding increase in the temporal contrast is needed to ensure that the intensity on target remains the same before the main part of the laser pulse arrives.

There have been several successful attempts to increase the contrast of short-pulse PW lasers, for example, by modification of the front-end of the laser system [109, 110] or through the use of plasma mirrors [111]. With an appropriate front-end laser system and an optimized DPM, it has recently been shown to be possible to achieve sufficiently high laser pulse contrast for direct interaction of laser pulses with targets as thin as 10 nm [111].

The study presented in **Paper IV** revealed that with sufficiently high temporal contrast of the laser pulse and a very thin (10 nm) amorphous carbon foil target, there is a correlation between the rate of change (i.e. time derivative) of the instantaneous wavelength, averaged over the duration of the pulse, and the maximum kinetic energy of laser-accelerated protons. This directly implies that the temporal properties of the main laser pulse influence the laser-driven ion acceleration beyond 'simply' the contrast of the laser pulse, and the electric field of the main part of the pulse may play a significant role, affecting the ion acceleration with ultrathin targets. The effects found experimentally and discussed in **Paper IV** indicate a possible branch of studies dedicated to the interaction of tailored laser pulses with solids, and can potentially be of great interest when further explored using intense few-cycle pulses.

The field of laser-driven ion acceleration is still young, and has only been closely investig-

ated for the past two decades, with target manufacturing techniques and laser development going hand-in-hand. However, despite the best efforts, TNSA still remains a rather inefficient process, and no really significant breakthroughs have been achieved. The conversion efficiency of laser energy to the kinetic energy of the protons, in a simple scenario consisting of a flat target and a single transform-limited pulse, does not typically exceed 4% [112]. The laser-to-electron energy conversion can be as high as 70% [38], and the major part is thus lost in the electron to ion energy exchange.

It is the author's opinion that further investigations into ways of enhancing the efficiency of the TNSA process should focus on increasing the efficiency of the energy transfer between the hot electrons and the ions. This could be done by either spatially confining the electron sheath, or by increasing the time during which ion acceleration takes place.

However, it is possible that completely new laser-based acceleration mechanisms will prove to be inherently more efficient than TNSA (for example, radiation pressure acceleration), and will dominate the field in the future. Such mechanisms will come hand-in-hand with the development of more advanced laser systems that can provide higher temporal contrast, shorter pulse duration and higher peak power, and will allow for a broad range of means to tailor the laser pulses.

The Author's Contributions

The experiments presented in this thesis were conducted at the Lund High-Power Laser Facility using the Lund multi-TW laser system. I played an active part in the optimization, development and characterization of this laser system, as well as its day-to-day operation. Likewise, I participated in the development and maintenance of the laser system and the laser-plasma laboratory.

Paper I: Influence of micromachined targets on laser accelerated proton beam profiles

I took an active part in developing the idea of the experiment, designing and setting up the experiment, including the low-energy laser-machining involving the estimation of the appropriate energy of the machining pulses, data processing and analysis, and took an active part discussions on the manuscript.

Paper II: Enhanced laser-driven proton acceleration using nanowire targets

I played active part in preparing and conducting the experiment, my main contribution being the optimization of the double plasma mirror set-up and ensuring the reliably high contrast of the laser pulses. The Thomson parabola ion spectrometer was used for the first time in this study. I designed this spectrometer, and performed its assembly and calibration. I developed the code for data processing and analyzed the spectra of the protons accelerated in the forward direction, acquired by the Thomson parabola spectrometer. I also took an active part in discussions of the manuscript.

Paper III: Laser-driven proton acceleration from ultrathin foils with nanoholes

I took an active part in preparing and conducting the experiment, processing and analyzing the data obtained for the protons accelerated in the forward direction, and in discussions on the manuscript.

Paper IV: Effects of pulse chirp on laser-driven proton acceleration

I designed the experiment, including the high-power FROG setup for the pulse characterization and means of monitoring the repeatability of the laser pulse properties. I took an active part in conducting the experiment, performed the analysis of the data from the Thomson parabola spectrometer, resulting from the forward accelerated protons, and wrote the draft of the manuscript.

Acknowledgments

As a foreword, I would like to say that the (almost) five years I spent at Atomic Physics were many things: light, tedious, and sometimes pushing me to the limit, but most importantly, every moment has been fun, thanks to all the people who surrounded me and whose support I felt every day.

Firstly, I would like to express my gratitude to my supervisors Professor Claes-Göran Wahlström and Dr. Olle Lundh for hiring me in the first place, and, more importantly, for always being ready to help me with questions and concerns about science and research, or life in general. Working in the 'High Intensity' group has meant a lot to me, and I am grateful that I had the opportunity to work with each of them.

I would also like to thank Henrik Ekerfelt for putting up with me in the same office for over two years, and for being understanding when I was acting bitter after he "moved out" to write his thesis; Malay Dalui, Hannes Pahl, Lovisa Senje, and Kristoffer Svensson for showing me the ropes in the lab; Diego Guenot, for teaching me how to count and be arrogant in French, and all his help with the setup alignment; Martin Hansson, for teaching me how to operate gas reducer valves and all of his work with the DPM; Kristoffer Svendsen, for all his help in the lab and for always being there to share and listen to my complaints. I would also like to thank Isabel Gallardo Gonsález, Jonas Björklund-Svensson, and Cornelia Gustafsson for always keeping a relaxed and friendly atmosphere within the group.

I would like to thank Anders Persson for taking me on lunch trips to Biltema and Swedol and always be supportive of my fascinating and mostly very safe ideas with advice and all the power tools in the world. Also, I would like to express my gratitude to Giada Cantono. During the years we have worked together she has truly become my sister-in-arms in the field of proton acceleration. Every mirror we turned, every camera we burned, every time we stayed after midnight to finish a measurement, I've always felt her shoulder right next to mine, and this has made me a better scientist, and a better person.

I have been lucky enough to collaborate with great scientists from all around the world. This was made possible by the PLIONA project, which connected me with the great people

working with us in Gothenburg and Umeå: Julien Ferri, Illia Thiele, Arkady Gonoskov, Evgeniya Smetanina, Tünde Fülöp, and others. I would also like to thank our collaborators who participated in the experimental campaigns with us: Simon Vallières, Martina Salvadori, Fabrizio Consoli and Patrizio Antici.

Thanks to everyone at Atomic Physics who made it feel like a second home and made me feel that I belonged here. Speaking of home, I would like to thank Jan for deciding that living under the same roof with me is a great idea, and then to David and Anne-Lise for deciding the same and not regretting it (so far) after Jan moved away. You have been fabulous flat mates, and I never had to feel that I was returning to a cold house when you were there. I'd like to thank the atto-group: Hugo, Robin, Mattias, Lana, Marius, Jasper, Maria, Hampus, Neven, Emma, and Chen for always being ready to help, discussing anything in the world, and joining after-work activities after long and tough days of doing research. Thank you Anne P-J, Jakob and Åke for taking care of administration and computer problems when I was clueless about what to do.

Thank you, Ivan, for forming the Russian crew with me, and David for joining it despite being so French. You guys have supported me in many questionable endeavors outside of work, and all of them were much more fun with you around.

Thanks to everyone in the Division of Atomic Physics for the relaxed and welcoming atmosphere in the coffee room, for occasional chats in the corridor, the Monday cake, and the Christmas dinner.

I also want to thank my closest friends from school for always being supportive of my career and life choices, sometimes pretending to understand what my research was about, and for giving me tips on how to write code in a readable way.

Finally, I want to thank my family for always being there for me. I strongly believe that the upbringing that I got made me the person I am now, and for that I will be eternally grateful.

References

[1] S. A. Johansson, J. L. Campbell, and K. G. Malmqvist. *Particle-induced X-ray emission spectrometry (PIXE)*, volume 133. Wiley New York (1995).

[2] M. Roth, T. Cowan, M. Key, S. Hatchett, C. Brown, W. Fountain, J. Johnson, D. Pennington, R. Snavely, S. Wilks, *et al. Fast ignition by intense laser-accelerated proton beams*. Physical Review Letters, 86(3):436 (2001).

[3] D. Schulz-Ertner and H. Tsujii. *Particle radiation therapy using proton and heavier ion beams*. Journal of Clinical Oncology, 25(8):953–964 (2007).

[4] P. Maine, D. Strickland, P. Bado, M. Pessot, and G. Mourou. *Generation of ultrahigh peak power pulses by chirped pulse amplification*. IEEE Journal of Quantum Electronics, 24(2):398–403 (1988).

[5] U. Schramm, M. Bussmann, A. Irman, M. Siebold, K. Zeil, D. Albach, C. Bernert, S. Bock, F. Brack, J. Branco, *et al. First results with the novel petawatt laser acceleration facility in Dresden*. In *Journal of Physics: Conference Series*, volume 874, page 012028. IOP Publishing (2017).

[6] Y. Chu, X. Liang, L. Yu, Y. Xu, L. Xu, L. Ma, X. Lu, Y. Liu, Y. Leng, R. Li, *et al. High-contrast 2.0 Petawatt Ti: sapphire laser system*. Optics Express, 21(24):29231–29239 (2013).

[7] D. Doria, M. Cernaianu, P. Ghenuche, D. Stutman, K. Tanaka, C. Ticos, and C. Ur. *Overview of ELI-NP status and laser commissioning experiments with 1 PW and 10 PW class-lasers*. Journal of Instrumentation, 15(09):C09053 (2020).

[8] P. Sprangle, G. Joyce, E. Esarey, and A. Ting. *Laser wakefield acceleration and relativstic optical guiding*. In *AIP Conference Proceedings*, volume 175, pages 231–239. American Institute of Physics (1988).

[9] F. Amiranoff, S. Baton, D. Bernard, B. Cros, D. Descamps, F. Dorchies, F. Jacquet, V. Malka, J. Marques, G. Matthieussent, *et al. Observation of laser wakefield acceleration of electrons*. Physical Review Letters, 81(5):995 (1998).

[10] A. Gonsalves, K. Nakamura, J. Daniels, C. Benedetti, C. Pieronek, T. De Raadt, S. Steinke, J. Bin, S. Bulanov, J. Van Tilborg, *et al. Petawatt laser guiding and electron beam acceleration to 8 GeV in a laser-heated capillary discharge waveguide*. Physical Review Letters, 122(8):084801 (2019).

[11] R. Snavely, M. Key, S. Hatchett, T. Cowan, M. Roth, T. Phillips, M. Stoyer, E. Henry, T. Sangster, M. Singh, *et al. Intense high-energy proton beams from petawatt-laser irradiation of solids*. Physical Review Letters, 85(14):2945 (2000).

[12] A. Maksimchuk, S. Gu, K. Flippo, D. Umstadter, and V. Y. Bychenkov. *Forward ion acceleration in thin films driven by a high-intensity laser*. Physical Review Letters, 84(18):4108 (2000).

[13] M. Borghesi. *Ion Acceleration: TNSA and Beyond*. In L. A. Gizzi, R. Assmann, P. Koester, and A. Giulietti, editors, *Laser-Driven Sources of High Energy Particles and Radiation*, pages 143–164. Springer International Publishing (2019).

[14] F. Wagner, O. Deppert, C. Brabetz, P. Fiala, A. Kleinschmidt, P. Poth, V. Schanz, A. Tebartz, B. Zielbauer, M. Roth, *et al. Maximum proton energy above 85 MeV from the relativistic interaction of laser pulses with micrometer thick CH2 targets*. Physical Review Letters, 116(20):205002 (2016).

[15] A. Higginson, R. J. Gray, M. King, R. J. Dance, S. D. R. Williamson, N. M. H. Butler, R. Wilson, R. Capdessus, C. Armstrong, J. S. Green, *et al. Near-100 MeV protons via a laser-driven transparency-enhanced hybrid acceleration scheme*. Nature Communications, 9(1):1–9 (2018).

[16] B. Dromey, M. Coughlan, L. Senje, M. Taylor, S. Kuschel, B. Villagomez-Bernabe, R. Stefanuik, G. Nersisyan, L. Stella, J. Kohanoff, *et al. Picosecond metrology of laser-driven proton bursts*. Nature Communications, 7(1):1–6 (2016).

[17] M. Borghesi, A. Mackinnon, D. H. Campbell, D. Hicks, S. Kar, P. K. Patel, D. Price, L. Romagnani, A. Schiavi, and O. Willi. *Multi-MeV proton source investigations in ultraintense laser-foil interactions*. Physical Review Letters, 92(5):055003 (2004).

[18] C. Palmer, P. Campbell, Y. Ma, L. Antonelli, A. Bott, G. Gregori, J. Halliday, Y. Katzir, P. Kordell, K. Krushelnick, *et al. Field reconstruction from proton radiography of intense laser driven magnetic reconnection*. Physics of Plasmas, 26(8):083109 (2019).

[19] M. Borghesi, G. Sarri, C. Cecchetti, I. Kourakis, D. Hoarty, R. Stevenson, S. James, C. Brown, P. Hobbs, J. Lockyear, *et al. Progress in proton radiography for diagnosis of ICF-relevant plasmas*. Laser and Particle Beams, 28(2):277–284 (2010).

[20] G. Voronov and N. Delone. *Ionization of the xenon atom by the electric field of ruby laser emission*. Soviet Journal of Experimental and Theoretical Physics Letters, 1:66 (1965).

[21] P. Agostini, F. Fabre, G. Mainfray, G. Petite, and N. K. Rahman. *Free-free transitions following six-photon ionization of xenon atoms*. Physical Review Letters, 42(17):1127 (1979).

[22] P. Kruit, J. Kimman, H. Muller, and M. Van der Wiel. *Electron spectra from multiphoton ionization of xenon at 1064, 532, and 355 nm*. Physical Review A, 28(1):248 (1983).

[23] P. Gibbon. *Short pulse laser interactions with matter: an introduction*. World Scientific (2005).

[24] W. Kruer. *The physics of laser plasma interactions*. CRC Press (2019).

[25] E. Startsev and C. McKinstrie. *Multiple scale derivation of the relativistic ponderomotive force*. Physical Review E, 55(6):7527 (1997).

[26] M. Zepf, M. Castro-Colin, D. Chambers, S. Preston, J. Wark, J. Zhang, C. Danson, D. Neely, P. Norreys, A. Dangor, *et al. Measurements of the hole boring velocity from Doppler shifted harmonic emission from solid targets*. Physics of Plasmas, 3(9):3242–3244 (1996).

[27] S. Wilks, W. Kruer, M. Tabak, and A. Langdon. *Absorption of ultra-intense laser pulses*. Physical Review Letters, 69(9):1383 (1992).

[28] Y. Ping, A. Kemp, L. Divol, M. Key, P. Patel, K. Akli, F. Beg, S. Chawla, C. Chen, R. Freeman, *et al. Dynamics of relativistic laser-plasma interaction on solid targets*. Physical Review Letters, 109(14):145006 (2012).

[29] G. Kemp, A. Link, Y. Ping, H. McLean, P. Patel, R. Freeman, D. Schumacher, H. Tiedje, Y. Tsui, R. Ramis, *et al. On specular reflectivity measurements in high and low-contrast relativistic laser-plasma interactions*. Physics of Plasmas, 22(1):013110 (2015).

[30] J. Freidberg, R. Mitchell, R. L. Morse, and L. Rudsinski. *Resonant absorption of laser light by plasma targets*. Physical Review Letters, 28(13):795 (1972).

[31] F. Beg, A. Bell, A. Dangor, C. Danson, A. Fews, M. Glinsky, B. Hammel, P. Lee, P. Norreys, and M. Tatarakis. *A study of picosecond laser–solid interactions up to* 10^{19} *W cm-2*. Physics of Plasmas, 4(2):447–457 (1997).

[32] N. Denisov. *On a singularity of the field of an electromagnetic wave propagated in an inhomogeneous plasma*. Soviet Physics JETP-USSR, 4(4):544–553 (1957).

[33] F. Brunel. *Not-so-resonant, resonant absorption*. Physical Review Letters, 59(1):52 (1987).

[34] P. Gibbon and A. Bell. *Collisionless absorption in sharp-edged plasmas*. Physical Review Letters, 68(10):1535 (1992).

[35] W. Kruer and K. Estabrook. *J× B heating by very intense laser light*. The Physics of Fluids, 28(1):430–432 (1985).

[36] G. Malka and J. Miquel. *Experimental confirmation of ponderomotive-force electrons produced by an ultrarelativistic laser pulse on a solid target*. Physical Review Letters, 77(1):75 (1996).

[37] M. Santala, M. Zepf, I. Watts, F. Beg, E. Clark, M. Tatarakis, K. Krushelnick, A. Dangor, T. McCanny, I. Spencer, *et al. Effect of the plasma density scale length on the direction of fast electrons in relativistic laser-solid interactions*. Physical Review Letters, 84(7):1459 (2000).

[38] Y. Ping, R. Shepherd, B. Lasinski, M. Tabak, H. Chen, H. Chung, K. Fournier, S. Hansen, A. Kemp, D. Liedahl, *et al. Absorption of short laser pulses on solid targets in the ultrarelativistic regime*. Physical Review Letters, 100(8):085004 (2008).

[39] A. Robinson, M. Zepf, S. Kar, R. Evans, and C. Bellei. *Radiation pressure acceleration of thin foils with circularly polarized laser pulses*. New Journal of Physics, 10(1):013021 (2008).

[40] A. Henig, S. Steinke, M. Schnürer, T. Sokollik, R. Hörlein, D. Kiefer, D. Jung, J. Schreiber, B. Hegelich, X. Yan, *et al. Radiation-pressure acceleration of ion beams driven by circularly polarized laser pulses*. Physical Review Letters, 103(24):245003 (2009).

[41] L. O. Silva, M. Marti, J. R. Davies, R. A. Fonseca, C. Ren, F. S. Tsung, and W. B. Mori. *Proton shock acceleration in laser-plasma interactions*. Physical Review Letters, 92(1):015002 (2004).

[42] A. Henig, D. Kiefer, M. Geissler, S. G. Rykovanov, R. Ramis, R. Hörlein, J. Osterhoff, Z. Major, L. Veisz, S. Karsch, *et al. Laser-driven shock acceleration of ion beams from spherical mass-limited targets*. Physical Review Letters, 102(9):095002 (2009).

[43] L. Yin, B. Albright, B. Hegelich, and J. Fernández. *GeV laser ion acceleration from ultrathin targets: The laser break-out afterburner*. Laser and Particle Beams, 24(2):291–298 (2006).

[44] D. Jung, L. Yin, D. Gautier, H.-C. Wu, S. Letzring, B. Dromey, R. Shah, S. Palaniyappan, T. Shimada, R. Johnson, *et al. Laser-driven 1 GeV carbon ions from preheated diamond targets in the break-out afterburner regime*. Physics of Plasmas, 20(8):083103 (2013).

[45] S. Wilks, A. Langdon, T. Cowan, M. Roth, M. Singh, S. Hatchett, M. Key, D. Pennington, A. MacKinnon, and R. Snavely. *Energetic proton generation in ultra-intense laser–solid interactions*. Physics of Plasmas, 8(2):542–549 (2001).

[46] M. Passoni, L. Bertagna, and A. Zani. *Target normal sheath acceleration: theory, comparison with experiments and future perspectives*. New Journal of Physics, 12(4):045012 (2010).

[47] R. Stephens, R. Snavely, Y. Aglitskiy, F. Amiranoff, C. Andersen, D. Batani, S. Baton, T. Cowan, R. Freeman, T. Hall, *et al. Kα fluorescence measurement of relativistic electron transport in the context of fast ignition*. Physical Review E, 69(6):066414 (2004).

[48] A. Mackinnon, Y. Sentoku, P. Patel, D. Price, S. Hatchett, M. Key, C. Andersen, R. Snavely, and R. Freeman. *Enhancement of proton acceleration by hot-electron recirculation in thin foils irradiated by ultraintense laser pulses*. Physical Review Letters, 88(21):215006 (2002).

[49] Y. Lyubarsky. *On the relativistic magnetic reconnection*. Monthly Notices of the Royal Astronomical Society, 358(1):113–119 (2005).

[50] R. Jung, J. Osterholz, K. Löwenbrück, S. Kiselev, G. Pretzler, A. Pukhov, O. Willi, S. Kar, M. Borghesi, W. Nazarov, *et al. Study of electron-beam propagation through preionized dense foam plasmas*. Physical Review Letters, 94(19):195001 (2005).

[51] P. McKenna, D. Neely, R. Bingham, and D. Jaroszynski. *Laser-plasma interactions and applications*. Springer (2013).

[52] T. Ceccotti, A. Lévy, H. Popescu, F. Réau, P. d'Oliveira, P. Monot, J. Geindre, E. Lefebvre, and P. Martin. *Proton acceleration with high-intensity ultrahigh-contrast laser pulses*. Physical Review Letters, 99(18):185002 (2007).

[53] P. Mora. *Plasma expansion into a vacuum*. Physical Review Letters, 90(18):185002 (2003).

[54] J. Fuchs, Y. Sentoku, E. d'Humières, T. Cowan, J. Cobble, P. Audebert, A. Kemp, A. Nikroo, P. Antici, E. Brambrink, *et al. Comparative spectra and efficiencies of ions laser-accelerated forward from the front and rear surfaces of thin solid foils*. Physics of Plasmas, 14(5):053105 (2007).

[55] A. Flacco, F. Sylla, M. Veltcheva, M. Carrié, R. Nuter, E. Lefebvre, D. Batani, and V. Malka. *Dependence on pulse duration and foil thickness in high-contrast-laser proton acceleration*. Physical Review E, 81(3):036405 (2010).

[56] J. Schreiber, F. Bell, F. Grüner, U. Schramm, M. Geissler, M. Schnürer, S. Ter-Avetisyan, B. Hegelich, J. Cobble, E. Brambrink, *et al. Analytical model for ion acceleration by high-intensity laser pulses*. Physical Review Letters, 97(4):045005 (2006).

[57] B. Aurand, L. Senje, K. Svensson, M. Hansson, A. Higginson, A. Gonoskov, M. Marklund, A. Persson, O. Lundh, D. Neely, *et al. Manipulation of the spatial distribution of laser-accelerated proton beams by varying the laser intensity distribution*. Physics of Plasmas, 23(2):023113 (2016).

[58] M. Afshari, J. Hornung, A. Kleinschmidt, P. Neumayer, D. Bertini, and V. Bagnoud. *Proton acceleration via the TNSA mechanism using a smoothed laser focus*. AIP Advances, 10(3):035023 (2020).

[59] C. Brabetz, S. Busold, T. Cowan, O. Deppert, D. Jahn, O. Kester, M. Roth, D. Schumacher, and V. Bagnoud. *Laser-driven ion acceleration with hollow laser beams*. Physics of Plasmas, 22(1):013105 (2015).

[60] V. A. Vshivkov, N. M. Naumova, F. Pegoraro, and S. Bulanov. *Nonlinear electrodynamics of the interaction of ultra-intense laser pulses with a thin foil*. Physics of Plasmas, 5(7):2727–2741 (1998).

[61] A. Macchi. *A superintense laser-plasma interaction theory primer*. Springer Science & Business Media (2013).

[62] J.-C. Chanteloup. *Multiple-wave lateral shearing interferometry for wave-front sensing*. Applied Optics, 44:1559–1571 (2005).

[63] A. V. Kudryashov, V. V. Samarkin, A. L. Rukosuev, and A. Alexandrov. *High-power lasers and adaptive optics*. volume 5333, pages 45–52. International Society for Optics and Photonics (2004).

[64] R. Trebino, K. W. DeLong, D. N. Fittinghoff, J. N. Sweetser, M. A. Krumbügel, B. A. Richman, and D. J. Kane. *Measuring ultrashort laser pulses in the time-frequency domain using frequency-resolved optical gating*. Review of Scientific Instruments, 68(9):3277–3295 (1997).

[65] N. C. Geib, M. Zilk, T. Pertsch, and F. Eilenberger. *Common pulse retrieval algorithm: a fast and universal method to retrieve ultrashort pulses*. Optica, 6(4):495–505 (2019).

[66] F. Verluise, V. Laude, Z. Cheng, C. Spielmann, and P. Tournois. *Amplitude and phase control of ultrashort pulses by use of an acousto-optic programmable dispersive filter: pulse compression and shaping*. Optics Letters, 25:575–577 (2000).

[67] T. Oksenhendler, S. Coudreau, N. Forget, V. Crozatier, S. Grabielle, R. Herzog, O. Gobert, and D. Kaplan. *Self-referenced spectral interferometry*. Applied Physics B, 99:7–12 (2010).

[68] A. Moulet, S. Grabielle, C. Cornaggia, N. Forget, and T. Oksenhendler. *Single-shot, high-dynamic-range measurement of sub-15 fs pulses by self-referenced spectral interferometry*. Optics Letters, 35:3856–3858 (2010).

[69] T. Oksenhendler, P. Bizouard, O. Albert, S. Bock, and U. Schramm. *High dynamic, high resolution and wide range single shot temporal pulse contrast measurement*. Optics Express, 25:12588–12600 (2017).

[70] A. Lévy, T. Ceccotti, P. D'Oliveira, F. Réau, M. Perdrix, F. Quéré, P. Monot, M. Bougeard, H. Lagadec, P. Martin, *et al. Double plasma mirror for ultrahigh temporal contrast ultraintense laser pulses*. Optics Letters, 32(3):310–312 (2007).

[71] T. Wittmann, J. Geindre, P. Audebert, R. S. Marjoribanks, J.-P. Rousseau, F. Burgy, D. Douillet, T. Lefrou, K. T. Phuoc, and J.-P. Chambaret. *Towards ultrahigh-contrast ultraintense laser pulses—complete characterization of a double plasma-mirror pulse cleaner*. Review of Scientific Instruments, 77:083109 (2006).

[72] G. Doumy, F. Quéré, O. Gobert, M. Perdrix, P. Martin, P. Audebert, J. C. Gauthier, J.-P. Geindre, and T. Wittmann. *Complete characterization of a plasma mirror for the production of high-contrast ultraintense laser pulses*. Physical Review E, 69:026402 (2004).

[73] B. Dromey, S. Kar, M. Zepf, and P. Foster. *The plasma mirror—a subpicosecond optical switch for ultrahigh power lasers*. Review of Scientific Instruments, 75:645–649 (2004).

[74] G. Scott, V. Bagnoud, C. Brabetz, R. Clarke, J. Green, R. Heathcote, H. Powell, B. Zielbauer, T. Arber, P. McKenna, *et al. Optimization of plasma mirror reflectivity and optical quality using double laser pulses*. New Journal of Physics, 17(3):033027 (2015).

[75] A. Lévy. *Accélération d'ions par interaction laser-matière en régime de ultra haut contraste laser*. Ph.D. thesis, Université Paris Sud-Paris XI (2008).

[76] Y. Cai, W. Wang, C. Xia, J. Liu, L. Liu, C. Wang, Y. Xu, Y. Leng, R. Li, and Z. Xu. *Time-resolved measurements on reflectivity of an ultrafast laser-induced plasma mirror*. Physics of Plasmas, 16:103104 (2009).

[77] A. Leblanc, A. Denoeud, L. Chopineau, G. Mennerat, P. Martin, and F. Quéré. *Plasma holograms for ultrahigh-intensity optics*. Nature Physics, 13:440–443 (2017).

[78] R. Wilson, M. King, R. J. Gray, D. C. Carroll, R. J. Dance, C. Armstrong, S. J. Hawkes, R. J. Clarke, D. J. Robertson, and D. Neely. *Ellipsoidal plasma mirror focusing of high power laser pulses to ultra-high intensities*. Physics of Plasmas, 23:033106 (2016).

[79] H.-E. Tsai, A. V. Arefiev, J. M. Shaw, D. J. Stark, X. Wang, R. Zgadzaj, and M. C. Downer. *Self-aligning concave relativistic plasma mirror with adjustable focus*. Physics of Plasmas, 24:013106 (2017).

[80] B. Aurand, M. Hansson, L. Senje, K. Svensson, A. Persson, D. Neely, O. Lundh, and C.-G. Wahlström. *A setup for studies of laser-driven proton acceleration at the Lund Laser Centre*. Laser and Particle Beams, 33(1):59–64 (2015).

[81] L. Senje. *Detector development, source characterization and novel applications of laser ion acceleration*. Ph.D. thesis (2017).

[82] K. Svensson. *Experiments on laser-based particle acceleration: Beams of energetic electrons and protons*. Ph.D. thesis (2016).

[83] J. J. Thomson. *Rays of positive electricity*. The London, Edinburgh, and Dublin Philosophical Magazine and Journal of Science, 21(122):225–249 (1911).

[84] D. C. Carroll, K. Jones, L. Robson, P. McKenna, S. Bandyopadhyay, P. Brummitt, D. Neely, F. Lindau, O. Lundh, and C. G. Wahlström. *The design, development and use of a novel Thomson spectrometer for high resolution ion detection*. High Power Laser Science, Short Pulse Plasma Physics, Central Laser Facility Annual Report,(2005/2006), pages 16–20 (2006).

[85] D. Gwynne, S. Kar, D. Doria, H. Ahmed, M. Cerchez, J. Fernandez, R. J. Gray, J. S. Green, F. Hanton, and D. A. MacLellan. *Modified Thomson spectrometer design for high energy, multi-species ion sources*. Review of Scientific Instruments, 85:033304 (2014).

[86] J. Cobble, K. Flippo, D. Offermann, F. Lopez, J. Oertel, D. Mastrosimone, S. Letzring, and N. Sinenian. *High-resolution Thomson parabola for ion analysis*. Review of Scientific Instruments, 82(11):113504 (2011).

[87] S. Tata, A. Mondal, S. Sarkar, A. D. Lad, and M. Krishnamurthy. *A gated Thomson parabola spectrometer for improved ion and neutral atom measurements in intense laser produced plasmas*. Review of Scientific Instruments, 88:083305 (2017).

[88] F. Schillaci, M. Maggiore, A. Velyhan, G. A. P. Cirrone, G. Cuttone, D. Margarone, G. P. Palumbo, P. Pisciotta, D. Rifuggiato, and F. Romano. *Calibration and energy resolution study of a high dispersive power Thomson Parabola Spectrometer with monochromatic proton beams*. Journal of Instrumentation, 9:T10003 (2014).

[89] R. W. Pryor. *Multiphysics modeling using COMSOL®: a first principles approach*. Jones & Bartlett Publishers (2009).

[90] `https://www.comsol.com/comsol-multiphysics` (2021). [Online; accessed 2021-08-04].

[91] P. Bellido, M. Seimetz, R. Lera, A. R. de la Cruz, S. Torres-Peiró, A. J. González, F. Sánchez, L. Roso, and J. M. Benlloch. *Design of a Thomson parabola spectrometer for the detection of laser-accelerated protons and ions*. pages 1–4. IEEE (2015).

[92] A. Mančić, J. Fuchs, P. Antici, S. Gaillard, and P. Audebert. *Absolute calibration of photostimulable image plate detectors used as (0.5–20 MeV) high-energy proton detectors*. Review of Scientific Instruments, 79(7):073301 (2008).

[93] K. Harres, M. Schollmeier, E. Brambrink, P. Audebert, A. Blažević, K. Flippo, D. Gautier, M. Geißel, B. Hegelich, F. Nürnberg, *et al. Development and calibration of a Thomson parabola with microchannel plate for the detection of laser-accelerated MeV ions*. Review of Scientific Instruments, 79(9):093306 (2008).

[94] R. Prasad, D. Doria, S. Ter-Avetisyan, P. S. Foster, K. E. Quinn, L. Romagnani, C. M. Brenner, J. S. Green, P. Gallegos, and M. J. V. Streeter. *Calibration of Thomson parabola—MCP assembly for multi-MeV ion spectroscopy*. Nuclear Instruments and Methods in Physics Research Section A: Accelerators, Spectrometers, Detectors and Associated Equipment, 623:712–715 (2010).

[95] R. Weber, J. E. Balmer, and P. Lädrach. *Thomson parabola time-of-flight ion spectrometer*. Review of scientific instruments, 57:1251–1253 (1986).

[96] G. A. P. Cirrone, A. Tramontana, G. Candiano, M. Carpinelli, S. Cavallaro, M. Cutroneo, G. Cuttone, C. D. Martinis, D. Giove, and J. Krása. *A new Thomson Spectrometer for high energy laser-driven beams diagnostic*. Journal of Instrumentation, 9:T08001 (2014).

[97] C. Momma, B. N. Chichkov, S. Nolte, F. von Alvensleben, A. Tünnermann, H. Welling, and B. Wellegehausen. *Short-pulse laser ablation of solid targets*. Optics Communications, 129(1-2):134–142 (1996).

[98] L. Fedeli, A. Formenti, L. Cialfi, A. Sgattoni, G. Cantono, and M. Passoni. *Structured targets for advanced laser-driven sources*. Plasma Physics and Controlled Fusion, 60(1):014013 (2017).

[99] R. Hollinger, C. Bargsten, V. N. Shlyaptsev, V. Kaymak, A. Pukhov, M. G. Capeluto, S. Wang, A. Rockwood, Y. Wang, A. Townsend, *et al. Efficient picosecond x-ray pulse generation from plasmas in the radiation dominated regime*. Optica, 4(11):1344–1349 (2017).

[100] X. Liu, P. R. Coxon, M. Peters, B. Hoex, J. M. Cole, and D. J. Fray. *Black silicon: fabrication methods, properties and solar energy applications*. Energy and Environmental Science, 7(10):3223–3263 (2014).

[101] J. Ferri, I. Thiele, E. Siminos, L. Gremillet, E. Smetanina, A. Dmitriev, G. Cantono, C.-G. Wahlström, and T. Fülöp. *Enhancement of laser-driven ion acceleration in non-periodic nanostructured targets*. Journal of Plasma Physics, 86(1) (2020).

[102] I. Prencipe, A. Sgattoni, D. Dellasega, L. Fedeli, L. Cialfi, I. W. Choi, I. J. Kim, K. A. Janulewicz, K. Kakolee, H. W. Lee, *et al. Development of foam-based layered targets for laser-driven ion beam production*. Plasma Physics and Controlled Fusion, 58(3):034019 (2016).

[103] M. Passoni, A. Zani, A. Sgattoni, D. Dellasega, A. Macchi, I. Prencipe, V. Floquet, P. Martin, T. Liseykina, and T. Ceccotti. *Energetic ions at moderate laser intensities using foam-based multi-layered targets*. Plasma Physics and Controlled Fusion, 56(4):045001 (2014).

[104] J. Fuchs, P. Antici, E. d'Humières, E. Lefebvre, M. Borghesi, E. Brambrink, C. Cecchetti, M. Kaluza, V. Malka, M. Manclossi, *et al. Laser-driven proton scaling laws and new paths towards energy increase*. Nature Physics, 2(1):48–54 (2006).

[105] S. Fourmaux, S. Buffechoux, B. Albertazzi, D. Capelli, A. Lévy, S. Gnedyuk, L. Lecherbourg, P. Lassonde, S. Payeur, P. Antici, *et al. Investigation of laser-driven proton acceleration using ultra-short, ultra-intense laser pulses*. Physics of Plasmas, 20(1):013110 (2013).

[106] I. Hofmann. *Performance of solenoids versus quadrupoles in focusing and energy selection of laser accelerated protons*. Physical Review Special Topics-Accelerators and Beams, 16(4):041302 (2013).

[107] M. Martiş, O. Budrigă, E. d'Humières, L. Ionel, and M. Carabaş. *Modeling the interaction of an ultra-high intensity laser pulse with an ultra-thin nanostructured foil target*. Plasma Physics and Controlled Fusion, 62(9):095014 (2020).

[108] J. Psikal and M. Matys. *Ultra-intense laser interaction with specially-designed targets as a source of energetic protons*. In *Research Using Extreme Light: Entering New Frontiers with Petawatt-Class Lasers III*, volume 10241, page 102411K. International Society for Optics and Photonics (2017).

[109] F. Wagner, C. João, J. Fils, T. Gottschall, J. Hein, J. Körner, J. Limpert, M. Roth, T. Stöhlker, and V. Bagnoud. *Temporal contrast control at the PHELIX petawatt laser facility by means of tunable sub-picosecond optical parametric amplification*. Applied Physics B, 116(2):429–435 (2014).

[110] L. Ranc, C. Le Blanc, N. Lebas, L. Martin, J.-P. Zou, F. Mathieu, C. Radier, S. Ricaud, F. Druon, and D. Papadopoulos. *Improvement in the temporal contrast in the tens of ps range of the multi-PW Apollon laser front-end*. Optics Letters, 45(16):4599–4602 (2020).

[111] I. W. Choi, C. Jeon, S. G. Lee, S. Y. Kim, T. Y. Kim, I. J. Kim, H. W. Lee, J. W. Yoon, J. H. Sung, S. K. Lee, *et al. Highly efficient double plasma mirror producing ultrahigh-contrast multi-petawatt laser pulses*. Optics Letters, 45(23):6342–6345 (2020).

[112] C. M. Brenner, A. Robinson, K. Markey, R. Scott, R. Gray, M. Rosinski, O. Deppert, J. Badziak, D. Batani, J. Davies, *et al. High energy conversion efficiency in laser-proton acceleration by controlling laser-energy deposition onto thin foil targets*. Applied Physics Letters, 104(8):081123 (2014).

Paper I

Influence of micromachined targets on laser accelerated proton beam profiles

M. Dalui, A. Permogorov, H. Pahl, A. Persson, and C.-G. Wahlström
Plasma Physics and Controlled Fusion **60** 035014 (2018)

OPEN ACCESS
IOP Publishing
Plasma Physics and Controlled Fusion
Plasma Phys. Control. Fusion **60** (2018) 035014 (7pp)
https://doi.org/10.1088/1361-6587/aaa79f

Influence of micromachined targets on laser accelerated proton beam profiles

Malay Dalui, Alexander Permogorov, Hannes Pahl[1], Anders Persson and Claes-Göran Wahlström

Department of Physics, Lund University, PO Box 118, Lund, SE-221 00, Sweden

E-mail: malay.dalui@fysik.lth.se

Received 13 October 2017, revised 12 January 2018
Accepted for publication 15 January 2018
Published 6 February 2018

Abstract

High intensity laser-driven proton acceleration from micromachined targets is studied experimentally in the target-normal-sheath-acceleration regime. Conical pits are created on the front surface of flat aluminium foils of initial thickness 12.5 and 3 μm using series of low energy pulses (0.5–2.5 μJ). Proton acceleration from such micromachined targets is compared with flat foils of equivalent thickness at a laser intensity of 7×10^{19} W cm^{-2}. The maximum proton energy obtained from targets machined from 12.5 μm thick foils is found to be slightly lower than that of flat foils of equivalent remaining thickness, and the angular divergence of the proton beam is observed to increase as the depth of the pit approaches the foil thickness. Targets machined from 3 μm thick foils, on the other hand, show evidence of increasing the maximum proton energy when the depths of the structures are small. Furthermore, shallow pits on 3 μm thick foils are found to be efficient in reducing the proton beam divergence by a factor of up to three compared to that obtained from flat foils, while maintaining the maximum proton energy.

Keywords: laser-plasma based proton acceleration, laser micromachining, conical structures

(Some figures may appear in colour only in the online journal)

1. Introduction

Laser-plasma based proton acceleration has become a widely studied research area due to its capability of accelerating ions over a very short distance [1, 2]. Typically protons are accelerated over a distance of up to tens of μm by a high amplitude transient electric field ($\sim$TV m^{-1}) produced in the interaction of high intensity laser interaction with thin foils. Compared to conventional accelerator beams, shorter bunch duration, lower transverse emittance, and smaller source size make laser accelerated protons potentially suitable for numerous applications in fundamental as well as applied science and medicine [3]. Although, the potential is enormous for viable applications, low repetition rate, broad energy spectra and large ion-divergence of laser-driven ion sources need to be overwhelmed.

The most robust mechanism for laser-driven ion acceleration is called target normal sheath acceleration (TNSA) [4–6]. In this scheme, typically, a high intensity ($>10^{18}$ W cm^{-2}), short (<1 ps) laser pulse is focused onto the front surface of a thin foil (few μm thick). Very often the laser pulse pedestal, originating from amplified spontaneous emission (ASE), and the rising edge of the pulse almost completely ionize the material in the focal area, resulting in hot dense plasma. The rest of the pulse cannot propagate through this plasma and transfers a fraction of its energy to the plasma electrons before being reflected. Depending on laser intensity and plasma density gradient, several processes (e.g. resonance absorption, $\mathbf{J} \times \mathbf{B}$ heating, Brunel heating, etc) lead to a copious production of energetic (*hot*) electrons [7, 8]. A large number of these hot electrons then penetrate the foil and generate a strong charge-separation sheath electric field at the rear side of the target. Atoms, present at the rear side of the target, usually as surface contamination, get field ionized and subsequently accelerated in this transient sheath

[1] Present address: CERN, Geneva 23, CH-1211, Switzerland.

field to multi-MeV energies according to their charge-to-mass ratio. The strength of the sheath field is proportional to the square root of the product of the hot electron density and temperature. Therefore, higher and hotter electron production can lead to enhanced proton acceleration. The use of thin targets reduces the effective area of hot electron emission from the rear side of the target and thereby increases the areal density of hot electrons which gives rise to improved proton acceleration [9–11]. However, the ultimate target thickness is limited by the intensity contrast between the pedestal and the peak of the laser pulse. In addition, structured targets, where the material distribution at the front surface is modified, can be more efficient in absorbing the laser pulse energy than flat targets leading to both larger number and increased temperature of hot electrons [12–15], resulting in enhanced proton acceleration [16–20].

Typically TNSA proton beams have a large and energy dependent angular divergence with the smallest divergence for the most energetic protons [21–23]. Focussing of the full proton beam down to a small spot has been demonstrated in the past using curved targets [24, 25]. Recently, Aurand *et al* have demonstrated that the spatial distribution of the hot electrons on the rear side of the target and the transverse expansion of the electric sheath field has a profound effect on the angular divergence of the accelerated protons; the proton beam divergence can be reduced if the transverse spatial distribution of the electron sheath on the rear surface of the target is increased [26]. One way to reduce it is to defocus the laser on the target [26]. The maximum proton energy in this case is found to be lower, as the laser intensity on the target becomes lower compared to the tight focus condition. In spite of obtaining enhanced hot electron production, Matsuoka *et al* have reported almost similar acceleration in terms of maximum proton energy from conical targets compared to flat targets [27]. The conical structures were created on the front surface of the thin foils of various initial thickness, in the range 25–100 μm using series of pulses of energy 7–70 μJ. The higher number of hot electrons produced in such interactions is argued to be balanced by a larger electron divergence which acts adversely to enhance the maximum proton energy. In the present study we extend that investigation with thinner target foils (3 and 12.5 μm) and also using lower energy pulses (0.5–2.5 μJ) for making structures. The questions we address here are, whether higher electron divergence produced in conical targets is effective in reducing the proton beam divergence, and if there are any effects of different aspect ratios (longitudinal versus radial dimension) of the conical structures on the proton acceleration.

To prepare our structured targets, we use laser micromachining on thin aluminium foils. Laser micromachining is the process in which micron sized features/structures are created by ablating material from a substrate using pulsed lasers. With femtosecond duration and low pulse energy, the laser energy is deposited very rapidly and the thermal diffusion to the ionic lattice is minimized, which results in sharp and reproducible structures [28]. This method has the advantage that it facilitates *in situ* target fabrication as the same beam and focusing geometry can be used for target preparation as well as proton acceleration without altering the experimental set-up. Laser micromachining is also very effective in generating controlled transient plasma structures on a plain solid surface, which can be used to study laser energy absorption, electron dynamics as well as proton acceleration from such structures [29–31]. In our experiment the pulse energy is adequately attenuated while micromachining such that only a very small amount of target material is removed from the focal area with each laser pulse, resulting in a pit on the front surface of the target. The depth of the pit is controlled by the number of machining pulses. Since the propagation axis for the machining pulse and the main pulse is identical, this method also relaxes the requirement of target alignment between target machining and proton acceleration. We found that micromachined targets, for a certain geometrical structure of the pit, can be effective in reducing the proton beam divergence by a factor of up to three compared to conventional flat targets.

2. Experimental set-up

The experiments are performed using the 10 Hz multi-terawatt Ti:sapphire laser system at Lund University, Sweden. It is a chirped pulse amplification based system delivering linearly polarized laser pulses of 35 fs temporal duration at a central wavelength of 800 nm. In the present experiments, the main pulse (accelerating pulse) energy on the target is kept fixed at 0.59($\pm$0.05) J. The ASE to main pulse intensity contrast of the laser pulses, as measured by a third order autocorrelator, is 1–3 $\times$ 10^{-9} up to 50 ps prior to the arrival of the peak of the pulse. After compression, a deformable mirror (DM) sends the laser beam to the experimental chamber. Figure 1 shows the schematics of the experimental setup. The p-polarized laser pulses are focused on the target by a $f/3$ off-axis parabolic mirror at an incidence angle of 45°. The DM, together with a wavefront sensor, corrects for wavefront aberrations and helps to achieve a circular focal spot of approximately 3.7 μm full-width-at-half-maximum (FWHM) in diameter, resulting in a peak intensity of 7 $\times$ 10^{19} W cm^{-2} in vacuum. The target foil is sandwiched between two rectangular metal frames, each having an identical array of circular openings (sites) that enables to have free standing target foils on every site. The whole target holder is mounted on a motorized x–y–z translation stage assembly allowing a new target foil to be positioned in the focal plane for each laser shot. A magnetic spectrometer, placed in the target normal direction on the rear side of the target, is used to record the proton energy spectra on a shot-to-shot basis. This spectrometer, which is based on a permanent dipole magnet, bends the proton trajectories downwards (y-direction) according to their energy. A rectangular slit is used at the entry of the spectrometer to sample the central part of the proton beam. After the magnet the protons impact on a plastic scintillator (Saint-Gobain, BC-408) and the resulting fluorescence is imaged onto a 16-bit EMCCD camera. The spatial profile of the proton beam is imaged by another scintillating screen (5 cm $\times$ 8 cm) placed within a light shielded box (footprint

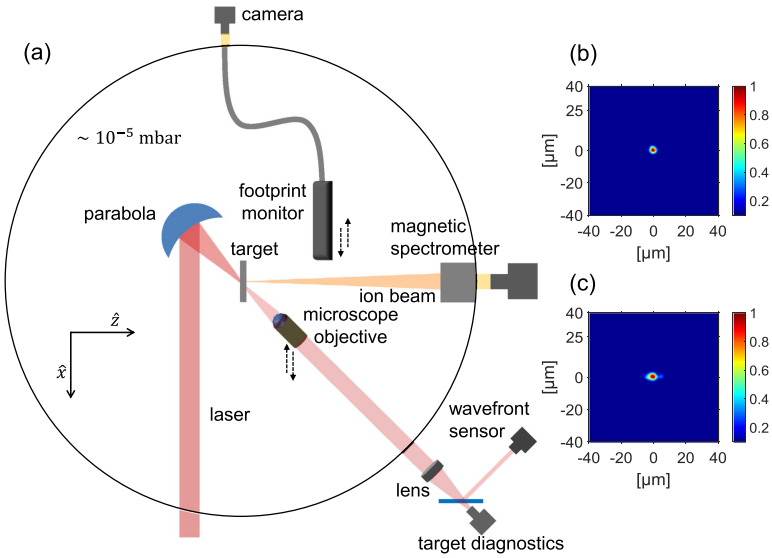

Figure 1. (a) Schematics of the experimental set-up (top view). The laser pulse is focused on the front side of the target by an off-axis parabola. The microscope objective is used to align the target in the focus. The magnetic spectrometer and the footprint monitor are used to characterize the proton beam. Images of the focus of the accelerating pulse and the machining pulse in vacuum are shown in (b) and (c), respectively.

monitor) at a distance of 8.3 cm from the rear surface of the target. The footprint monitor is mounted on a linear translational stage that allows it to be moved in and out of the proton beam path. It is positioned in a way that it can capture proton beams of transverse size up to approximately 32° (full-angle). For a single laser shot either the spectrum or the spatial profile of the proton beam is recorded. Both scintillators are covered with a single layer of 13 μm thick Al foil to protect them from ambient light (radiation from resultant plasma as well as scattered laser radiation) and target debris. It also stops protons of energy less than 0.9 MeV and heavier ions compared to proton from reaching the detector. The whole experimental chamber is maintained at a pressure $\sim 10^{-5}$ mbar. More details about the target system and ion diagnostics can be found in [32].

3. Target preparation

We use Al foils of two different initial thicknesses (12.5 and 3 μm) and the front side of each foil is laser machined to create conical pits. The laser pulse energy is selected by ensuring through a microscope objective that no surface deformation occurs on the rear surface of the foils. Approximately 2.5 μJ/pulse and 0.5 μJ/pulse are used respectively to machine the thicker foil and the thinner foil. Figure 2(a) shows the schematic of the micromachined targets. The impact of a large number of machining pulses eventually forms a tunnel through the foil. The transmission of a co-linear HeNe laser beam is used to confirm the tunnel making process. If N_t is the minimum number of machining pulses required to make a tunnel through a foil of thickness L, then, the material removal rate is estimated as L/N_t. Therefore, the depth of the pit after N ($<N_t$) machining pulses is estimated to be, $d = NL/N_t$; and the remaining foil thickness, $l_{\text{rem}}^{N} = L - d = L(1 - N/N_t)$. Figure 2(b) shows an microscope image of the front side of the foil after machining a 12.5 μm foil with 25 pulses. The pit is slightly elliptical in shape as the laser pulse is incident obliquely onto the target. The width of the pit as a function of N is shown in figure 2(c), and it is observed to remain below four times the diameter (FWHM) of the laser focal spot in vacuum.

4. Results and discussions

In the experiment, we first fix the initial foil thickness and send low energy machining pulses to create a pit on the front side of the foil. The full energy pulse is sent after micromachining, and proton energy spectra as well as proton beam profiles are recorded as a function of number of machining pulses (N). After each such measurement, we move to a new undamaged target site for the next measurement, and the whole process is repeated during the experiment. Results obtained from machined targets of different l_{rem} are compared with flat foils of equivalent thickness under similar experimental conditions.

Prior to the experiment the laser focus is optimized in spatial domain using adaptive optics and in temporal domain by adjusting the compressor-grating to minimize any spatio-temporal coupling. The image of the focus of the accelerating pulse as well as the machining pulse are shown in figures 1(b) and (c), respectively. Other method of characterization can be

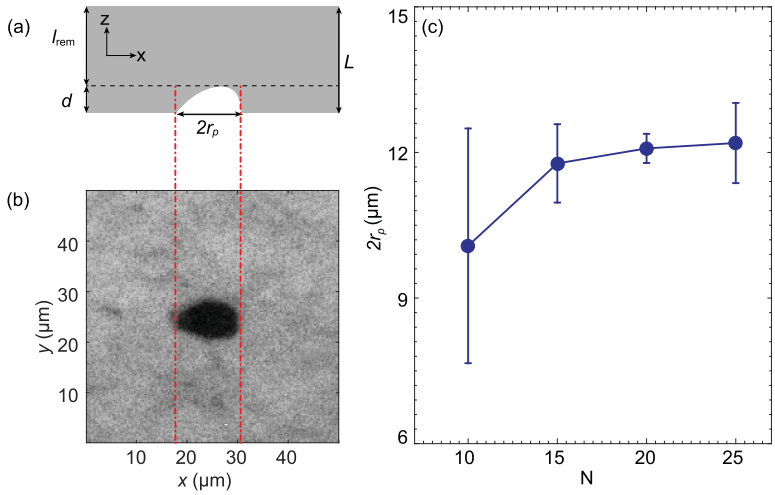

Figure 2. (a) Schematic showing the side-view (in x–z plane) of the micromachined target, (b) is a microscope image of the front-side of the micromachined target surface (top-view), and (c) shows the size (long axis) of the conical structure as a function of the number of machining pulses.

found in [33]. We believe that 'prethermal' laser ion sheath acceleration [34] is absent in our experimental conditions. The Rayleigh length of the laser focus is much longer than the depth of the pits as well as the target thickness; therefore, the change in the main pulse intensity is negligible when it interacts with the micromachined targets.

4.1. Structures on 12.5 μm thick foils

Proton energy spectra (averaged over 5 shots), as derived from the magnetic spectrometer, from flat foils of different thickness and from laser machined targets with different l_{rem} are shown in figures 3(a) and (b), respectively. For flat targets, the maximum proton energy, E^{p}_{max} is observed to increase with decreasing foil thickness, which is consistent with the results of several previous experimental studies [9–11]. For micromachined targets, irrespective of l_{rem}, E^{p}_{max} remains almost constant and equal to that obtained with 12.5 μm thick flat foils. This indicates that the ion front experiences almost equal accelerating sheath fields for the case of machined targets along the target normal direction. Figure 4 shows the spatial profile of the proton beam as detected by the footprint monitor from flat targets (figures 4(a)–(c)) as well as micromachined targets (figures 4(d)–(f)). We observe that the angular divergence of the proton beam from micromachined targets are comparable with that obtained from flat foils as long as $l_{rem} \gtrsim 6$ μm. In this case the full-angle-at-half-maximum (FAHM) of the proton beam is found to be 6.1°(±0.6°). The beam divergence increases to 9°(±1°) (FAHM) when l_{rem} is reduced to 3 μm. The proton emission seems to lose beam-like properties and its spatial profile becomes larger than the footprint monitor detector window as l_{rem} becomes very small as the conical

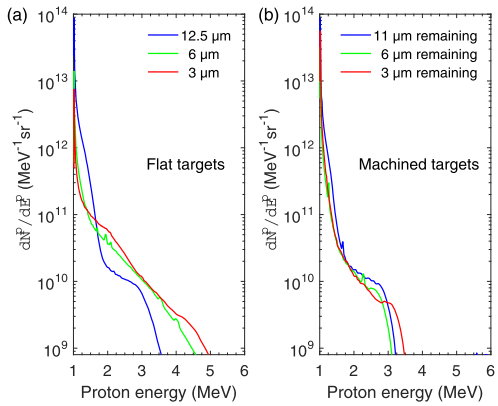

Figure 3. Proton energy spectra from (a) flat foils of different thickness and (b) micromachined targets (from 12.5 μm foil) of various l_{rem} as retrieved from the magnetic spectrometer.

structure starts acting as a diverging element/lens for the hot electrons.

The results can be explained considering ballistic propagation of hot electrons through the target. The hot electrons leave the rear surface of the target from an effective area, $w_{eh} = \frac{\pi}{4}D^2$, where, $D = s_{eh} + 2l_{rem}\tan\alpha_{eh}$ is the diameter of the area of hot electron emission from the rear side of the target, s_{eh} is the diameter of the laser interaction area on the front side and α_{eh} is the half-divergence-angle of the hot electron beam [35]. For flat foils, E^{p}_{max} increases with decreasing foil thickness due to geometric effects as the hot electron density on the rear surface increases as $n_{eh} \propto 1/w_{eh}$

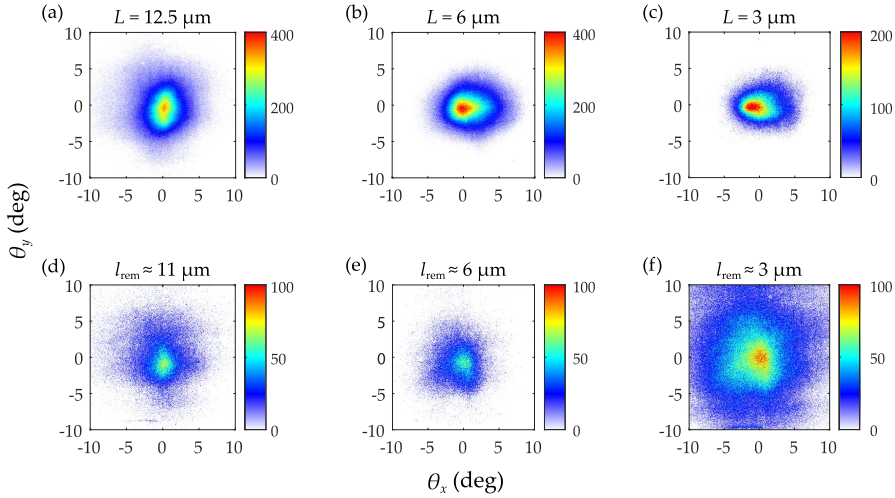

Figure 4. (a)–(c) Show spatial profiles of proton beam obtained from flat foils of different thickness, L (top panel). Beam profiles acquired from micromachined targets of different l_{rem} are shown in (d)–(f) (bottom panel). L and l_{rem} for different targets are labelled accordingly.

Table 1. The diameter of the hot electron sheath on the rear side of the target (D) as calculated using a simple model considering ballistic propagation of hot electrons for targets machined from an initial thickness of 12.5 μm.

Targets	s_{eh} (μm)	l_{rem} (μm)	α_{eh} (°)	D (μm)
Flat foil (L = 12.5 μm)	3.7	12.5	40	24.7
Machined (shallow pits)	3.7	11	40	22.2
Machined (moderate pits)	3.7	6	50	18
Machined (deep pits)	3.7	3	50	10.9

[9, 10]. In machined targets, the hot electrons originate not only from the tip of the conical structure but from a larger area around the tip including the wall surface, resulting in a higher hot electron production with a larger angular divergence [27]. Higher α_{eh} acts adversely to increase n_{eh}, resulting in similar (slightly lower) maximum proton energy from micromachined targets compared to flat targets of equivalent thickness. These observations are consistent with earlier works of Matsuoka *et al* [27]. Previous studies have shown that the transverse spatial profile of the sheath field on the target-rear surface has a profound influence on the angular divergence of the accelerated proton beam. Using numerical simulations it has been shown that the diameter of the resultant proton beam at the detector can be reduced, if the transverse circular area of the sheath field on the rear side of the target is increased [26]. With micromachined targets, the laser interaction not only increases α_{eh}, but also decreases l_{rem} as the depth of the pit increases. However, if the product remains at a constant value, the proton beam divergence should not change, which can explain the beam profile obtained from micromachined targets for $l_{rem} \gtrsim 6$ μm. For deeper pits ($l_{rem} \lesssim 3$ μm), the hot electrons need to travel less distance to reach the rear side of the foil; therefore, the effective area of hot electron emission (w_{eh}) is reduced, resulting in more divergent proton beams. Table 1 shows the diameter of the hot electron sheath on the rear side of the target, D as calculated using our model. We assume that the half-divergence angle of the hot electron emission does not change due to shallow pits. The values for electron divergence for deeper pits are taken from [27]. It can be seen that D remains almost similar for shallow pits and the proton beam divergence does not show much change. For deep pits ($l_{rem} \lesssim 3$ μm), D decreases significantly, that results in divergent proton beams.

4.2. Structures on 3 μm thick foils

The results of proton acceleration from targets machined from 3 μm thick Al foils are shown in figure 5. The proton energy spectra (averaged over 5 shots) from flat targets and micromachined targets are shown in figure 5(a) for various pit depths (d) of the conical structure. Although E^{p}_{max} shows a slight increase for shallow pits ($d \sim 0.2$ μm), this method does not seem to boost the proton acceleration significantly along the target normal direction (black triangles in figure 5(b)). However, for shallow pits ($d = 0.1$–0.5 μm), the angular divergence of the proton beam is observed to be reduced by a factor of about 3 compared to flat foils (red circles in figure 5(b)). The error bars here represent the standard deviation of the data set as obtained from three

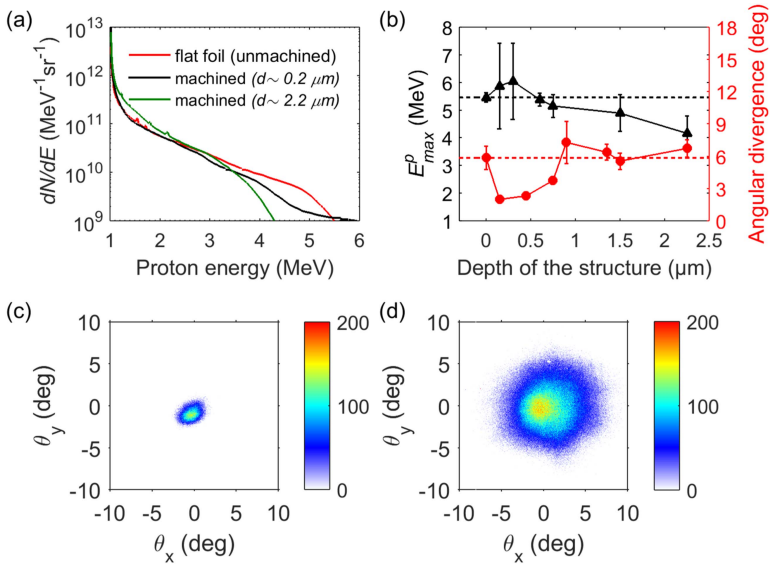

Figure 5. (a) Average proton energy spectra as obtained from flat foils (3 μm thick) and machined (from 3 μm thick foils) targets of different pit depth. (b) Maximum proton energy (E^{p}_{max}) as derived from the spectrometer (black triangles) and angular divergence (FAHM) of the proton beams as detected in the footprint monitor (red circles) for different pit depth, d. The dotted lines correspond to the reference for flat targets ($d = 0$). (c) Shows the beam profile obtained from micromachined target when the pit depth, $d \approx 0.15$ μm and (d) is a representative spatial profile of the proton beam from reference flat targets (3 μm thick).

Table 2. The diameter of the hot electron sheath on the rear side of the target (D) as calculated using the simple model presented in section 4.1 for targets machined from an initial thickness of 3 μm.

Targets	s_{eh} (μm)	l_{rem} (μm)	α_{eh} (°)	D (μm)
Flat ($L = 3$ μm)	3.7	3	40	8.7
Machined (shallow pits)	3.7	2.8	40	8.4
Machined (deep pits)	3.7	0.8	50	5.6

different targets and laser shots. The spatial profile of one such proton beam is shown in figure 5(c) measuring a beam divergence of only 2° (±0.3°) (FAHM), whereas the divergence is 5.9°(±1.1°) (FAHM) for 3 μm thick flat foils (figure 5(d)). Targets machined from thicker foils (12.5 μm) having similar pit depths are not very productive in reducing the beam divergence, indicating that a particular aspect ratio of the conical structure is needed for this effect. Deeper pits ($d > 2$ μm) machined in the 3 μm foils make the proton beam divergent, similar to the behaviour exhibited by machined targets from thicker foils. Table 2 shows the values of the extension of the sheath field, D as calculated using our model for different target parameters. For deep pits, D decreases slightly compared to that obtained with flat foils, which results in a small change in the proton beam divergence (see figure 5(b)). For shallow pits on 3 μm foils, D can increase by a factor of three compared to flat foils if $\alpha_{eh} > 75°$, which can results in a three fold reduction in proton beam divergence. However, the hot electron divergence as measured in [27] is well below this estimated value. Moreover, we have observed in section 4.1 that the results can be explained if α_{eh} remains same to that of flat foils for shallow pits. Further investigations are needed to understand the effect of reduction of proton beam divergence as the hot electron recirculation may play an important role in shaping the transverse distribution of the sheath field for such target geometries.

To investigate the qualitative energy distribution of protons within the beam, we have used a stack made up with five layers of CR-39 (25 mm × 25 mm× 100 μm) plastic sheet. Energetic protons when is passed through CR-39, permanent tracks are formed and is used to detect protons. Proton deposits most of its energy at the Bragg peak; hence a stack of CR-39 provides energy resolved spatial profiles of the beam. The stack is placed on the rear side of the target foil, approximately 2 cm away from the target surface and is covered with a 13 μm thick Al-foil for shielding. For flat targets, protons are found to be distributed symmetrically where the most energetic protons are located at the central region around the target normal, which is consistent with several experimental studies. However, the distribution is skewed for machined targets and the most energetic protons are found to be shifted from the target normal towards the laser direction by about 20°. The findings are consistent with earlier works of Matsuoka *et al* [27]. The effect could be because of the combination of the denting of the target due to the $\mathbf{J} \times \mathbf{B}$ force [36, 37] and the geometry of the conical structure.

5. Conclusion

We have carried out experimental investigations on proton acceleration from laser-machined structured targets. In order to exploit the inherent advantage of self-alignment of the target, the same focusing geometry is used for machining the target as well as for the accelerating laser pulse. Conical pits of different aspect ratios are micromachined at the front side of Al foils of initial thicknesses 12.5 and 3 μm. Even for the deepest pits, in the thicker foil, the width of the structure at the front surface is found to be within four times the diameter (FWHM) of the laser focal spot in vacuum. Proton acceleration results from micromachined targets of various remaining thicknesses are compared with flat targets of equivalent thickness. Micromachined targets from an initial thickness of 12.5 μm do not result in improved proton acceleration in terms of maximum energy compared to flat Al foils of equivalent thickness. Furthermore, the spatial profiles of the proton beams are observed to be similar to that obtained from flat foils for $l_{\rm rem} \gtrsim L/2$, but the beam becomes very divergent for $l_{\rm rem} < L/2$, which is attributed to the narrower transverse spatial distribution of the hot electrons on the rear-surface. On the other hand, shallow pits on the front side of a 3 μm thick Al foil are found to be effective in reducing the angular divergence of the proton beam by a factor of three, without affecting the maximum proton energy. In addition, a slight increase in the maximum proton energy is observed for these targets compared to unstructured flat foils. Targets machined from thicker foils with similar $l_{\rm rem}$ ($>L/2$) do not result in such a reduction in proton beam divergence, indicating that the aspect ratio of the conical structure, $d/2r_p$ (see figure 2(a)) also has a bearing on the angular divergence of the accelerated proton beam. A certain geometry of the pit structure ($l_{\rm rem} \gtrsim L/2$ and $d/2r_p \sim 0.1$) on 3 μm foils is found to be effective in improving the proton beam quality.

Acknowledgments

The authors acknowledge the support of the Swedish Research Council and the Knut and Alice Wallenberg Foundation, including their funding of the PLIONA project.

ORCID iDs

Malay Dalui https://orcid.org/0000-0003-1313-430X
Hannes Pahl https://orcid.org/0000-0003-0498-1339

References

[1] Daido H, Nishiuchi M and Pirozkov A S 2012 *Rep. Prog. Phys.* **75** 056401
[2] Macchi A, Borghesi M and Passoni M 2013 *Rev. Mod. Phys.* **85** 751
[3] Malka V, Faure J, Gauduel Y A, Lefebvre E, Rousse A and Phuoc K T 2008 *Nat. Phys.* **4** 447
[4] Wilks S C, Langdon A B, Cowan T E, Roth M, Singh M, Hatchett S, Key M H, Pennington D, MacKinnon A and Snavely R A 2001 *Phys. Plasmas* **8** 542
[5] Passoni M, Perego C, Sagattoni A and Batani D 2013 *Phys. Plasmas* **20** 060701
[6] Roth M and Schollmeier M 2016 *CERN Yellow Rep.* **1** 231
[7] Liseykina T, Mulser P and Murakami M 2015 *Phys. Plasmas* **22** 033302
[8] Sheng Z M, Weng S M, Yu L L, Wang W M, Cui Y Q, Chen M and Zhang J 2015 *Chin. Phys.* B **24** 015201
[9] Kaluza M, Schreiber J, Santala M I K, Tsakiris G D, Eidmann K, Meyer-ter-Vehn J and Witte K J 2004 *Phys. Rev. Lett.* **93** 045003
[10] Neely D, Foster P, Robinson A, Lindau F, Lundh O, Persson A, Wahlström C-G and McKenna P 2006 *Appl. Phys. Lett.* **89** 021502
[11] Zeil K, Kraft S D, Bock S, Bussmann M, Cowan T E, Kluge T, Metzkes J, Richter T, Sauerbrey R and Schramm U 2010 *New J. Phys.* **12** 045015
[12] Kahaly S, Yadav S K, Wang W-M, Sengupta S, Sheng Z-M, Das A, Kaw P K and Kumar G R 2008 *Phys. Rev. Lett.* **101** 145001
[13] Klimo O, Psikal J, Limpouch J, Proska J, Novotny F, Ceccotti T, Floquet V and Kawata S 2011 *New J. Phys.* **13** 053028
[14] Cristoforetti G *et al* 2014 *Plasma Phys. Control. Fusion* **56** 095001
[15] Dalui M, Kundu M, Trivikram T M, Ray K and Krishnamurthy M 2016 *Phys. Plasmas* **23** 103101
[16] Margarone D *et al* 2012 *Phys. Rev. Lett.* **109** 234801
[17] Ceccotti T *et al* 2013 *Phys. Rev. Lett.* **111** 185001
[18] Prencipe I *et al* 2016 *Plasma Phys. Control. Fusion* **58** 034019
[19] Passoni M *et al* 2016 *Phys. Rev. Accel. Beams* **19** 061301
[20] Dalui M, Kundu M, Tata S, Lad A D, Jha J, Ray K and Krishnamurthy M 2017 *AIP Adv.* **7** 095018
[21] Maksimchuk A, Gu S, Flippo K, Umstadter D and Bychenkov V Y 2000 *Phys. Rev. Lett.* **84** 4108
[22] Snavely R A *et al* 2000 *Phys. Rev. Lett.* **85** 2945
[23] Borghesi M, Mackinnon A J, Campbel D H, Hicks D G, Kar S, Patel P K, Price D, Romagnani L, Schiavi A and Willi O 2004 *Phys. Rev. Lett.* **92** 055003
[24] Patel P K, Mackinnon A J, Key M H, Cowan T E, Foord M E, Allen M, Price D F, Ruhl H, Springer P T and Stephens R 2003 *Phys. Rev. Lett.* **91** 125004
[25] Snavely R A *et al* 2007 *Phys. Plasmas* **14** 092703
[26] Aurand B *et al* 2016 *Phys. Plasmas* **23** 023113
[27] Matsuoka T *et al* 2010 *Nucl. Fusion* **50** 055006
[28] Pronko P P, Dutta S K, Squier J, Rudd J V, Du D and Mourou G 1995 *Opt. Commun.* **114** 106
[29] Monchocé S, Kahaly S, Leblanc A, Videau L, Combis P, Réau F, Garzella D, D'Oliveira P, Martin P and Quéré F 2014 *Phys. Rev. Lett.* **112** 145008
[30] Leblanc A, Monchocé S, Bourassin-Bouchet C, Kahaly S, Quéré F and Faure J 2016 *Nat. Phys.* **12** 301
[31] Lübcke A, Andreev A, Höhm S, Grunwald R, Ehrentraut L and Schnürer M 2017 *Sci. Rep.* **7** 44030
[32] Aurand B, Hansson M, Senje L, Svensson K, Persson A, Neely D, Lundh O and Wahlström C-G 2015 *Laser Part. Beams* **33** 59
[33] Kahaly S, Monchocé S, Gallet V, Gobert O, Réau F, Tcherbakoff O, D'Oliveira P, Martin P and Quéré F 2014 *Appl. Phys. Lett.* **104** 054103
[34] Zeil K, Metzkes J, Kluge T, Bussmann M, Cowan T E, Kraft S D, Sauerbrey R and Schramm U 2014 *Nat. Commun.* **3** 874
[35] Coury M *et al* 2012 *Appl. Phys. Lett.* **100** 074105
[36] Vincenti H, Monchocé S, Kahaly S, Bonnaud G, Martin P and Quéré F 2014 *Nat. Commun.* **5** 3403
[37] Thévenet M, Leblanc A, Kahaly S, Vincenti H, Vernier A, Quéré F and Faure J 2016 *Nat. Phys.* **12** 355

Paper II

Enhanced laser-driven proton acceleration using nanowire targets

S. Vallières, M. Salvadori, A. Permogorov, G. Cantono, K. Svendsen, Z. Chen, S. Sun, F. Consoli, E. d'Humières, C.-G. Wahlström and P. Antici
Scientific Reports 11:2226 (2021)

scientific reports

OPEN

Enhanced laser-driven proton acceleration using nanowire targets

S. Vallières[1,2]✉, M. Salvadori[1,3,4], A. Permogorov[5], G. Cantono[5], K. Svendsen[5], Z. Chen[1], S. Sun[1], F. Consoli[3], E. d'Humières[2], C.-G. Wahlström[5] & P. Antici[1]

Laser-driven proton acceleration is a growing field of interest in the high-power laser community. One of the big challenges related to the most routinely used laser-driven ion acceleration mechanism, Target-Normal Sheath Acceleration (TNSA), is to enhance the laser-to-proton energy transfer such as to maximize the proton kinetic energy and number. A way to achieve this is using nanostructured target surfaces in the laser-matter interaction. In this paper, we show that nanowire structures can increase the maximum proton energy by a factor of two, triple the proton temperature and boost the proton numbers, in a campaign performed on the ultra-high contrast 10 TW laser at the Lund Laser Center (LLC). The optimal nanowire length, generating maximum proton energies around 6 MeV, is around 1–2 μm. This nanowire length is sufficient to form well-defined highly-absorptive NW forests and short enough to minimize the energy loss of hot electrons going through the target bulk. Results are further supported by Particle-In-Cell simulations. Systematically analyzing nanowire length, diameter and gap size, we examine the underlying physical mechanisms that are provoking the enhancement of the longitudinal accelerating electric field. The parameter scan analysis shows that optimizing the spatial gap between the nanowires leads to larger enhancement than by the nanowire diameter and length, through increased electron heating.

Laser-driven ion acceleration, as obtained by interaction of a high-intensity short-pulse laser with a target, is a recent field of interest for its many diverse potential applications[1–3]. Besides being a compact source, laser-accelerated protons feature a high brillance, a short bunch duration and a large energy spread. This has catalyzed their utilization in different domains that include ultra-fast radiography[4], novel fusion schemes[5], high energy density matter[6], laboratory astrophysics[7], medical applications[8–10], novel neutron sources[11], cultural heritage[12,13], material science[14–16] and using them as injectors for larger accelerators[17,18]. Most of these applications have been currently explored with the most consolidated acceleration mechanism that is obtained on typical commercially available TW laser systems, the so-called Target-Normal Sheath Acceleration (TNSA)[19]. In this acceleration scheme, hydrogen containing contaminants are accelerated at the rear surface of a thin solid foil (target), typically made of gold (Au), aluminum (Al) or copper (Cu), that is irradiated by a high-intensity ($I_0 > 10^{18}$ W/cm^2), short pulse (< 1 ps) laser operating in the near-infrared spectral range. Since about two decades, scientists are trying to find ways to increase the proton energy and proton flux, such as to expand the portfolio of viable applications. Besides increasing the laser energy, which results in high proton energies[20], the most straightforward method to do so is by improving the laser energy absorption on the target, a key parameter to transferring energy into the accelerated ions.

In the past, there have been many suggestions on how to improve the target in order to maximize the laser-to-target absorption. Since one of the current trends for utilizing these sources for applications is by increasing the particle flux (for example, by increasing the shot rate), any new target proposal needs to result viable in terms of being easy and cheap to manufacture, and fast and non-stringent to align. Similar to photovoltaic applications, trapping light using micro- and nano-structured surfaces is one of the most established approaches to enhance the laser energy absorption[21–23]. In laser-driven ion acceleration, many studies have proposed nanostructuring the front target surface for this purpose, demonstrating both theoretically[24–31], and experimentally[32–42], an improvement in the absorption mechanisms. The drawback of such structures is that any trapping is limited to a nanometric scale in all three dimensions, which might not be always ideal. Nanometric rods standing up-right on a substrate in a brush-like geometry, also called nanowire (NW) targets, have recently been suggested for TNSA: These targets have the advantage of combining micrometric trapping thickness with nanometric structures.

[1]INRS-EMT, 1650 blvd. Lionel-Boulet, Varennes, QC J3X 1P7, Canada. [2]CELIA, Univ. of Bordeaux, 351 Cours de la Libération, 33400 Talence, France. [3]National Agency for New Technologies, Energy and Sustainable Economic Development, Via Enrico Fermi 45, 00044 Frascati, Rome, Italy. [4]Univ. of Rome "La Sapienza", P. Aldo Moro 5, 00185 Rome, Italy. [5]Department of Physics, Lund University, 22100 Lund, Sweden. ✉email: simon.vallieres@emt.inrs.ca

First theoretical and numerical estimations made by Wang et al.[43] have shown that this target type allows for an enhanced laser energy absorption. The same nanowire geometry has been demonstrated experimentally to be very effective for enhanced THz pulse generation[44], and several other works have demonstrated enhanced X-ray emission though greater electron heating with nano-velvets[45] and nanowires[46–48]. The high aspect ratio between length and diameter of NWs favors an increased laser absorption due to a greater effective interaction surface area with the incoming electromagnetic (EM) wave, occurring within a few laser cycles such as to maximize the interaction with the intact NW forest. This increased interaction ejects electrons from the NW boundaries mainly through Brunel-type and $\boldsymbol{J} \times \boldsymbol{B}$ absorption processes, which are further accelerated in the gaps between the NWs by Direct Laser Acceleration (DLA) before re-collision with the target bulk[49], where the electrons seed a cascade of impact ionization events. This leads to a denser and hotter electron cloud at the rear side of the target and generates a more intense accelerating sheath electric field driving the TNSA mechanism. Only two experimental studies have been performed to demonstrate this effect: Firstly, Khaghani et al.[50] irradiated micro-pillar targets with a 80 J and 500 fs laser. They obtained a maximum energy enhancement ratio of up to 2.4 and 20 times more protons in the spectrum. They show a measured hot electron temperature increase by a factor of 2 at lower laser intensity. Secondly, Dozières et al.[51] used NW targets and obtained a maximum energy enhancement factor in the range 1.5–2. In the same work, an experimental evaluation of the influence of d and g was performed, recommending a thorough evaluation of influence of length l in a subsequent study. In both works, a direct comparison between nanowires and flat targets having the same thickness within a systematic approach is missing, preventing conclusions to be drawn.

In this work we present a systematic study of enhanced laser-driven proton acceleration using Cu nanowire targets with regards to the geometrical parameters (diameter, gap and length). Our findings are supported and complemented numerically by Particle-In-Cell (PIC) simulations, which enabled a full parametric investigation. The effect of the NW's geometrical parameters are related to theoretical models for plasma expansion in vacuum[52]. The experimental study is complementary to Dozières et al.[51] and focuses on the NW length l as the main investigated parameter. Using experimental NW targets, we find average proton enhancement ratios of 2 and 3 for maximum energy and temperature respectively, as well as multiple-fold proton number enhancement. We relate these improvements to an enhanced TNSA-related electric field produced by a stronger hot electron yield, both in density n_e and temperature T_e. We find that the number of hot electrons generated by the interaction is dominantly influenced by the nanowire diameter, whereas a larger gap opening boosts the electron temperature up to a particular optimized gap size value. Between both parameters, the gap size has stronger influence compared to the nanowire diameter with regards to the laser energy absorption.

NW geometry optimization

We performed PIC simulations using the 2D3V PICLS code[53] to determine the optimal NW geometry for proton acceleration and thus to orient the NW production process. The 2D PIC simulations allow to investigate the role of NW length and check the optimal parameter range for the specific experimental configuration used in this work. In addition, the extensive parametric investigation considering all three parameter (d, g and l) allows a more comprehensive understanding of how the increased absorption and electron generation result in enhanced proton acceleration. Details about the simulation parameters can be found in *Methods*. The simulation geometry is shown in Fig. 1a. We performed different parametric simulations to optimize the diameter d, gap g and length l of the NWs, starting from the best case scenario depicted by Wang et al.[43] (i.e. $d = 200$ nm, $g = 200$ nm and $l = 1\,\mu$m at central laser wavelength of $\lambda_0 = 800$ nm) which we define as the nominal parameters. We varied each parameter independently, keeping the other parameters fixed. We can note in Fig. 1b where we present a snapshot of the simulation using the nominal parameters, a laser energy absorption of 75% compared to about 5% for a typical flat Cu foil, as is also shown in Fig. 1c–e for the best laser absorption cases (blue markers). Figure 1c shows that the laser energy absorption and laser-to-proton conversion efficiency peak for NW diameters of $d = 200$ nm ($\lambda_0/4$). Laser absorption and conversion efficiency both increase for $d < 100$ nm, as consistent with the work of Martinez et al.[54], and then decrease after $d = 200$ nm. This can be justified as follows: for small NW diameters $d < 100$ nm, increasing d leads to higher laser energy absorption through a greater number of electrons interacting with the laser pulse, whereas for values larger than $d = 200$ nm the area irradiated by the laser is closer to a flat surface as it reflects more energy from the NW tip surface. Figure 1d shows the variation of absorption with gap distance g, the laser energy absorption is already near-maximal at $g = 200$ nm ($\lambda_0/4$)[43], whereas the proton conversion efficiency optimum is found at $g = 800$ nm (λ_0). Interestingly, the laser absorption increases only slightly between 200 and 800 nm, while the laser-to-proton conversion efficiency increases significantly (almost doubles, passing from 10 to 18%). This difference among the two absorption mechanisms is due to the ejected electrons that are accelerated within the laser field in the gap region before re-collision with the target bulk: For too small gaps, the electrons reach the next NW with lower kinetic energy (electronic temperature) than for larger gaps. Therefore, larger gaps lead to a greater energy transfer to the protons, a phenomenon also observed and explained in the work of Blanco et al.[27] using triangular nanostructures and found also in other works[42,54,56,57]. Concerning the NW length variation exposed in Fig. 1e, we see that the laser energy absorption (blue diamonds) improves very strongly from $l = 0\,\mu$m (flat target substrate of thickness $s = 300$ nm) to $l = 0.5\,\mu$m, whereas for $l > 0.5\,\mu$m it only increases by less than 1%. Concerning the laser-to-proton conversion efficiency (red dots), it is best for the shortest NWs and decreases for longer NW lengths. This is similar to what is observed in the TNSA regime when increasing the thickness of flat targets[55]. More precisely, electrons ejected from longer NWs will go through a larger effective material thickness and thus lose more energy (i.e. lower electron temperature) before reaching the rear target surface where they establish the accelerating sheath electric field. Hence, even if longer NWs lead to a greater laser energy absorption and therefore to greater number of ejected electrons, using long lengths also increases the energy loss of electrons during their re-collision with

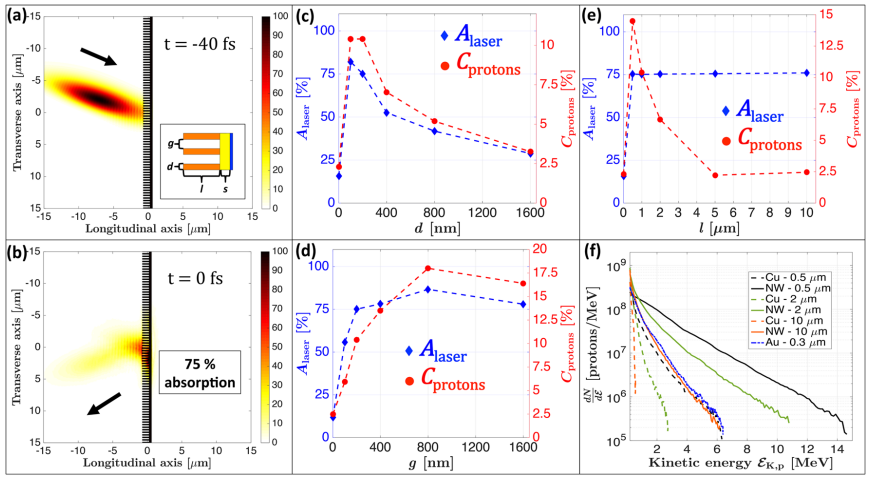

Figure 1. Numerical optimization of NW geometry through PIC simulations using the 2D3V PICLS code. (**a**) EM intensity and simulated target shown just before the laser interaction at $t = -40$ fs. Color scale is in percentage of maximum intensity. The inset is a NW scheme defining the geometry parameters l, d and g; target is composed of copper NW (orange), gold substrate (yellow) and a proton layer (blue). (**b**) EM intensity and simulated target shown during the laser-target interaction at $t = 0$ fs. (**c**–**e**) Variation of laser energy absorption (blue diamonds—left scale) and laser-to-proton conversion efficiency (red points—right scale) for different NW (**c**) diameters d, (**d**) gaps g and (**e**) lengths l. (**f**) Simulated proton spectra for NWs with $d = g = 200$ nm (same values as the experimental working point) and three different NW lengths of 0.5, 2 and 10 μm (solid lines), along with their thickness-equivalent Cu reference foils and the bare Au substrate of 0.3 μm (dotted lines).

the target (wires and substrate), which ultimately produces lower laser-to-proton conversion efficiency. This effect is exhibited in Fig. 1f where we compare the simulated proton spectra for NW lengths of $l = 0.5$, 2 and 10 μm with respect to their thickness-equivalent reference flat Cu foil spectra, along with the bare Au substrate case. All NW targets yield higher energies than their respective reference Cu foils, moreover the least performant NWs (i.e. $l = 10$ μm) provide equivalent kinetic energies than the most performant flat foil case, namely the 0.3 μm-thick Au substrate. The estimated maximum energy enhancement ratio is about 3 for $l = 0.5$ μm, 4.4 for $l = 2$ μm and goes up to a factor of 10 for $l = 10$ μm due to the low energies generated for such large thickness. We limited our simulations to 2D PIC simulations presented here, without exploring 3D PIC simulations, since our simulations already give a sufficiently complete idea of the main phenomena with regards to the enhanced acceleration mechanism, as well as offering a comprehensive view of the underlying phenomena occurring within the geometry optimization. However, we expect to observe lower enhancement ratios in the experiment since 2D PIC simulations are known to overestimate the electrons energies by a factor in the range of 1.5-2[58,59] through greater $\boldsymbol{J} \times \boldsymbol{B}$ electron heating, although this effect can be compensated by the shorter travel time of hot electrons in the NW interspace in 2D[60]. This proton energy overestimation is further amplified for NWs due to an overestimated electron confinement, leading to stronger TNSA electric field[60]. In the experiment, described in the following section, we did not use the proton-optimized gap of 800 nm due to limitations in the fabrication methodology and this will be the subject of further investigations. Nevertheless, the experimentally used gap of $g = 200$ nmalready provides a substantially increased laser-to-proton conversion efficiency by a factor of 5 with respect to the flat target case, moreover being near-optimal for the laser energy absorption as shown in Fig. 1d (blue diamonds).

Experimental campaign

We performed experiments on the high-power Ti:Sapphire laser of the Lund Laser Center (LLC)[61] in Lund (Sweden). The system benefits of a double plasma mirror (DPM) configuration providing an Amplified Spontaneous Emission (ASE) pedestal contrast better than of 10^{-11} at 100 ps and 10^{-9} at 3 ps before the main pulse, with an energy transmission efficiency of 40%. Having an ultra-high contrast is essential for this type of study in order to keep the nanostructures intact when the main pulse arrives. The laser pulses had an energy of $\mathcal{E}_L = 0.35$ J on target, a duration of $\tau_L = 35$ fs yielding a peak power of 10 TW at a central wavelength of $\lambda_0 = 800$ nm, and the beam was focused down using an $f/3$ off-axis parabola to a focal spot diameter of $w_{\mathrm{FWHM}} = 3$ μm, providing an on-target intensity of $I_0 \sim 5 \times 10^{19}$ W/cm^2. The p-polarized pulses were incident on the targets at an angle of 20° with respect to target-normal direction to allow for the measurement of the reflected laser pulse and to avoid sending the reflection back in the laser system as when using 0° incidence, while preserving an efficient TNSA mechanism. The proton beam spectrum was monitored by a calibrated Thomson Parabola (TP) spectrometer

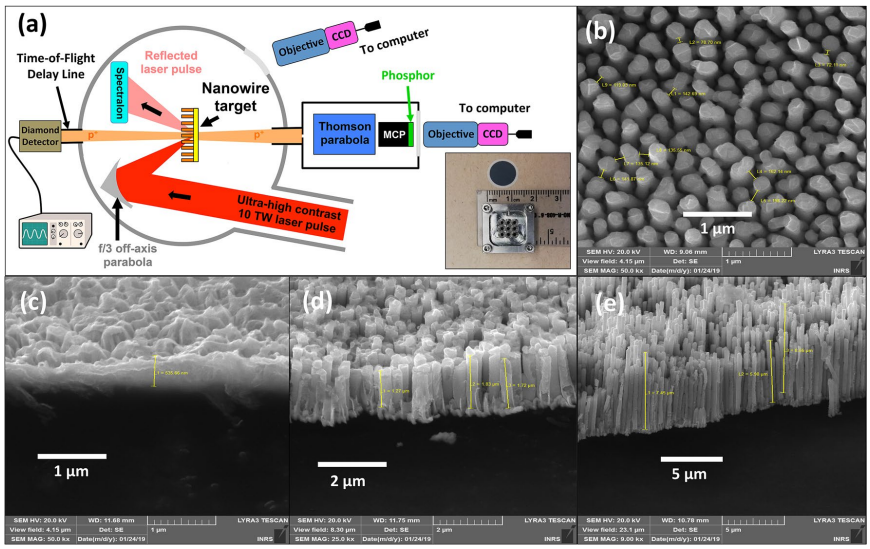

Figure 2. Experimental setup. (**a**) Schematic of the experimental setup showing the three main proton monitoring systems: a TP spectrometer at 0°, a TOF line at 180° and a Spectralon diffuser. (inset) Target holder specifically designed for holding the NW discs. (**b**–**e**) SEM images showing (**b**), a top view of the nanowire target. (**c**–**e**) different NW targets of different lengths (0.3 µm in (**c**), 1.5 µm in (**d**) and 8 µm in (**e**).

placed at 0°, coupled to a microchannel plate-phosphor assembly for particle detection. In order to monitor particles accelerated in the laser-backward direction, we used a Time-of-Flight (TOF) delay line oriented at 180° with respect to the TP spectrometer. In the TOF detector, the ions were detected using a Chemical Vapor Deposition (CVD) diamond detector[62–64]. The reflectivity of the target was measured using a Spectralon diffuser placed at the specular reflection angle compared to the impinging laser; an image of the scattered light was recorded on a CCD through a window of the chamber. Details of the experimental setup are presented in Fig. 2. As targets we used Cu NW targets, with an average diameter of $d = 200$ nm, gap of $g = 200$ nm and five different verified lengths of $l = 0.5$, 1, 2, 5 and 10 µm. The used NW geometry provided an areal density of 6.25 NW/µm^2 (i.e. reduction of the effective electron density by a factor of 0.4 compared to Cu flat targets) and therefore approximately 44 NWs were located within the focal spot area. This NW density is close to the numerical optimum of the present study ($d_{opt} = 200$ nm and $g_{opt} = 800$ nm), that yields 7 NWs per focal spot, and slightly higher that the optimum reported in the work of Dozières et al.[51] (around 1 NW per focal spot area). We expect that this difference is due to the higher laser intensity (1.5×10^{21} W/cm^2) used in their study, as increasing the intensity would require longer traveling time for attaining maximal heating of the ejected electrons, suggesting the use of larger gap distances (i.e. lower number of NW per focal spot). The NWs were grown on a $s = 300$ nm thick Au substrate (the total thickness of the target being $s + l$) by electrodeposition using Anodic Aluminum Oxide (AAO) templates of 1 cm in diameter (available commercially, WHATMAN Anodisc), following the methodology described in Mondal et al.[44] and adapted from Gao et al.[65]. The NW production methodology is easily implementable in-house and inexpensive, allowing for large amounts of targets to be produced at once. However, the method still presents some limitations to vary the parameters d and g, another reason why we focused our attention on the experimental investigation of the parameter l. A specific target holder was designed for the NW discs allowing for 9 repetitive shots per disc, as shown in the inset of Fig. 2a. In order to test the repeatability of the data, and ensure statistically valid information, each target type was irradiated several times (3-18 times, depending on the available targets). Scanning Electron Microscope (SEM) images of the NW targets are shown in Fig. 2b–e for three different NW lengths. One can see that for very short NWs (NW length of 0.3 µm as indicated in Fig. 2c), the target surface appears to be very irregular and rugged, due to the too short growth time. Longer growth times form the as-expected forests of wires, as visible in Fig. 2d (1.5 µm) and 2e (8 µm). The NW lengths l are measured using the postprocessing software of the SEM microscope, so that the NW lengths l are calibrated with the chemical reaction growth time. Reference shots were also taken on five types of Cu foils with thicknesses equivalent to the different NW lengths l (0.5, 1, 2, 5 and 10 µm), along with the NW bare Au substrate.

Figure 3a shows the averaged proton spectra for different target types. Only three NW lengths ($l = 0.5$, 2 and 10 µm) are shown for better visualization of the data, along with their respective reference Cu foils. Considering the reference Cu foils, one can observe an improvement in the proton yield and maximum proton energy with decreasing foil thickness, the expected behavior for the TNSA mechanism. We find that any NW target we used results in an equivalent or higher proton yield and maximum proton energy than what is obtained with the flat

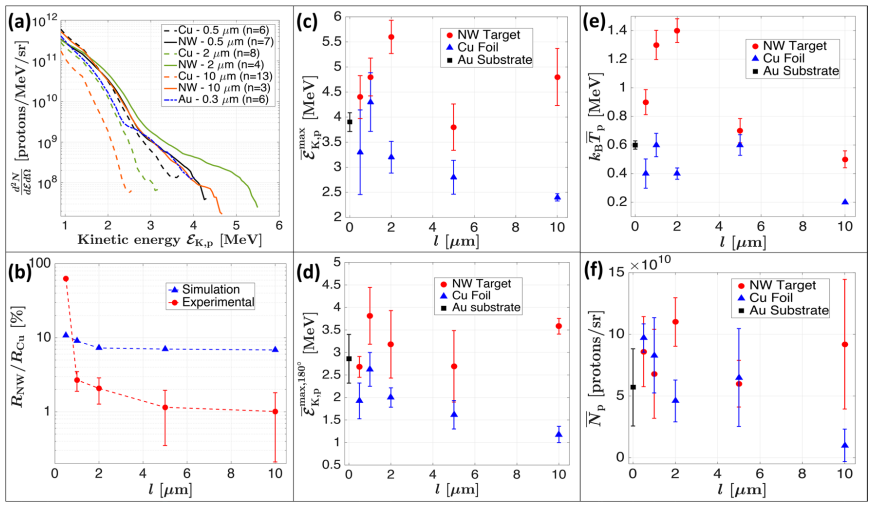

Figure 3. Experimental results for NW length investigation. (**a**) Averaged spectra for NW targets (solid lines) along with their thickness-equivalent Cu reference foils and the bare Au substrate of 0.3 μm (dotted lines). (**b**) Reflectivity ratios of NW targets and Cu foils as obtained experimentally from the Spectralon diffuser (red points) and through PIC simulations (blue diamonds). Proton spectra characteristics (**c**–**f**) shown for NW targets (red circles), Cu reference foils (blue diamonds) and the bare 300 m-thick Au substrate (black squares). (**c**) Average maximum proton energy in the forward acceleration direction $\overline{\mathcal{E}}^{max}_{K,p}$. (**d**) Average maximum proton energy in the backward acceleration direction $\overline{\mathcal{E}}^{max,180°}_{K,p}$. (**e**) Average proton temperature $k_B\overline{T}_p$ as obtained by a linear fit on the log-plotted spectra in the high energy section. (**f**) Average integrated proton numbers $\overline{N}_p$ for $\mathcal{E}_{K,p} > 1$ MeV. The cumulated number of shots are of 7, 7, 4, 4 and 3 for NWs of length $l = 0.5$, 1, 2, 5 and 10 μm respectively. For Cu foils, the cumulated number of shots are of 6, 18, 8, 10 and 13 for thicknesses of 0.5, 1, 2, 5 and 10 μm respectively, as well as 6 shots the Au substrate. The shown uncertainties are the total standard deviations (instrument accuracy and shot-to-shot fluctuation summed in quadrature).

targets, including the bare Au substrate, in a very similar situation to what is observed through simulations (see Fig. 1f). The NW length that yields the highest proton energies is found to be $l = 2$ μm with maximal proton energy of 5.6 MeV compared to 3.2 MeV for a Cu foil of equivalent thickness, giving a mean enhancement ratio of 1.8. Indeed, for NW lengths below 2 μm, the wires are not yet formed as well-defined cylinders (see Fig. 2c). This decreases the laser energy absorption and therefore reduces their performance in enhancing the TNSA acceleration mechanism. Nevertheless, a non-negligible enhancement is observed even for the rough surfaces as for the case of $l = 0.5$ μm, and is likely to be attributed to a different absorption mechanism such as from stochastic incidence angles as shown in Cerchez et al.[66]. As a comparison, the mean enhancement ratio for maximum energy with $l = 10$ μm is of about 2, however, the absolute maximum energy is slightly lower, 4.8 MeV, as expected for thicker targets. Hence, there is a compromise when choosing the working point: Short NW lengths produce higher proton energies, but are difficult to manufacture in a well-defined NW geometry. Longer NW lengths produce well-defined NW forests yielding high laser energy absorption, but decrease the TNSA mechanism efficiency due to the increased thickness[55]. In Fig. 3b we show the experimental and simulated laser-energy reflectivity ratios between NW targets and reference Cu foils. We can note that the reflectivity ratio obtained from PIC simulations very slowly increases from 7% for a target thickness of $l = 10$ μm to 10% for a thickness of $l = 0.5$ μm. The experimental reflectivity heavily increases for thicknesses below 2 μm since NWs become too short and form the aforementioned very rough surface (see Fig. 2c), which explains the less performant NWs with lengths of $l = 0.5$ and 1 μm. Nevertheless, we observe a good agreement between the simulated and experimental reflectivity ratio in terms of functional trend and amplitude, moreover also exhibiting the inverse trend as observed in Fig. 1e for laser energy absorption. The difference is due to the fact that during the experiment only the energy reflected in the specular direction is captured by the CCD looking at the Spectralon. Part of the energy is dispersed also by non-aligned nanowires, which leads to an underestimation of the total reflectivity. Figure 3c–d show the maximum proton energy measured on the TP spectrometer placed at 0° in the forward acceleration direction $\overline{\mathcal{E}}^{max}_{K,p}$, in addition to those recorded at 180° in the backward acceleration direction $\overline{\mathcal{E}}^{max,180°}_{K,p}$ using the TOF lines equipped with a diamond detector. One can see that all the NW types are univocally superior in maximum energy compared to their equivalent Cu foils and also with respect to the bare Au substrate. TP measurements depicted in Fig. 3c show that the highest maximum energy is achieved for a NW length of 2 μm, before decreasing with shorter NWs of 0.5 and 1 μm. This represents a different but complementary trend than what is shown with simulations on Fig. 1e, but is explained by the fact that experimental NWs with thickness

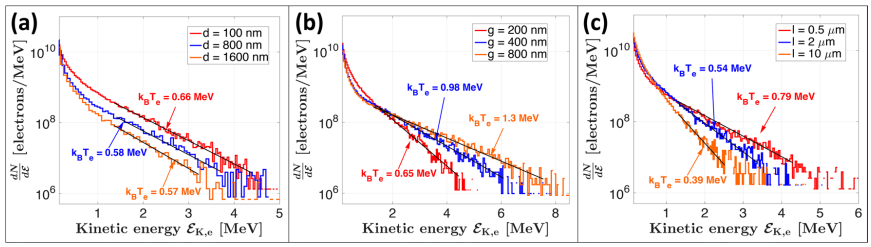

Figure 4. Simulated electron spectra at t = 40 fs after the interaction with the laser pulse for different NW (**a**) diameters *d*, (**b**) gaps *g* and (**c**) lengths *l*. Values of *d*, *g* and *l* are chosen for better visualization. The black lines correspond to linear fits in the relevant energy range for the retrieval of the hot electron temperature T_e^{hot}.

below 2 μm do not form a uniform and well-defined NW forest compared to longer lengths. Consequently, this effect decreases the laser energy absorption and thus also the efficiency of the TNSA mechanism. As a results, a decrease in performance is observed compared to a more efficient TNSA mechanism for shorter NWs, hence why the optimum is slightly shifted at $l = 1$ μm in backward direction. This suggests that the experimental optimal length is in the range of $l = 1$–2 μm. Some manufacturing problems occured with the $l = 5$ μm target, preventing to obtain perfectly flat NW targets. As a result, the performance of $l = 5$ μm is lower than for $l = 10$ μm. It is likely that this changed the target-normal direction and thus reduced the measured maximum energy. TOF measurements (see Fig. 2d) show that even in the backward direction the enhancement in the maximum proton energy is significant for long NWs, despite a lower absolute energy value. The correlation between forward and backward direction acceleration mechanism has already been investigated for thin foil targets, and for high contrast lasers the two target sides showed similar maximum energy trends[67–69], with maximum energy slightly in favor of the forward acceleration scheme. The maximum proton energy in the backward direction is increased by a factor of 1.4 for target thicknesses of $l = 0.5$ μm, up to a factor of 2.9 at $l = 10$ μm. This effect is expected as the increase in laser energy absorption from NW geometry produces a larger amount of electrons and with higher temperatures in the plasma located also at the front target surface (the NW side), which expands and induces a charge separation that catalyzes the backward acceleration of ions. Even in the presence of nanostructures, the plasma expansion does uniformize the sheath electric field over time and produces an enhanced proton acceleration in the backward direction. On the temporal scale, the sheath electric field may have a lower peak value and gradient due to the rough NW surface compared to a flat surface, nevertheless the higher number of hotter electrons ultimately leads to a greater energy transfer to the ions also on the front target surface for backward acceleration. This is coherent with what is observed in the works of Dalui et al.[38], Cristoforretti et al.[39] and as well in Bagchi et al.[37] in the sub-relativistic regime where the laser intensity (10^{16} W/cm^2) is sufficient to strongly ionize the target bulk and induces a charge separation that leads to the backward ion acceleration. In Fig. 3e we show theextracted energetic proton temperature $k_B \overline{T}_p$ as obtained by fitting a straight line in the high energy part of the log-spectrum just before the cutoff (i.e. Maxwell-Boltzmann distribution). The straight lines for obtaining the proton temperature are not shown in Fig. 3e for better visualization, but examples are shown in Fig. 4. The trend regarding proton temperatures is more clear than for the maximum energies; Since the temperature is an average metric over the hot proton population, it is less dependent on variations of the target-normal direction compared to the measurement to the TP spectrometer. It is clearly possible to see in Fig. 3e, the increasing proton temperature with decreasing NW length, having its optimum at $l = 2$ μm, before decreasing back for $l < 2$ μm due to misformed NWs. The proton temperatures are also all superior compared to their respective reference Cu foils, the enhancement ratio going up to a factor of 3.5 for $l = 2$ μm. In Fig. 3f we show the total proton number per unit solid angle $\overline{N}_p$ obtained by integrating the spectra for proton energies > 1 MeV. The trend here is less clear; proton numbers are slightly lower for some NW cases, but this is strongly dependent on the low energy threshold that we fixed when computing the integrated number and on the orientation of target-normal which produces a high statistical fluctuation in the measurement, given the small acceptance angle of the TP diagnostic. Nevertheless, the proton number enhancement is clear for $l = 2$ μm and $l = 10$ μm for enhancement ratios going up to 2.5 and 9, respectively.

As can be seen from these results, in all cases NW configurations improve the acceleration mechanism compared to flat foils of equivalent thickness, even when compared to the very thin Au substrate of 300 nm thick. This demonstrates that the enhancement mostly comes from the laser energy confinement determined by the NW parameters *d* and *g*, and is influenced to a lesser extent by the NW length *l*. The results obtained in this work are in agreement with the work of Khaghani et al.[50] with regards to maximum energy and number enhancement ratios. Moreover, they measured hot electron temperature improvements of a factor of 2 at a lower laser intensity (5×10^{17} W/cm^2), in agreement with our factor of 2, as shown for the electron temperature calculations through simulations presented in the next section. Concerning the work of Dozières et al.[51], the maximum energy enhancement ratios are again in good agreement with those of the present study.

Underlying physical phenomena and discussion

In light of the experiments, we analyzed the simulations to highlight the underlying physical mechanisms responsible for the enhanced proton acceleration. In Fig. 4 we show the electron spectra immediately after the interaction of the laser pulse with the target at t = 40 fs. The hot electron temperature T_e^{hot} was calculated by obtaining the slope of a straight line fit in the high-energy part of the log-spectra, as for a Maxwell-Boltzmann distribution where $\frac{dN}{d\mathcal{E}} \sim e^{-\mathcal{E}_K/k_B T}$. The number of hot electrons N_e^{hot} was then calculated by integrating the spectra for energies above the ponderomotive potential $\mathcal{E}_{pond} = m_e c^2 \left(\sqrt{1 + \frac{a_0^2}{2}} - 1 \right) = 1.47$ MeV, where a_0 is the normalized amplitude of the vector potential. On the first hand, we note from Fig. 4a that the hot electron temperature does not vary significantly with increasing NW diameter d (i.e. the slope does not change), however the number of hot electrons continuously decreases with increasing d (i.e. spectra are shifted downwards). Since large NW diameters tend towards the flat target case, this suggests that the NW diameter optimum for protons is due to an increased production of hot electrons, balanced by an increased reflection of the energy from the NW tips. On the other hand, varying the NW gap induces significant changes in the slope at high energies (i.e. the hot electron temperature) as we can observe in Fig. 4b, which is also observed in the work of Blanco et al.[27] and Vallières et al.[42]. The empty space between the nanostructures allows to eject and heat electrons from the NW boundaries by the laser pulse through Brunel-type and $\boldsymbol{J} \times \boldsymbol{B}$ absorptions. These electrons are then further accelerated by DLA due to a greater time of flight before re-collision with the target bulk, thus increasing the temperature of the population. Finally in Fig. 4c, we note that increasing the NW length produces a reduction of both the hot electron number, since less low energy electrons can cross an increasingly thicker target, and the hot electron temperature. This results in an increased energy loss for thicker targets.

Showing that the behavior of n_e and T_e with nanostructured targets still respects fundamental equations of the TNSA mechanism, as presented by the work Mora[52], denotes a pure enhancement of the hot electron cloud by the nanostructures. To show that this occurs without any new unexpected effects facilitates the comprehension of the enhancement process. This is very important in order to guide the subsequent advances in enhanced laser-driven proton beams with nanostructures. To do so, we have checked the correspondance of N_e^{hot} and T_e^{hot} with $E_{sheath} = \sqrt{n_e k_B T_e / \varepsilon_0}$ and have first calculated $\overline{\boldsymbol{E}}_{x,theory}^{max} \propto \sqrt{N_e^{hot} k_B T_e^{hot}}$, and further evaluated the maximum longitudinal electric field from the simulations $\overline{\boldsymbol{E}}_{x,sim}^{max}$. More precisely, $\overline{\boldsymbol{E}}_{x,sim}^{max}$ is investigated in the simulations as the time-averaged maximum longitudinal electric field defined as follows:

$$\overline{\boldsymbol{E}}_{x,sim}^{max} = \frac{1}{\tau_{acc}} \int_{t_0}^{t_f} \max_{x,y} \left[\boldsymbol{E}_x(x,y,t) \right] dt \tag{1}$$

where t_0 is the laser pulse interaction time with the target, t_f is the time where the simulation ends and $\tau_{acc} = t_f - t_0$ is the acceleration time. The metric presented in Eq. (1) allows to remove the temporal variation of the electric field, which is disturbed compared to the typical flat target case due to the NW shape, and rather looks at the global effect as is observed with the simulated or measured proton spectra. The variation of $\overline{\boldsymbol{E}}_{x,sim}^{max}$ with d, g and l, compared to $\overline{\boldsymbol{E}}_{x,theory}^{max}$, is shown in Fig. 5. As it is possible to observe in Fig. 5a–e, there is a clear proportionality between $\overline{\boldsymbol{E}}_{x,sim}^{max}$ and $\overline{\boldsymbol{E}}_{x,theory}^{max}$ as they exhibit the same functional trend. Moreover, all parameters show the same trend and optima (d_{opt} = 100-200 nm, g_{opt} = 800 nm and $l_{opt} = 0.5\,\mu$m) as for the geometry optimization presented on Fig. 1. This brings a very comprehensive view of the effect of d, g and l on the TNSA mechanism. In particular, d increases the hot electron density, g is the driver for hot electron temperatures, which combined together produce an enhanced accelerating sheath electric field that ultimately leads to improved proton beam characteristics. This latter parameter g is key to achieve the highest value of temperatures and thus of the rooted product $\sqrt{N_e^{hot} k_B T_e^{hot}}$ for g = 800 nm, in agreement with the proton optimum presented in Fig. 1d. We have further verified the correspondence with the theoretical maximum proton energy expected from Mora[52], i.e. $\mathcal{E}_{K,p}^{max} = 2 k_B T_e \left[\ln \left(t_p + \sqrt{t_p^2 + 1} \right) \right]^2$ with $t_p = \omega_{p,i} t / \sqrt{2}e$ being the normalized acceleration time and $\omega_{p,i} = \sqrt{Ze^2 n_e / m_i \varepsilon_0}$ being the ion plasma frequency. Using the maximum proton energies extracted from simulations, as well the extracted hot electrons numbers N_e^{hot} and temperatures $k_B T_e^{hot}$, we compare in Fig. 5b–f the theoretical $\mathcal{E}_{K,p,theory}^{max}$ and simulated $\mathcal{E}_{K,p,sim}^{max}$ maximum energies using the proportionality presented in the following Eq. (2):

$$\boldsymbol{\mathcal{E}}_{K,p,theory}^{max} \propto 2 k_B T_e^{hot} \left[\ln \left(\sqrt{N_e^{hot}} + \sqrt{N_e^{hot} + 1} \right) \right]^2 \tag{2}$$

As is possible to note from Fig. 5c–d, the functional behavior is well reproduced from theory (red markers in Fig. 5b–f) and is furthermore in agreement with the shapes of the laser-to-proton conversion efficiencies C_{proton} shown in Fig. 1c, d (red markers). The linear dependence of $\mathcal{E}_{K,p}^{max}$ on T_e and logarithmic dependence on n_e, combined with the previously demonstrated relationships $T_e(d,g) \simeq T_e(g)$ and $n_e(d,g) \simeq n_e(d)$ (for a fixed optimized length l_{opt}) extracted from Fig. 4, highlights the predominant importance of the parameter g to achieve the highest proton energies.

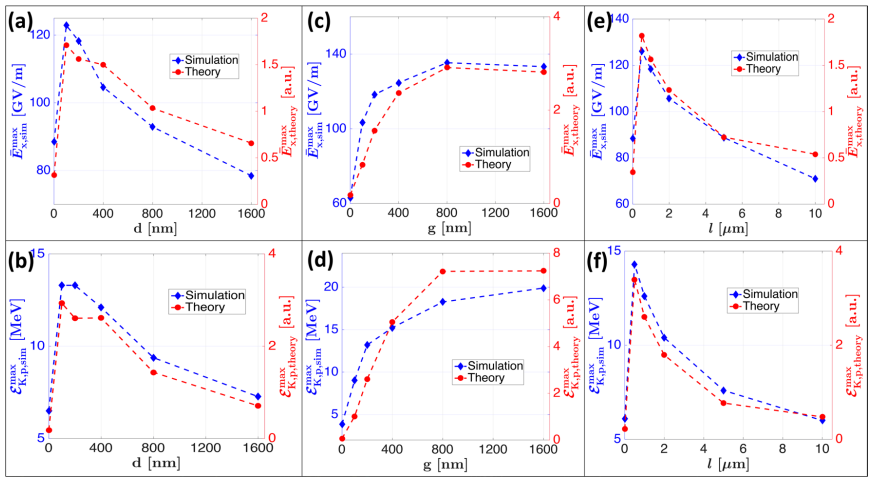

Figure 5. Time-averaged maximum longitudinal accelerating electric field $\bar{E}^{max}_{x,\,sim}$ (blue diamonds) calculated using (1) variation with NW (**a**) diameter d, (**c**) gap g and (**e**) length l, compared to $\bar{E}^{max}_{x,\,theory}$ (red dots). Simulated maximum proton energies $\mathcal{E}^{max}_{K,p,sim}$ variation with NW (**b**) diameter d, (**d**) gap g and (**f**) length l, compared to $\mathcal{E}^{max}_{K,p,theory}$ (red dots) calculated using (2).

Regarding the discrepancy between the experimental and numerical maximum energy enhancement ratios of respectively 2 and 3, this is partially due to the very uniform and quasi-periodic geometry within the simulation box, whereas with the experimental NWs there is a distribution of gap distances within the focal spot area of the laser which lowers its efficiency. Concerning the optimal NW length l, shorter NWs are the most efficient to enhance the proton acceleration as correctly shown by simulations in the present study (Fig. 1e, f), down to the theoretical minimum proposed by Wang at 0.5 μm for a 800 nm laser wavelength. However, it is experimentally challenging to manufacture well-defined forests of short NWs using the electrodeposition methodology. This reduces the performance of too short NWs and produces an experimental optimum around $l = 1$–2 μm for this present study. On the one hand, even if long NWs are prone to generate more hot electrons due to an increased laser energy absorption (i.e. high hot electron density n_e), too long NWs produce an important energy loss of hot electrons going through the target bulk (i.e. lower hot electron temperature T_e) which has a greater impact on the maximum energy, as predicted by the Mora model. On the other hand, too short NWs, fabricated using the electrodeposition method used in this study, do not favor a high laser energy absorption due to a misformed NW forest, explaining the presence of an optimum that is clearly visible experimentally on Fig. 3e, but is not observable numerically on Figs. 1e and 5e, f. Since it is the rooted product of n_e and T_e that is of crucial importance for the TNSA sheath electric field enhancement, a greater number of hot electrons does not necessarily produce a more intense accelerating field if the electron temperature is consequently lower, hence emphasizing the need to find the experimental optimum as in the case of this study. Moreover, regarding the substrate thickness, it is important to note that a too thin substrate may also lead to an over-fragile structure, a substrate thickness of about $s = 1$ μm or of comparable size to the length l is recommended.

This type of analysis is translatable and in agreement with other types of monolayered quasi-periodic nanostructures such as nanospheres in Vallières et al.[42] or triangles in the work of Blanco et al.[27]. The best NW parameters for d and g are a compromise between high laser confinement in the interspace of NWs and reflection of the laser energy from the NW tips. According to our simulations, an optimized NW diameter d favors the generation of higher hot electron densities n_e due to the multiple reflections of the pulse which ejects more electrons, whereas an optimized gap distance g boosts the electron temperature T_e since electrons are accelerated by the EM wave in the nanostructure interspace before collision with the substrate, in agreement with previous numerical studies[27,42,54,56,57]. It is the proper combination of these two parameters d and g that enhances the maximal TNSA sheath electric field as described in the formula $E_{sheath} = \sqrt{n_e k_B T_e/\varepsilon_0}$. Regarding the forward-accelerated proton beam enhancement also obtained at a sub-relativistic intensity (2×10^{17} W/cm^2) in Khaghani et al.[50] (backward acceleration enhancement with nanostructures at sub-relativistic intensity was demonstrated in other works[36,37]), we conclude that, if the hot electron production is not hindered by too thick substrate or NW length, then the hot electron cloud reaching the rear-side of the target can be substantially boosted in terms of numbers and temperature due to the strong heating in the wire interspace even if the absorption mechanisms vary. The DLA occurring within a few laser cycle during this time of flight in the NW gap space is therefore essential and reduces the need of very strict relativistic intensities for forward ion acceleration.

In conclusion, this work is the first to present a systematic study of the enhancement provided by nanowire targets for laser-driven proton acceleration in terms of the relevant geometrical parameters d, g and l, but also

regarding their influence on the proton spectra characteristics (proton maximum energy, temperature and total number) in the TNSA regime, hence providing a comprehensive understanding of the proton beam enhancement with nanostructured targets. Experimental evidence exhibits high enhancement ratios for the proton spectra characteristics, in agreement with PIC simulations. A geometry optimization was also performed through PIC simulations allowing to define the best parameters for the LLC laser characteristics. A larger gap value of $g = 800$ nm between the nanowires is expected to provide even higher enhancement ratios according to our simulations. The aforementioned improvements will be the subject of a subsequent study. The easy production method along with the high enhancement ratios provided by NW targets open very promising avenues for laser-driven proton beam generation on ultra-high power laser facilities, where the proton energies would be of strong interest for material science, medical applications and laboratory astrophysics.

Methods

Nanowire Production. The Cu nanowire arrays were fabricated by the electrochemical deposition method, based on the methodology of Mondal et al.[44] which is adapted from Gao et al.[65]. The through-hole Anodic Aluminum Oxide (AAO) membrane (pore size: 0.2 μm, membrane thickness: 60 μm, WHATMAN Anodisc) was applied as the template for the electrochemical deposition of Cu NWs. With a layer of gold (300 nm) sputtered on the one side, the AAO membrane served as the working cathode electrode in a conventional three-electrode cell for the electrochemical deposition. The graphite carbon and the saturated calomel electrode (SCE) were applied as the counter and the reference electrode, respectively. The electrolyte was a mixture of 0.2 M $CuSO_4$ and 0.1 M H_3BO_3. Experiments were carried out by using a potentiostat (Autolab) with the constant potential of -1.20 V (vs. SCE) at room temperature. The length of the Cu NWs can be controlled between 0 and 20 μm by adjusting the deposition time during the synthesis. The nanowire diameter and the gap size were dictated by the template itself, which were around 200 nm for both and further confirmed by the Scanning Electron Microscope (SEM) characterization. For the SEM characterization, the as-prepared Cu nanowires embedded in the template were first immersed in a 1 M NaOH solution for 20 min to dissolve the AAO membrane. Then, they were rinsed in distilled water several times and let dry for 24 h prior to the shots. Special multi-target holders have been developed to perform multiple laser shots on one template. Prior to the laser shots, the AAO templates were dissolved inside the multi-target holder using the aforementioned methodology.

PIC simulations. The PIC simulations involve a Gaussian p-polarized laser pulse incident at 20° with respect to target-normal, at a wavelength of $\lambda_0 = 800$ nm, a pulse duration of $\tau_L = 35$ fs at Full-Width Half-Maximum (FWHM), focused down to a Gaussian focal spot size of $w_{\mathrm{FWHM}} = 3\,\mu$m on the target at an intensity of 6×10^{19} W/cm^2, leading to $a_0 = 5.3$ where a_0 is the normalized amplitude of the vector potential. The simulation grid uses $\Delta x = \Delta y = 20$ nm, $\Delta t = \Delta x/c = 66$ as and runs over 800 fs. The box size is of 4080×4000 cells ($102\lambda_0 \times 100\lambda_0$) in the transverse and longitudinal axes respectively. Copper nanowires were placed on a 300 nm thick gold foil, both with electron densities of $100n_c$, where n_c is the critical density at $\lambda_0 = 800$ nm. A 20 nm proton layer was placed at the back of the target with a density of $15n_c$. Copper and gold ion species were initiated at the 3+ ionization level with field and collisional ionizations enabled. We used 30 macroparticles per cell for electrons and the corresponding numbers for ion species to ensure charge neutrality in each cell at the initial state of the simulation. The investigated geometrical parameters were lengths of $l = 0$, 0.5, 1, 2, 5 and 10 μm, diameters of $d = 0$, 100, 200, 400, 800 and 1600 nm, as well as gaps of $g = 0$, 100, 200, 400, 800 and 1600 nm. Only one NW parameter was varied at a time around the nominal NW parameters of $d = 200$ nm, $g = 200$ nm and $l = 1$ μm. Each simulation runs 16 h on 600 cores.

Received: 13 March 2020; Accepted: 2 December 2020
Published online: 26 January 2021

References

1. Badziak, J. Laser-driven ion acceleration: Methods, challenges and prospects. *IOP Conf. Ser. J. Phys. Conf. Ser.* **95**, 012001 (2018).
2. Macchi, A., A Review of Laser-Plasma Ion Acceleration. arXiv:1712.06443 (2017).
3. Daido, H., Nishiuchi, M. & Pirozhkov, A. S. Review of laser-driven ion sources and their applications. *Rep. Prog. Phys.* **75**, 056401 (2012).
4. Romagnani, L. *et al.* Dynamics of electric fields driving the laser acceleration of multi-MeV protons. *Phys. Rev. Lett.* **95**, 195001 (2005).
5. Roth, M. *et al.* Fast ignition by intense laser-accelerated proton beams. *Phys. Rev. Lett.* **86**, 436 (2001).
6. Patel, P. K. *et al.* Isochoric heating of solid-density matter with an ultrafast proton beam. *Phys. Rev. Lett.* **91**, 125004 (2003).
7. Albertazzi, B. *et al.* Laboratory formation of a scaled protostellar jet by coaligned poloidal magnetic field. *Science* **346**, 325 (2014).
8. Yogo, A. *et al.* Measurement of relative biological effectiveness of protons in human cancer cells using a laser-driven quasi-monoenergetic proton beamline. *Appl. Phys. Lett.* **98**, 053701 (2011).
9. Metzkes, J., Cowan, T. E., Karsch, L., Kraft, S. D., Pawelke, J., Richter, C., Richter, T., Zeil, K. & Schramm, U., Preparation of laser-accelerated proton beams for radio-biological applications. *Nucl. Instrum. Methods Phys. Res. Sect. A* **653**, 172 (2011).
10. Doria, D. *et al.* Biological effectiveness on live cells of laser driven protons at dose rates exceeding 109 Gy/s. *AIP Adv.* **2**, 011209 (2012).
11. Roth, M. *et al.* Bright laser-driven neutron source based on the relativistic transparency of solids. *Phys. Rev. Lett.* **110**, 044802 (2013).
12. Barberio, M., Veltri, S., Scisciò, M. & Antici, P. Laser-accelerated proton beams as diagnostics for cultural heritage. *Sci. Rep.* **7**, 40415 (2017).
13. Barberio, M. & Antici, P. Laser-PIXE using laser-accelerated proton beams. *Sci. Rep.* **9**, 6855 (2019).
14. Barberio, M. *et al.* Laser-accelerated particle beams for stress testing of materials. *Nat. Comm.* **9**, 372 (2018).
15. Barberio, M. *et al.* Graphitization of diamond by laser-accelerated proton beams. *Carbon* **138**, 531–537 (2018).
16. Barberio, M. *et al.* Laser-generated proton beams for high-precision ultra-fast crystal synthesis. *Sci. Rep.* **7**, 12522 (2017).

17. Antici, P. *et al.* Numerical study of a linear accelerator using laser-generated proton beams as a source. *J. Appl. Phys.* **104**, 124901 (2008).
18. Antici, P. *et al.* A compact post-acceleration scheme for laser-generated protons. *Phys. Plasmas* **18**, 073103 (2011).
19. Wilks, S. .C., Kruer, W. .L., Tabak, M. & Langdon, A. .B. Absorption of ultra-intense laser pulses. *Phys. Rev. Lett* **69**, 1383 (1992).
20. Fuchs, J. *et al.* Laser-driven proton scaling laws and newpaths towards energy increase. *Nat. Phys.* **2**, 48–54 (2006).
21. Shi, G. & Kioupakis, E. Electronic and optical properties of nanoporous silicon for solar-cell applications. *ACS Photonics* **2**(2), 208–2015 (2015).
22. Aydin, K., Ferry, V. E., Briggs, R. M. & Atwater, H. A. Broadband polarization-independent resonant light absorption using ultrathin plasmonic super absorbers. *Nat. Commun.* **2**, 517 (2011).
23. Rosei, F. Nanostructured surfaces: Challenges and frontiers in nanotechnology. *Condens. Mater.* **16**(17), S1373 (2004).
24. Andreev, A. *et al.* Efficient generation of fast ions from surface modulated nanostructure targets irradiated by high intensity short-pulse lasers. *Phys. Plasma* **18**, 103103 (2011).
25. Klimo, O. *et al.* Short pulse laser interaction with micro-structured targets: Simulations of laser absorption and ion acceleration. *New. J. Phys.* **13**, 053028 (2011).
26. Yu, J. *et al.* Laser-driven proton acceleration using a conical nanobrush target. *Phys. Plasmas* **19**, 053108 (2012).
27. Blanco, M. *et al.* Table-top laser-based proton acceleration in nanostructured targets. *New J. Phys.* **19**, 033004 (2017).
28. Lübcke, A. *et al.* Prospects of target nanostructuring for laser proton acceleration. *Sci. Rep.* **7**, 44030 (2017).
29. Ji, L. *et al.* Exploring novel target structures for manipulating relativistic laser-plasma interaction. *High P. Laser Sci. Eng.* **5**, e14 (2017).
30. Fedeli, L., Formenti, A., Cialfi, L., Pazzaglia, A. & Passoni, M. Ultra-intense laser interaction with nanostructured near-critical plasmas. *Sci. Rep.* **8**, 3834 (2018).
31. Passoni, M. *et al.* Advanced laser-driven ion sources and their applications in materials and nuclear science. *Plasma Phys. Control Fusion* **62**, 014022 (2019).
32. Margarone, D. *et al.* Laser-driven proton acceleration enhancement by nanostructured foils. *Phys. Rev. Lett.* **109**, 234801 (2012).
33. Giuffrida, L. *et al.* Manipulation of laser-accelerated proton beam profiles by nanostructured and microstructured targets. *Phys. Rev. Acc. Beams* **20**, 081301 (2017).
34. Torrisi, L. *et al.* Nanostructured targets for TNSA laser ion acceleration. *Nukleonika* **61**, 103 (2016).
35. Torrisi, L. Ion acceleration from intense laser-generated plasma: Methods, diagnostics and possible applications. *Nukleonika* **60**, 207 (2015).
36. Bagchi, S. *et al.* Fast ion beams from intense, femtosecond laser irradiated nanostructured surfaces. *Appl. Phys.* **88**, 167–173 (2007).
37. Bagchi, S. *et al.* Surface-plasmon-enhanced MeV ions from femtosecond laser irradiated, periodically modulated surfaces. *Phys. Plasma* **19**, 030703 (2012).
38. Dalui, M. *et al.* Preferential enhancement of laser-driven carbon ion acceleration from optimized nanostructured surfaces. *Sci. Rep.* **5**, 11930 (2015).
39. Cristoforetti, G. *et al.* Transition from coherent to stochastic electron heating in ultrashort relativistic laser interaction with structured targets. *Sci. Rep.* **7**, 1479 (2017).
40. Ebert, T. *et al.* Laser-induced microstructures on silicon for laser-driven acceleration experiments. *High P. Laser Sci. Eng.* **5**, e13 (2017).
41. Passoni, M. *et al.* Toward high-energy laser-driven ion beams: Nanostructured double-layer targets. *Phys. Rev. Acc. Beams* **19**, 061301 (2016).
42. Vallières, S., Barberio, M., Scisciò, M., d'Humières, E. & Antici, P. Enhanced laser-driven proton acceleration using ultrasmall nanoparticles. *Phys. Rev. Acc. Beams* **22**, 091303 (2019).
43. Wang, W.-M., Sheng, Z.-M., Yu, M. Y. & Zhang, J. A model for the efficient coupling between intense lasers and subwavelength grating targets. *Phys. Plasma* **15**, 030702 (2008).
44. Mondal, S. *et al.* Aligned copper nanorod arrays for highly efficient generation of intense ultra-broadband THz pulses. *Sci. Rep.* **7**, 40058 (2017).
45. Kulcsár, G. *et al.* Intense picosecond X-ray pulses from laser plasmas by use of nanostructured @@Velvet@@ targets. *Phys. Rev. Lett.* **84**, 22 (2000).
46. Purvis, M. A. *et al.* Relativistic plasma nanophotonics for ultrahigh energy density physics. *Nat. Photonics* **7**, 796–800 (2013).
47. Bargsten, C. *et al.* Energy penetration into arrays of aligned nanowires irradiated with relativistic intensities: Scaling to terabar pressures. *Sci. Adv.* **3**, 1601558 (2017).
48. Hollinger, R. *et al.* Efficient picosecond X-ray pulse generation from plasmas in the radiation dominated regime. *Optica* **4**(11), 111344 (2017).
49. Moreau, A. *et al.* Enhanced electron acceleration in aligned nanowire arrays irradiated at highly relativistic intensities. *Plasma Phys. Control Fusion* **62**, 014013 (2020).
50. Khaghani, D. *et al.* Enhancing laser-driven proton acceleration by using micro-pillar arrays at high drive energy. *Sci. Rep.* **7**, 11366 (2017).
51. Dozières, M. *et al.* Optimization of laser-nanowire target interaction to increase the proton acceleration efficiency. *Plasma Phys. Control Fusion* **61**, 065016 (2019).
52. Mora, P. Plasma expansion into a vacuum. *Phys. Rev. Lett.* **90**(18), 185002 (2003).
53. Sentoku, Y. & Kemp, A. J. Numerical methods for particle simulations at extreme densities and temperatures: Weighted particles, relativistic collisions and reduced currents. *J. Comput. Phys.* **227**(14), 6846–6861 (2008).
54. Martinez, B., d'Humières, E. & Gremillet, L. Synchrotron emission from nanowire arraytargets irradiated by ultraintense laser-pulses. *Plasma Phys. Control Fusion* **60**, 074009 (2018).
55. Dong, Q. L., Sheng, Z.-M., Yu, M. Y. & Zhang, J. Optimization of ion acceleration in the interaction of intense femtosecond laser pulses with ultrathin foil. *Phys. Rev. E* **68**, 026408 (2003).
56. Cao, L. *et al.* Control of the hot electrons produced by laser interaction with nanolayered target. *Phys. Plasmas* **17**, 103106 (2010).
57. Cao, L. *et al.* Enhanced absorption of intense short-pulse laser light by subwavelength nanolayered target. *Phys. Plasmas* **17**, 043103 (2010).
58. Liu, J.-L., Chen, M., Zheng, J., Sheng, Z.-M. & Liu, C.-S. Three dimensional effects on proton acceleration by intense laser solid target interaction. *Phys. Plasma* **20**, 063107 (2013).
59. Stark, D. J., Yin, L., Albright, B. J. & Guo, F. Effects of dimensionality on kinetic simulations of laser-ion acceleration in the transparency regime. *Phys. Plasma* **20**, 053103 (2017).
60. Jiang, S., Krygier, A. G., Schumacher, D. W., Akli, K. U. & Freeman, R. R. Effects of front-surface target structures on properties of relativistic laser-plasma electrons. *Phys. Rev. E* **89**, 013106 (2014).
61. Aurand, B. *et al.* A setup for studies of laser-driven proton acceleration at the Lund Laser Centre. *Laser Part. Beams* **33**, 59–64 (2015).
62. Marinelli, M. *et al.* Analysis of laser-generated plasma ionizing radiation by synthetic single crystal diamond detectors. *Appl. Surf. Sci.* **272**, 104–108 (2013).
63. De Angelis, R. *et al.* High performance diagnostics for Time-Of-Flight and X ray measurements in laser produced plasmas, based on fast diamond detectors. *J. Instrum.* **11**, C12048 (2016).

64. Cipriani, M. *et al.* Spectral characterization by CVD diamond detectors of energetic protons from high-repetition rate laser for aneutronic nuclear fusion experiments. *J. Instrum.* **14**, C01027 (2019).
65. Gao, T., Meng, G., Wang, Y., Sun, S. & Zhang, L. Electrochemical synthesis of copper nanowires. *J. Phys. Condens. Matter* **14**, 355363 (2002).
66. Cerchez, M. *et al.* Enhanced energy absorption of high intensity laser pulses by targets of modulated surface. *Appl. Phys. Lett.* **112**, 221103 (2018).
67. Fourmaux, S. *et al.* Investigation of laser-driven proton acceleration using ultra-short, ultra-intense laser pulses. *Phys. Plasmas* **20**, 013110 (2013).
68. Ceccotti, T. *et al.* Proton acceleration with high-intensity ultrahigh-contrast laser pulses. *Phys. Rev. Lett.* **99**, 185002 (2007).
69. Levy, A. *et al.* Proton acceleration with high-intensity laser pulses in ultrahigh contrast regime. *IEEE Trans. Plasma Sci.* **36**(4), 185002 (2008).

Acknowledgements
This work is supported by FRQNT (nouveaux chercheurs, Grant No. 174726, Equipe 2016-PR-189974), the National Sciences and Engineering Research Council of Canada (NSERC) (Discovery Grant RGPIN-2018-05772 and the Alexander-Graham-Bell Graduate Scholarship for S.V.), Compute Canada (Job: pve-323-ac) as well as the Canada Foundation for Innovation (CFI). This study has also received financial support from the French National Research Agency (ANR) in the frame of "the Investments for the future" Programme IdEx Bordeaux-ANR-10-IDEX-03-02, from the Swedish Research Council (VR) and the Knut and Alice Wallenberg Foundation (KAW). Concerning the use of the Lund Laser Center, we acknowledge support by Laserlab Europe (Grant Agreement 654148 under the European Union's Horizon 2020 research and innovation programme). We would like to thank Tsuneyuki Ozaki for the fruitful discussions, Anders Persson, Riccardo De Angelis and Pierluigi Andreoli for the technical support and Claudio Verona for lending us some equipment.

Author contributions
S.V., M.S., A.P., K.S., G.C., F.C., C.G.W. and P.A. conceived and conducted the experiments, S.V., M.S. and G.C. analyzed the experimental results, S.V. developed and analyzed the simulations under the guidance of E.H., Z.C. and S.S. developed and produced the nanowires, Z.C. and S.V. performed SEM on the nanowires, C.G.W., E.H. and P.A. supervised the project, S.V. and P.A. wrote the manuscript. All authors reviewed the manuscript.

Competing interests
The authors declare no competing interests.

Additional information
Correspondence and requests for materials should be addressed to S.V.

Reprints and permissions information is available at www.nature.com/reprints.

Publisher's note Springer Nature remains neutral with regard to jurisdictional claims in published maps and institutional affiliations.

Paper III

Laser-driven proton acceleration from ultrathin foils with nanoholes

G. Cantono, A. Permogorov, J. Ferri, E. Smetanina, A. Dmitriev, A. Persson, T. Fülöp, and C.-G. Wahlström
Scientific Reports 11:5006 (2021)

scientific reports

Check for updates

OPEN

Laser-driven proton acceleration from ultrathin foils with nanoholes

Giada Cantono[1]✉, Alexander Permogorov[1], Julien Ferri[2], Evgeniya Smetanina[3], Alexandre Dmitriev[3], Anders Persson[1], Tünde Fülöp[2] & Claes-Göran Wahlström[1]

Structured solid targets are widely investigated to increase the energy absorption of high-power laser pulses so as to achieve efficient ion acceleration. Here we report the first experimental study of the maximum energy of proton beams accelerated from sub-micrometric foils perforated with holes of nanometric size. By showing the lack of energy enhancement in comparison to standard flat foils, our results suggest that the high contrast routinely achieved with a double plasma mirror does not prevent damaging of the nanostructures prior to the main interaction. Particle-in-cell simulations support that even a short scale length plasma, formed in the last hundreds of femtoseconds before the peak of an ultrashort laser pulse, fills the holes and hinders enhanced electron heating. Our findings reinforce the need for improved laser contrast, as well as for accurate control and diagnostics of on-target plasma formation.

Starting from twenty years ago, laser-driven ion acceleration has been the object of tireless efforts of theoretical understanding and experimental optimisation, stimulated by the remarkable beam properties (in terms of duration, brightness, emittance) that promote the use of such sources in different applications (e.g. time-resolved radiography, isochoric heating and probing of warm dense matter, hadron therapy and PET isotope generation, fundamental studies of plasma and nuclear physics)[1–3]. To attain the beam quality required for each application, various acceleration mechanisms are currently being explored, developed hand in hand with laser and target technology, beam transport and diagnostics. Target normal sheath acceleration (TNSA) is up to now the most practised mechanism to generate proton and ion beams with tens of MeV of energy. In this process, a high-power laser pulse accelerates electrons at the front surface of thin, solid targets. Once some hot electrons travel through the target and escape into vacuum, the resulting space-charge electric field ionises atoms and hydrocarbon impurities on the rear surface, accelerating protons and heavier ions perpendicularly to it.

Increasing the energy transfer from the laser pulse to the hot electrons that develop the accelerating sheath field (i.e. increasing the absorption) results in larger yields and energies for the TNSA-driven ion beams. To this aim, a well-established strategy consists of adding micro- and nanostructures on the front surface of the target[4]. In the past decade, advances in the target manufacturing techniques and in the control of the laser performances have enabled experiments on various types of nanostructures[5], such as micropillars[6], nanowires[7], nanospheres[8], foams[9,10], or gratings[11,12]. At the same time, numerical simulations have explored how periodic arrangements of different shapes, sizes and geometries affect the mechanisms of electron heating[13–21], for example by providing larger areas for the laser to accelerate the plasma electrons, or by favouring charge recirculation and the occurrence of resonant processes[9–12]. Experiments with nanostructured targets have reported factors between 1.2 and 2.5 for the enhancement of the maximum proton energy with respect to simple flat foils. Faced with similar laser-to-proton energy conversion efficiencies, crucial aspects in the choice of the most efficient nanostructures become the costs of manufacturing and handling, which in turn depend on how stringent the geometrical constraints are[7,11,22].

In this context, we investigated the maximum energy of proton beams accelerated from flat foils of gold, perforated with a non-periodic distribution of nanometric holes (nanoholes, NHs). Previous experimental works on porous targets, composed of a periodic array of several-μm-long nanochannels, reported an increase of the X-ray yield when irradiating at sub-relativistic intensities (i.e. below 10^{18} W/cm^2)[23,24]. The use of perforated foils of sub-micrometric thicknesses to optimise laser-driven proton acceleration, however, has been explored only numerically[20,21,25,26], and to our knowledge no experiments in the relativistic regime have been performed so far. Particle-In-Cell (PIC) simulations showed that plasma electrons extracted from the edges and from the walls of the NHs locally amplify the electromagnetic field at the vacuum-plasma boundary. Electron experiencing this field gain more energy compared to non-structured foils, as they also benefit from a longer acceleration time due

[1]Department of Physics, Lund University, SE-22100 Lund, Sweden. [2]Department of Physics, Chalmers University of Technology, SE-41296 Göteborg, Sweden. [3]Department of Physics, University of Gothenburg, SE-41296 Göteborg, Sweden. ✉email: giada.cantono@fysik.lth.se

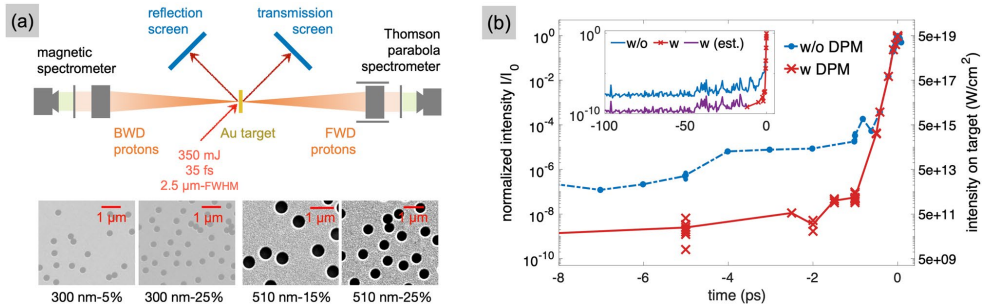

Figure 1. (**a**) Layout of the experimental setup and images of NH targets. Indicated are the NH diameter and filling factors. See Methods for additional information. (**b**) Laser temporal contrast measured by a third-order cross-correlator, with and without DPM (crosses and dots, respectively). The lines connect the averages of the points measured at each time. In the inset, the measurement without DPM is extended to include the ASE pedestal. The darker section of the curve with DPM is an estimation of the contrast where the signal falls below the dynamic range of the cross-correlator.

to longitudinal and transverse recirculation across the dense regions surrounding the holes. In a recent numerical study[26], these effects were related to the presence of individual holes on the target surface, rather than to their spatial distribution or to the reduced mass of the foil. With a greater number of highly energetic electrons crossing the target, enhancement factors of the maximum proton energy between 1.4 and 2 were reported for a variety of NH parameters[26].

From an experimental point of view, the relaxation in the geometrical constraints of the nanostructures reduces the technical difficulties associated with target fabrication. In this work, NH targets were produced with hole-mask colloidal lithography[27], a method where a metallic film is deposited on a distribution of plastic nanospheres of a chosen diameter. The nanospheres are then stripped away, leaving holes in the flat foil. Since the structuring does not include brittle elements such as nanospheres or nanowires, these foils can be efficiently produced in large areas and easily mounted on different supports to fit the experimental setup. For the same reason, the foil can be reduced to sub-μm thicknesses, which usually also favours proton acceleration[28,29].

On the other hand, it is well known that exposing ultrathin and nanostructured targets to relativistic intensities requires lowering the level of amplified spontaneous emission (ASE) and pre-pulses inherent to chirped pulse amplification-based laser systems. This would otherwise cause early heating, deformation of the target surface or, in the worst case, the creation of a plasma above critical density ($n_c = \epsilon_0 m_e \omega^2 / e^2$, ω being the laser frequency). Increasing the laser temporal contrast (i.e. the ratio between the peak intensity of the ultrashort pulse and any other radiation prior to it) so that the intensity of the ASE pedestal and of any pre-pulse is below the ionisation threshold of the target material is thus a prerequisite for this kind of experiments[30,31]. The High Power Laser Facility of Lund University (Sweden), where this work has been performed, houses a double plasma mirror (DPM)[31,32] that reduces at least by ~ 2 orders of magnitude the intensity of the radiation before the ultrashort pulse (cf. Fig. 1b). In this way, we achieve a temporal contrast of 10^{10} at the ASE timescale, and of 10^8 at 2 ps before the ultrashort pulse.

Our experiments aimed at testing, for the first time, the efficiency of NH targets irradiated by intense, high contrast laser pulses. However, despite varying the target parameters, the maximum energy of TNSA-driven protons was found to be equivalent to the one measured from flat foils of comparable thickness. We support our experimental results with new PIC simulations, where we investigated early plasma formation due to the finite contrast of our laser pulse. It appears that the energy deposited on target in the last ps before the peak of the pulse, when the DPM is ineffective, is enough to create a plasma that fills the NHs, thus hampering the expected enhancement in electron heating.

Results

Protons were accelerated irradiating flat foils of gold, both with and without NHs, with a multi-TW, high contrast laser pulse. We tested NH targets with various hole diameter d, filling factor ρ (i.e. the area of the foil covered by the holes, per unit area) and foil thickness t. Under identical conditions, we always performed measurements also from foils of the same thickness, but without NHs. These latter will be referred to as *regular* foils in the remainder of the text.

Figure 1 illustrates the experimental setup, including the laser focused at 45° angle of incidence, two diffuse reflectance screens for measuring the reflected and transmitted laser light during the interaction, and the diagnostics for protons emitted in both forward (FWD) and backward (BWD) directions.

Observing the cutoff energies of the protons accelerated in the BWD direction is a standard procedure to ensure that the laser contrast is high enough to prevent plasma formation on the target surface, as a step-like density profile enables efficient laser absorption through the vacuum-heating mechanism[33,34] and the establishment of the TNSA-driving fields also on the front side of the target. With good enough contrast, foils with sub-μm thicknesses typically produce similar proton energies in both FWD and BWD directions, giving an indirect

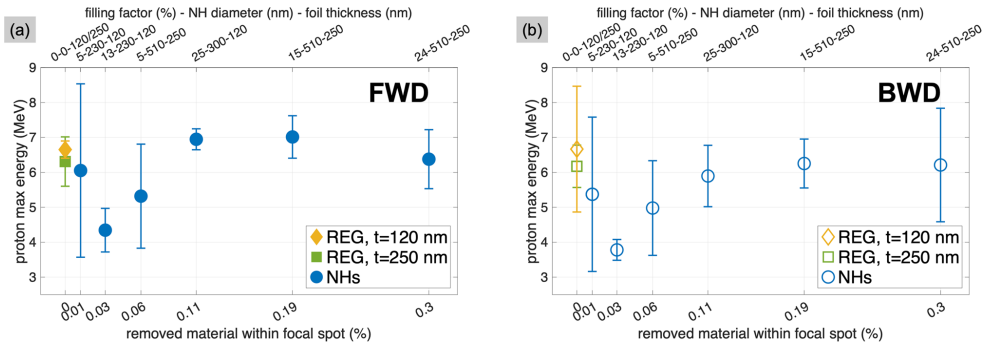

Figure 2. Proton maximum energies obtained from NH targets and regular foils, both in the FWD (**a**) and BWD (**b**) direction. For NHs, the amount of removed material is defined by the area occupied by NHs within the area covered by the laser focal spot. All target parameters (filling factor ρ, NH diameter d, foil thickness t) are listed in the top x-axis.

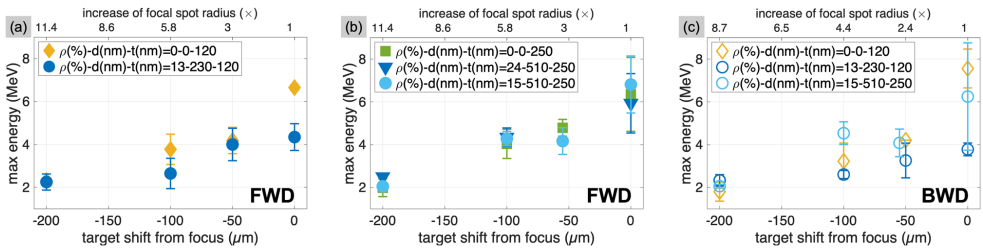

Figure 3. Proton maximum energies measured from regular and perforated foils when increasing the illuminated surface of the target. The increase of the focal spot radius is calculated as $[1 + (z/z_R)^2]^{0.5}$, with z being the shift from focus and z_R the Rayleigh length determined in the experiment. (**a**) FWD direction, for targets of 120 nm thickness. (**b**) FWD direction, for targets of 250 nm thickness. (**c**) BWD direction, for a selection of targets.

evidence of the survival of the target prior to the interaction with the pulse peak[35]. In our experiment, preliminary shots on the thinnest regular foils (120 nm of thickness) resulted in a maximum FWD energy of (6.7 ± 0.2) MeV, while the maximum BWD energy was (6.7 ± 0.7) MeV. As a consequence, and since in the fabrication of the NH targets the diameter of the holes was always larger than the foil thickness, the target structuring was assumed to be preserved during each laser shot.

The maximum energies of the protons accelerated from all the different targets, both in the FWD and BWD direction, are presented in Fig. 2. At a first glance, similar values and trends in both directions indicate efficient proton acceleration with all the types of targets, with the maximum energies in the FWD direction exceeding those in the BWD direction by less than 20%. However, more importantly, the results also show that the NH targets do not produce any proton energy enhancement, no matter the parameter we varied in our scan: The maximum energies are always found to be comparable with the values obtained from regular foils.

In NH targets with small filling factors, the number of holes inside the area covered by the laser focal spot varies relatively more the smaller the filling factor is. In order to ensure that NHs were irradiated, we hence varied the area covered by the focal spot by shifting the target along the focal axis. The consequent decrease of the laser intensity, up to a factor of ~ 100, would also limit any damage of the target possibly occurring in the residual time between the triggering of the DPM and the arrival of the ultrashort pulse. However, the results reported in Fig. 3 indicate once again that the maximum energy from NH targets never exceeds that from the regular foils, and the energies in both FWD and BWD direction remain comparable regardless of the target type or the position along the focal axis.

The results on the proton energies suggest that the NHs have been altered on the nanometric scale before the laser pulse reaches the peak intensity on the target, thus preventing the efficient electron heating that would support the enhanced proton acceleration. In Fig. 4, we present the measurements of the laser reflection and transmission from regular foils and NH targets, obtained with the diffuse reflectance screens. Here it is worth noting that, although displaying a slight increase in transmission for larger NH densities (Fig. 4a), all targets

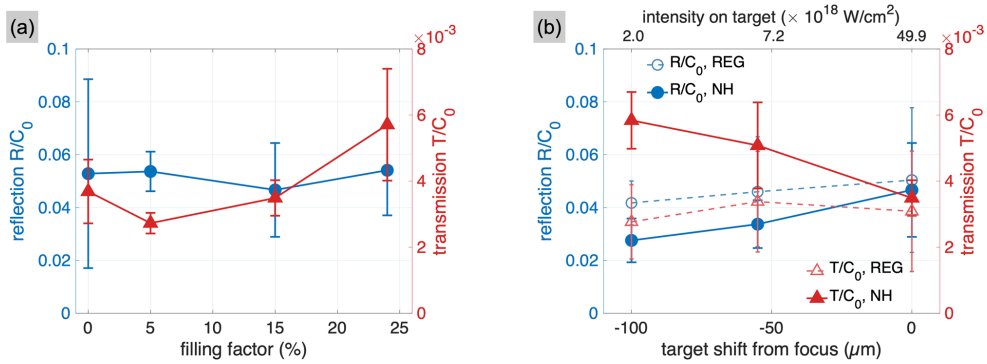

Figure 4. Reflection (dots) and transmission (triangles) signals, normalised to the signal C_0 measured in transmission without any target (blank shot), as a function of the filling factor (**a**) and of the shift of the target from the focal position (**b**). The focus scan is limited to the points where a sufficient signal to noise ratio could be detected on the reflectance screens. For all the measurements in this figure, the NH diameter was 510 nm and the foil thickness 250 nm. For the NH targets in (**b**), the filling factor was 15%.

produce similar absorption factors. This disagrees with the numerical simulations performed with a laser pulse with infinite temporal contrast[26], where a 70% decrease in reflection and 500% increase in transmission were observed when structuring the foil with NHs. A similar effect is observed when displacing the targets out of focus, as shown in Fig. 4b. When reducing the laser intensity on the NH targets, the transmission signal almost doubles compared to when the target is placed at focus, while the the reflection is 10 to 30% lower than the signal from regular foils. Despite hinting at the survival of the holes, the absorption coefficients that derive from the combination of the reflection and transmission measurements differ, for the regular foil and NH target, by only 1%.

In a separate set of measurements we changed the laser incidence angle to 20° and determined the FWD proton energy from NH targets (having $d = 230$ nm, $t = 120$ nm and $\rho = 15\%$) and from the corresponding regular foil. With observed cutoffs of (4.1 ± 0.4) and (5.1 ± 0.6) MeV, respectively, we conclude that neither in this case did the presence of NHs result in enhanced proton energies.

Led by the experimental observations, we performed two-dimensional PIC simulations to investigate how a pre-plasma, created in the last 100s of fs before the interaction with the relativistically intense laser pulse, affects the efficacy of NH targets. We characterise the pre-plasma by the scale length L of the exponential density profile that describes its expansion[36].

In a first set of simulations, a pre-plasma with an arbitrary scale length was added on the target before the interaction with an infinite-contrast laser pulse. Given the thinness of the foils, the pre-plasma was expanding from both front and rear surfaces, as well as from the walls of the holes in NH targets. A simple estimation for the scale length required to reach the relativistic critical density γn_c at the centre of the holes gives $L_{\text{fill}} = -d/[2\log(\gamma n_c/2n_{e0})]$, with d the NH diameter, $\gamma = (1 + a_0^2)^{1/2}$ with a_0 the normalised vector potential, and n_{e0} the initial electron density of the target. In these simulations, $d = 200$ nm, $n_{e0} \simeq 370 n_c$ and $a_0 = 6.7$ (i.e. a peak intensity $I_0 \simeq 10^{20}$ W/cm^2), resulting in $L_{\text{fill}} \simeq 20$ nm.

Figure 5a shows the electron and proton spectra from regular foils and NH targets when the pre-plasma scale length varies between 0 and 70 nm. In the case of regular foils (top row), slightly enhanced heating of 10 MeV electrons suggests a transition towards resonant absorption in correspondence of longer pre-plasmas ($L \geq 50$ nm). However, the maximum proton energy progressively decreases with increasing L, because the wider density ramp at the rear surface hampers the formation of the accelerating sheath field[37,38]. The results with NH targets (bottom row) indicate a stronger dependence on the scale length. First, increasing the scale length suppresses the large population of electrons between 5 and 12 MeV that is accelerated from the NH walls when $L = 0$ nm[26]. Second, in addition to the the gradual decrease as observed with the regular foil, the proton energies show a larger drop, from values around 25 MeV when $L < L_{\text{fill}}$, to 13 MeV in the opposite case. The effect of the pre-plasma on target absorption is presented in Fig. 5b. While the absorption of the regular foil (dashed lines) is almost constant for $L > 10$ nm, the NH target (solid lines) shows a 90% decrease in transmission and a 200% increase in reflection when L reaches 70 nm. At this point, absorption is similar for both targets, in agreement with the experimental results of Fig. 4.

A pre-plasma with $L \sim 50$ nm $> L_{\text{fill}}$ thus results in filling of the NHs and suppression of the enhanced proton acceleration. It is worth noticing that such estimation for L depends on how accurately the pre-plasma initialised on the different target surfaces reproduces their actual two-dimensional expansion. To get around this limitation, as well as to support the presence of the pre-plasma in the experiment, we performed a simulation where we represented the laser pulse using a sum of Gaussian functions, so as to fit the experimental measurement of the temporal contrast[39,40]. The fitted temporal profile is shown in Fig. 6a.

With some laser energy irradiating the unperturbed solid target before the peak of the pulse, holes are gradually filled up by the expanding plasma. This is clearly presented in Fig. 6b, which represents the temporal evolution of the plasma density inside the NHs. Such plasma reaches the relativistic critical density $\gamma n_c = 3.7 n_c$

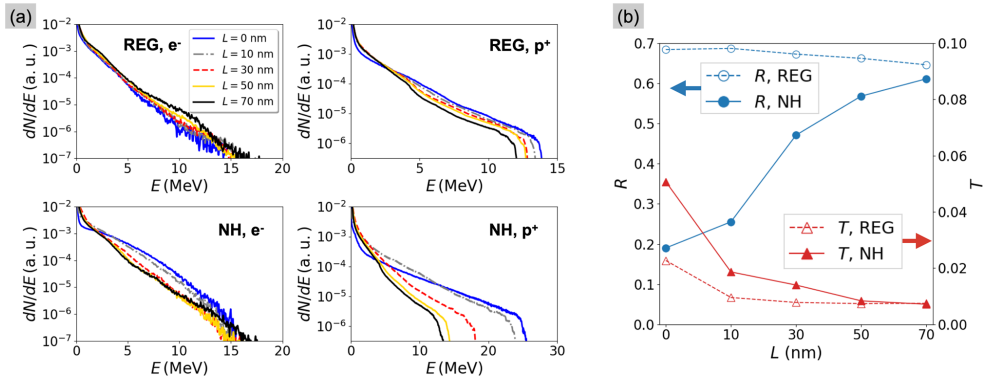

Figure 5. Numerical results from scanning the pre-plasma scale length. (**a**) Energy spectra from from regular foils (top) and NH targets (bottom). Electron spectra (left column) include all electrons recorded in the simulation box at the peak intensity, $t = 0$ fs, while proton spectra (right column) include the protons on the rear side of the target at $t = 250$ fs after the peak. (**b**) Reflection and transmission coefficients for both target types.

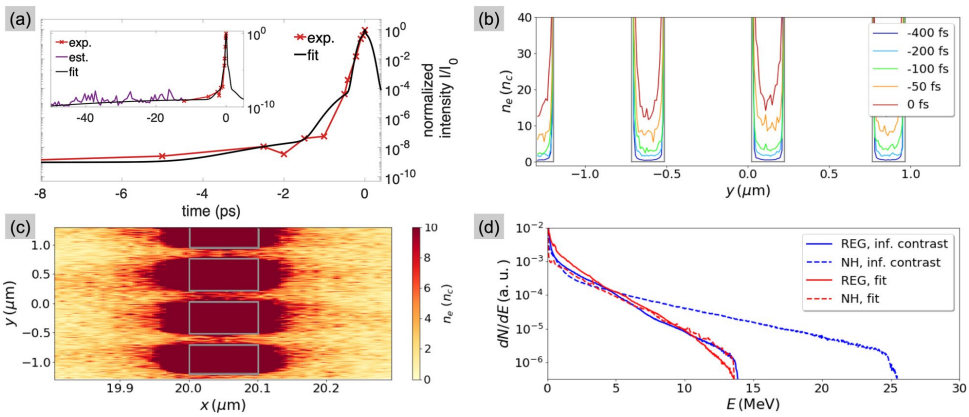

Figure 6. Results of the PIC simulations with finite contrast. (**a**) Profile of the laser pulse that fits the cross-correlator trace. The entire simulation setup is described in Methods. (**b**) Evolution of the plasma density inside the NHs at different times before the peak of the pulse (fixed at $t = 0$ fs). The traces are obtained by integrating the density maps along the whole target thickness. An example of density map, taken at −50 fs, is shown in (**c**), where the grey boxes highlight the original target shape. (**d**) Comparison of proton spectra from regular foil and NH target, obtained with either the infinite-contrast or with the fitted laser pulse.

at ~ -100 fs, and it has become fully overdense, with $n_e \sim 15 n_c$, at the arrival of the peak. At this time, the scale length is estimated as $15 n_c = 2 n_{e0} \exp[-d/(2L_{\mathrm{PIC}})]$, giving $L_{\mathrm{PIC}} \simeq 25$ nm. The two-dimensional density map of the target, showing the holes filled at −50 fs, is presented in Fig. 6c for completeness. Fig. 6d shows the results on proton spectra: The ×1.8 enhancement of the maximum energy with respect to a regular foil, expected when the NHs are preserved, is entirely lost with filled NHs.

Discussion

Our experiment shows that the proton energies achieved with NH targets are similar to those obtained with regular foils of the same thickness. Supported by simulations, we relate this finding to the formation a short-scale length plasma on the target surface, caused by a fraction of uncompressed laser energy that irradiates the target in the last ps before the peak of the pulse. This happens because the DPM is designed to remove the energy of the ASE pedestal, but it becomes ineffective at the high fluences reached in the proximity of the peak. Such

limitation rarely affects experiments on proton acceleration from thin targets, since a short-scale length plasma (with $L < \lambda/10$) is usually considered negligible to the efficiency of vacuum heating[34]. However, our work demonstrates that the observation of energetic protons from both surfaces of nm-thick foils, does not ensure that all types of nanostructures are preserved before the interaction with the relativistic laser pulse.

The simulations accounting for the finite contrast of the laser pulse allowed us to determine that $L_{\mathrm{PIC}} \simeq 25$ nm is detrimental for the energy enhancement expected with NHs of 200 nm diameter. Since we did not measure the plasma scale length produced in the experiment, we now compare L_{PIC} with analytical estimations of the target expansion.

The plasma scale length is calculated as $L_{\mathrm{exp}} = c_s t$, with t the expansion time and $c_s[\mathrm{nm/ps}] = 310(ZT_{e,[\mathrm{keV}]}/A)^{1/2}$ the sound speed for the ion with charge Z, atomic mass A, and electron temperature T_e. To simplify our analysis, we focus our attention on the layer of hydrogen contaminants present on the target surface and on the NH walls, because the protons dominate the dynamics of the plasma in the early stages of its expansion, when the number density of protons is higher than the number density of gold ions, $n_p > n_{\mathrm{Au}^+}$[41]. We expect $L_{\mathrm{exp}}^{\mathrm{H}^+}$ to give an overestimation of the scale length actually produced in the experiment, because the formula assumes that the expansion is sustained by a semi-infinite plasma[36], whereas recent measurements[42] limit the the thickness of the contaminant layers on metallic surfaces to 1–5 nm $< L_{\mathrm{PIC}}$. The expansion of the gold target is therefore essential to produce the plasma that fills the holes. However, a proper estimation of the plasma scale length requires sophisticated assumptions about the average ionisation of the foil in the moments before the interaction with the ultrashort pulse. In the following, we calculate L_{exp} both for the hydrogen plasma produced from the contaminant layer, and for the gold plasma formed by 11-time ionised atoms. This value is chosen[43] considering the charge state of a gold atom caused by field ionisation at a laser intensity of $\sim 10^{15}$ W/cm^2. We reckon that the experimental scale length will be within the range determined by $L_{\mathrm{exp}}^{\mathrm{H}^+}$ and $L_{\mathrm{exp}}^{\mathrm{Au}^{11+}}$.

The electron temperature is given by[36] $T_e[\mathrm{eV}] = 119(10^{-23} n_{e0,[\mathrm{cm}^{-3}]})^{1/12} Z^{1/12} (10^{-15} I_{[\mathrm{W/cm}^2]})^{1/3} (10^{-2} \tau_{[\mathrm{fs}]})^{1/6}$, and it depends on the intensity I that causes the heating during the time span τ. Since the target is irradiated by the ps-shoulder of the pulse, the heating time and the expansion time are considered equivalent, $t = \tau$, and we take the intensity arriving on target at -500 fs as the starting point for our calculation. This is motivated by two reasons: First, the contrast measurement in Fig. 1b clearly shows that at this time the DPM is ineffective; Second, even if target ionisation occurs at a lower intensity (i.e. before -500 fs), electrons heated at later times will catch up with the earlier, slower expanding front, because of their higher temperature. Taking 10^{13} W/cm^2 as lowest threshold for target ionisation, $I = 2 \times 10^{15}$ W/cm^2 at $\tau = -500$ fs represents the mid-point for calculating the expansion velocity during the irradiation by the ps-long shoulder.

For the initial electron density we use respectively the number of ionised hydrogen atoms in water, $n_{e0}^{\mathrm{H}^+} = 6.7 \times 10^{22}\,\mathrm{cm}^{-3} \simeq 40 n_c$, and the electron density of the ionised gold, $n_{e0}^{\mathrm{Au}^{11+}} = 6.5 \times 10^{23}\,\mathrm{cm}^{-3} \simeq 370 n_c$. For the hydrogen plasma, it follows that $T_e^{\mathrm{H}^+} = 190$ eV, $c_s^{\mathrm{H}^+} = 135$ nm/ps and $L_{\mathrm{exp}}^{\mathrm{H}^+} \simeq 70$ nm. For the gold plasma, $T_e^{\mathrm{Au}^{11+}} = 280$ eV, $c_s^{\mathrm{Au}^{11+}} = 40$ nm/ps and $L_{\mathrm{exp}}^{\mathrm{Au}^{11+}} \simeq 20$ nm. We also notice that with the electron temperature rapidly increasing in the last 500 fs, gold atoms with higher ionisation states would have higher sound velocities and produce larger scale lengths.

Despite the order of L_{exp} is below $\lambda/10$, the estimated scale lengths are crucial in relation to the size of the NHs. Compared to L_{PIC} and L_{fill}, the results for L_{exp} support our interpretation that the plasma produced by the ps-long shoulder fills the NHs before the interaction with the ultrashort laser pulse. The overdense plasma removes the additional interaction surface that was made available with the NH walls, and it prevents the electromagnetic field of the incoming pulse from recirculating the electrons around the holes. The result is a reduction both of the number and of the energy of the electrons accelerated during the interaction, hence the suppression of the mechanism for enhanced heating. The experimental results indicate that the filling occurs also with larger NHs, allowing us to infer that $L_{\mathrm{exp}} \simeq 50$ nm, which is the value for L_{fill} when $d = 510$ nm. We can also notice that $L_{\mathrm{exp}} \propto I^{1/6}$, so reducing the intensity on the target by a factor of 100, as done in the experiment by moving away from the laser focus, only decreases the scale length by a factor of 2, which is not enough to prevent the filling of the NHs.

Conclusion

In this work, we tested the efficiency on proton acceleration of ultrathin flat foils perforated with non-periodic distributions of holes of nanometric size. According to numerical simulations with laser pulses with infinite temporal contrast, electrons extracted from the the walls of the NHs and accelerated in the interstices lead to enhanced accelerating fields and high proton energies. However, in our experiment we could not observe any significant difference between the energies measured with NH targets or with regular flat foils. Our explanation, supported by simple analytical estimations and by PIC simulations, is that the laser temporal contrast obtained with a standard double plasma mirror does not prevent the formation of a short-scale plasma that fills the holes prior to the interaction with the relativistically intense laser pulse. It is worth emphasising that such a plasma does not particularly alter the efficiency of vacuum-heating, hence resulting in proton energies of similar magnitude from both surfaces of the foils. In this sense, measuring proton acceleration from the front surface does not allow discriminating the finer conditions of the target surface.

Despite the fact that NH targets do not lead to enhanced proton energies, experimental investigations such as this one remain crucial to assess realistic interaction conditions and to point out the limitations of present target and laser technologies. The study of the heating mechanisms and absorption processes enabled by suitable nanostructures continues to be relevant to identify the key parameters that improve proton acceleration.

But there is further need for target fabrication techniques and laser development to progress hand in hand, as the contrast typically achieved in multi-TW laser installations may yet be a limit for the capabilities of advanced target geometries. As of now, the laser community is striving to deliver PW-class systems with unprecedented contrast both in the ns and in the ps timescale[44–47] , exploiting different techniques to maintain clean pulses from the laser front end, through the amplification chain, and up to plasma mirrors[48]. At the same time, monitoring of on-target plasma formation, with sub-ps temporal resolution, will help correlating the shot-to-shot conditions of the target surface with the results from proton diagnostics, and modelling accurate experimental conditions in the numerical simulations. Further studies of the interplay between target geometry and laser properties will finally open the way to new strategies for the optimisation of proton acceleration, both in the TW and in the PW regime.

Methods

Target fabrication. Ultrathin gold foils with nanoholes (NHs) were manufactured at the Department of Physics of Gothenburg University, using hole-mask colloidal lithography[27]. The main steps of the fabrication are: (1) deposition of a sacrificial layer of Cr (70 nm thick) on a clean glass substrate; (2) deposition of a colloidal solution, containing polystyrene nanospheres with diameter equal to the required nanohole size; (3) deposition of the Au film, with thickness smaller than the nanospheres diameter; (4) tape-stripping of the nanospheres; (5) etching away the Cr layer, rinsing in distilled water and (6) transfer of the perforated film onto the target holder.

This fast and versatile technique allowed to prepare NH targets with different combinations of hole diameter ($d = 230$, 510 nm), filling factor ($\rho = 5$, 15, 25%) and substrate thickness ($t = 120$, 250 nm). The reference Au foils, without holes, were fabricated in the same deposition cycle as the NH targets, by simply skipping the deposition of the nanospheres.

All targets were checked and characterised with scanning electron microscopy after transfer onto the target holder (see Fig. 1). This one, in particular, fitted up to 4 different target types at the same time, allowing to compare their performances in the same experimental cycle.

Experimental setup. The experiment was carried out at the High Power Laser Facility of Lund University (Sweden), whose Ti:Sapphire laser system delivers 35 fs pulses at a central wavelength of 0.8 μm. The Gaussian, P-polarised beam was focused on solid targets by an $f/3$ off-axis parabolic mirror, within a $\sim 2.5\,\mu$m FWHM focal spot. With an incidence angle of 45° and a maximum energy of 350 mJ, the peak intensity on target reached $I \simeq 10^{20}$ W/cm^2.

A double plasma mirror[32] (DPM) allowed irradiating the ultrathin metallic foils without reaching their ionisation threshold ($\sim 10^{13}$ W/cm^2 for Au) with the 100s of ps-long pedestal due to amplified spontaneous emission (ASE). The DPM consists of two glass substrates with an anti-reflective coating, arranged with two parabolic mirrors in a confocal setup. The beam is transmitted through the substrates until the energy deposited in the material is enough to trigger a ionisation cascade. When the electron density finally reaches the critical value at the laser wavelength, the beam is reflected to the re-collimating mirror and transported to the experimental chamber. The fluence of the incoming beam on the dielectric substrates determines the trigger time of the device. A measurement of the laser temporal contrast, obtained with a third-order cross-correlator, is presented in Fig. 1b. Without DPM, the level of the ASE pedestal (at $\ll -100$ ps) is about 10^{-9} times the intensity of the peak of the pulse, while it falls outside the dynamic range of the cross-correlator when the DPM is used. In addition, a contrast enhancement of ~ 3 orders of magnitude is achieved at -2 ps, thus preventing target ionisation until ~ 1 ps before the peak.

Targets were mounted and aligned under vacuum at the position of the laser focus with $\sim 10\,\mu$m accuracy, and the quality of the irradiation site was verified prior to each shot. During the experiment, we also moved the targets along the laser focal axis, in order to illuminate larger areas of the foils without reducing the laser energy delivered both to the DPM and to the target. Given our Rayleigh length $z_R \sim 18\,\mu$m, shifting the target by 50, 100 and 200 μm from the focal plane corresponded to approximately a 3, 6 and 10-time increase of the focal spot radius, hence to lowering the intensity by a factor of 9, 36 and 100.

We measured the energy spectra of the proton beams emitted along the normal direction to both surfaces of the target, front and rear. Protons accelerated from the front, laser-irradiated surface (backward direction, BWD) were detected by a calibrated magnetic spectrometer. The dispersed particles impinged on a scintillator (St. Gobain, BC-408) protected by 12.5 μm of Al foil to filter out spurious light and heavier ions. Protons accelerated from the rear surface of the target (forward direction, FWD), instead, were measured with a calibrated Thomson Parabola spectrometer, employing a micro-channel plate and a phosphor screen as detector.

We also used two Spectralon screens (LabSphere, SRT-99-050) to intercept the laser light that was reflected and transmitted by the target. To prevent damage, the Spectralons were placed at ~ 15 cm distance from the target. An image of each screen was recorded by a dedicated CCD camera provided with neutral-density and 800-nm interferometric filters. The integrated signal was rescaled to take into account all the attenuation factors and different collection angles of the cameras. Then, we compared the signal obtained when irradiating different targets to the one recorded on the transmission Spectralon when no target was in place (blank shots).

Particle-in-cell simulations. Particle-In-Cell (PIC) simulations were performed with the two-dimensional version of the Smilei Code[49], adapting the numerical setup originally published in Ferri et al. (2020) [26].

We used a P-polarised laser pulse, with 0.8 μm wavelength and Gaussian profiles both in space and time, characterised by a FWHM of 2.5 μm and 35 fs, respectively. The energy of 350 mJ corresponded to a normalised potential vector $a_0 = 6.7$ at the centre of the spot. The pulse was focused at 45° of incidence on 100 nm-thick gold foils (11 times ionised, with ion number density $n_{Au^+} = 5.85 \times 10^{22}$ cm^{-3}, 100 macro-particles per cell, per species), coated on both surfaces with a 10 nm-thick proton/electron layer ($n_p = n_e = 1.74 \times 10^{23}$ cm^{-3}, 1000

macro-particles per cell, per species). For the perforated foils, holes with 200 nm diameter and 30% filling factor were randomly distributed on the target surface, following the method described in Ferri et al. [26] The simulation box was $50 \times 56\ \mu m^2$, with spatial steps $\Delta x = \Delta y = 5$ nm and a time step $\Delta t = 11.7$ as.

In the simulations with the pre-formed plasma, the proton/electron layers were given an exponential density profile of the form $n_e = n_{e0} \exp(-s/L)$, s being the distance from the unperturbed target (with $n_{e0} = 11 n_{Au^+} \simeq 370 n_c$) and L the scale length (varied between 0 and 70 nm). The profiles, added to all target surfaces (front, rear, and NH walls) were cut where $n_e = 0.01\ n_c$ to limit the spatial extent of the pre-plasma. The number of macro-particles in the pre-plasma was increased to 200 when working with $L = 10$ nm.

To account for the finite temporal contrast measured in the experiment, we modelled the intensity profile of the laser pulse with a sum of Gaussian functions, so as to describe the ultra-short pulse, the ps shoulder and the earlier ASE pedestal[39,40]. The normalised amplitude A and the width σ (in ps) for each function $A \exp[-t^2/(2\sigma^2)]$ were chosen so that the third-order cross-correlator trace would fit the experimental measurement up to 50 ps before the pulse peak, as shown in Fig. 6b. In detail, $A = 0.5$ and $\sigma = 0.015$ ps for the ultra-short pulse (such that FWHM$= 2\sigma\sqrt{2\log(2)} = 35$ fs), $A = 0.5$ and $\sigma = 0.09$ ps for the shoulder between -500 fs and -1 ps, $A = 10^{-4}$ and $\sigma = 0.35$ ps for the shoulder between -1 fs and -2 ps, $A = 4 \times 10^{-8}$ and $\sigma = 1.5$ ps for the pedestal between -5 and -2 ps, and $A = 10^{-9}$ and $\sigma = 25$ ps for the pedestal before -5 ps. With this profile, the transverse size of the simulation box was increased to 92 μm. We also decreased the peak intensity in order to redistribute the same 350 mJ of laser energy along such a longer pulse. A scaling factor of 3.5 was calculated as the ratio of the areas subtended by the fitted intensity profile and by the ultrashort pulse. As a consequence, $a_0 = 6.7/\sqrt{3.5} = 3.6$. The simulations run from 1 ps before the peak of the pulse, to $t = 250$ fs, when the proton spectra were recorded. Irradiating the targets with the longer laser pulse caused heating and expansion of the foil, for both target types. The expansion of the rear surface, in particular, motivated adding the pre-plasma also on the back of the target, when varying the pre-plasma scale lengths.

Received: 23 October 2020; Accepted: 12 February 2021
Published online: 03 March 2021

References

1. Macchi, A., Borghesi, M. & Passoni, M. Ion acceleration by superintense laser-plasma interaction. *Rev. Mod. Phys.* **85**, 751–793. https://doi.org/10.1103/RevModPhys.85.751 (2013).
2. Daido, H., Nishiuchi, M. & Pirozhkov, A. S. Review of laser-driven ion sources and their applications. *Rep. Progr. Phys.* **75**, 056401. https://doi.org/10.1088/0034-4885/75/5/056401 (2012).
3. Schreiber, J., Bolton, P. R. & Parodi, K. Invited review article: "hands-on" laser-driven ion acceleration: a primer for laser-driven source development and potential applications. *Rev. Sci. Instrum.* **87**, 071101. https://doi.org/10.1063/1.4959198 (2016).
4. Lübcke, A. *et al.* Prospects of target nanostructuring for laser proton acceleration. *Sci. Rep.* **7**, 44030. https://doi.org/10.1038/srep44030 (2017).
5. Prencipe, I. *et al.* Targets for high repetition rate laser facilities: needs, challenges and perspectives. *High Power Laser Sci. Eng.* **5**, e17. https://doi.org/10.1017/hpl.2017.18 (2017).
6. Khaghani, D. *et al.* Enhancing laser-driven proton acceleration by using micro-pillar arrays at high drive energy. *Sci. Rep.* **7**, 11366. https://doi.org/10.1038/s41598-017-11589-z (2017).
7. Dozières, M. *et al.* Optimization of laser-nanowire target interaction to increase the proton acceleration efficiency. *Plasma Phys. Controll. Fus.* **61**, 065016. https://doi.org/10.1088/1361-6587/ab157c (2019).
8. Margarone, D. *et al.* Laser-driven high-energy proton beam with homogeneous spatial profile from a nanosphere target. *Phys. Rev. Spec. Top. Accel. Beams* **18**, 071304. https://doi.org/10.1103/PhysRevSTAB.18.071304 (2015).
9. Passoni, M. *et al.* Toward high-energy laser-driven ion beams: nanostructured double-layer targets. *Phys. Rev. Accel. Beams* **19**, 061301. https://doi.org/10.1103/PhysRevAccelBeams.19.061301 (2016).
10. Bin, J. H. *et al.* Ion acceleration using relativistic pulse shaping in near-critical-density plasmas. *Phys. Rev. Lett.* **115**, 064801. https://doi.org/10.1103/RevModPhys.85.7510 (2015).
11. Andreev, A. *et al.* Relativistic laser nano-plasmonics for effective fast particle production. *Plasma Phys. Controll. Fus.* **58**, 014038. https://doi.org/10.1103/RevModPhys.85.7511 (2016).
12. Ceccotti, T. *et al.* Evidence of resonant surface-wave excitation in the relativistic regime through measurements of proton acceleration from grating targets. *Phys. Rev. Lett.* **111**, 185001. https://doi.org/10.1103/RevModPhys.85.7512 (2013).
13. Klimo, O. *et al.* Short pulse laser interaction with micro-structured targets: simulations of laser absorption and ion acceleration. *N. J. Phys.* **13**, 053028. https://doi.org/10.1103/RevModPhys.85.7513 (2011).
14. Kluge, T. *et al.* High proton energies from cone targets: electron acceleration mechanisms. *N. J. Phys.* **14**, 023038. https://doi.org/10.1103/RevModPhys.85.7514 (2012).
15. D'Humières, E., Brantov, A., Bychenkov, V. Y. & Tikhonchuk, V. T. Optimization of laser-target interaction for proton acceleration. *Phys. Plasmas* **20**, 023103. https://doi.org/10.1103/RevModPhys.85.7515 (2013).
16. Jiang, S., Krygier, A. G., Schumacher, D. W., Akli, K. U. & Freeman, R. R. Effects of front-surface target structures on properties of relativistic laser-plasma electrons. *Phys. Rev. E* **89**, 013106. https://doi.org/10.1103/RevModPhys.85.7516 (2014).
17. Brantov, A. & Bychenkov, V. Y. Laser-triggered proton acceleration from micro-structured thin targets. *Contrib. Plasma Phys.* **53**, 731–735. https://doi.org/10.1103/RevModPhys.85.7517 (2013).
18. Blanco, M., Flores-Arias, M. T., Ruiz, C. & Vranic, M. Table-top laser-based proton acceleration in nanostructured targets. *N. J. Phys.* **19**, 033004. https://doi.org/10.1103/RevModPhys.85.7518 (2017).
19. Fedeli, L. *et al.* Structured targets for advanced laser-driven sources. *Plasma Phys. Controll. Fus.* **60**, 014013. https://doi.org/10.1103/RevModPhys.85.7519 (2018).
20. Nodera, Y. *et al.* Improvement of energy-conversion efficiency from laser to proton beam in a laser-foil interaction. *Phys. Rev. E Stat. Nonlinear Soft Matter Phys.*https://doi.org/10.1088/0034-4885/75/5/05640*10 (2008).*
21. Psikal, J., Grym, J., Stolcova, L. & Proska, J. Hollow target for efficient generation of fast ions by ultrashort laser pulses. *Phys. Plasmas*https://doi.org/10.1088/0034-4885/75/5/05640*11 (2016).*
22. Langhammer, C., Kasemo, B. & Zorić, I. Absorption and scattering of light by Pt, Pd, Ag, and Au nanodisks: absolute cross sections and branching ratios. *J. Chem. Phys.* **126**, 194702. https://doi.org/10.1088/0034-4885/75/5/05640*12* (2007).
23. Chakravarty, U. *et al.* X-ray enhancement in a nanohole target irradiated by intense ultrashort laser pulses. *J. Appl. Phys.* **109**, 053301. https://doi.org/10.1088/0034-4885/75/5/05640*13* (2011).

24. Nishikawa, T. *et al.* Nanohole-array size dependence of soft x-ray generation enhancement from femtosecond-laser-produced plasma. *J. Appl. Phys.* **96**, 7537–7543. https://doi.org/10.1088/0034-4885/75/5/0564014 (2004).
25. Hadjisolomou, P., Bulanov, S. V. & Korn, G. Towards laser ion acceleration with holed targets. *J. Plasma Phys.*https://doi.org/10.1088/0034-4885/75/5/0564015 *(2020).*
26. Ferri, J. *et al.* Enhancement of laser-driven ion acceleration in non-periodic nanostructured targets. *J. Plasma Phys.* **86**, 905860101. https://doi.org/10.1088/0034-4885/75/5/0564016 (2020).
27. Fredriksson, H. *et al.* Hole–Mask colloidal lithography. *Adv. Mater.* **19**, 4297–4302. https://doi.org/10.1088/0034-4885/75/5/056401 7 (2007).
28. Neely, D. *et al.* Enhanced proton beams from ultrathin targets driven by high contrast laser pulses. *Appl. Phys. Lett.* **89**, 021502. https://doi.org/10.1088/0034-4885/75/5/0564018 (2006).
29. Poole, P. L. *et al.* Laser-driven ion acceleration via target normal sheath acceleration in the relativistic transparency regime. *N. J. Phys.* **20**, 013019. https://doi.org/10.1088/0034-4885/75/5/0564019 (2018).
30. Zhou, M. L., Bin, J. H., Haffa, D., Yan, X. Q. & Schreiber, J. The impact of femtosecond pre-pulses on nanometer thin foils for laser-ion acceleration. *Plasma Phys. Controll. Fus.* **59**, 055020. https://doi.org/10.1063/1.4959198 0 (2017).
31. Rödel, C. *et al.* High repetition rate plasma mirror for temporal contrast enhancement of terawatt femtosecond laser pulses by three orders of magnitude. *Appl. Phys. B Lasers Opt.* **103**, 295–302. https://doi.org/10.1063/1.4959198 1 (2011).
32. Dromey, B., Kar, S., Zepf, M. & Foster, P. The plasma mirror: a subpicosecond optical switch for ultrahigh power lasers. *Rev. Sci. Instrum.* **75**, 645–649. https://doi.org/10.1063/1.4959198 2 (2004).
33. Brunel, F. Not-so-resonant, resonant absorption. *Phys. Rev. Lett.* **59**, 52–55. https://doi.org/10.1063/1.4959198 3 (1987).
34. Chopineau, L. *et al.* Identification of coupling mechanisms between ultraintense laser light and dense plasmas. *Phys. Rev. X* **9**, 011050. https://doi.org/10.1063/1.4959198 4 (2019).
35. Ceccotti, T. *et al.* Proton acceleration with high-intensity ultrahigh-contrast laser pulses. *Phys. Rev. Lett.* **99**, 1–4. https://doi.org/10.1063/1.4959198 5 (2007).
36. Gibbon, P. *Short Pulse Laser Interactions with Matter* (Imperial College Press, London, 2005).
37. Flacco, A. *et al.* Dependence on pulse duration and foil thickness in high-contrast-laser proton acceleration. *Phys. Rev. E* **81**, 036405. https://doi.org/10.1063/1.4959198 6 (2010).
38. Psikal, J., Tikhonchuk, V., Limpouch, J., Andreev, A. & Brantov, A. Ion acceleration by femtosecond laser pulses in small multispecies targets. *Phys. Plasmas*https://doi.org/10.1063/1.4959198 7 *(2008).*
39. Shaw, B. H., Steinke, S., Van Tilborg, J. & Leemans, W. P. Reflectance characterization of tape-based plasma mirrors. *Phys. Plasmas* **23**, 063118. https://doi.org/10.1063/1.4959198 8 (2016).
40. Obst, L. *et al.* On-shot characterization of single plasma mirror temporal contrast improvement. *Plasma Phys. Controll. Fus.* **60**, 054007. https://doi.org/10.1063/1.4959198 9 (2018).
41. Scott, G. G. *et al.* Optimization of plasma mirror reflectivity and optical quality using double laser pulses. *N. J. Phys.* **17**, 033027. https://doi.org/10.1038/srep440300 (2015).
42. Lécz, Z., Budai, J., Andreev, A. & Ter-Avetisyan, S. Thickness of natural contaminant layers on metal surfaces and its effects on laser-driven ion acceleration. *Phys. Plasmas*https://doi.org/10.1038/srep440301 *(2020).*
43. Kawahito, D. & Kishimoto, Y. Ionization and acceleration of multiply charged gold ions in solid film irradiated by high intensity laser. *Phys. Plasmas*https://doi.org/10.1038/srep440302 *(2020).*
44. Rus, B. *et al.* ELI-Beamlines laser systems: status and design options. In Hein, J., Korn, G. & Silva, L. O. (eds.) *High-Power, High-Energy, and High-Intensity Laser Technology; and Research Using Extreme Light: Entering New Frontiers with Petawatt-Class Lasers*, vol. 8780, 87801T, https://doi.org/10.1117/12.2021264(SPIE, 2013).
45. Papadopoulos, D. N. *et al.* The Apollon 10 PW laser: experimental and theoretical investigation of the temporal characteristics. *High Power Laser Sci. Eng.*https://doi.org/10.1038/srep440303 *(2016).*
46. Sung, J. H. *et al.* 42 PW, 20 fs Ti:sapphire laser at 01 Hz. *Opt. Lett.* **42**, 2058. https://doi.org/10.1038/srep440304 (2017).
47. Ranc, L. *et al.* Improvement in the temporal contrast in the tens of ps range of the multi-PW Apollon laser front-end. *Opt. Lett.* **45**, 4599. https://doi.org/10.1038/srep440305 (2020).
48. Choi, I. W. *et al.* Highly efficient double plasma mirror producing ultrahigh-contrast multi-petawatt laser pulses. *Opt. Lett.* **45**, 6342. https://doi.org/10.1038/srep440306 (2020).
49. Derouillat, J. *et al.* SMILEI: a collaborative, open-source, multi-purpose particle-in-cell code for plasma simulation. *Comput. Phys. Commun.* **222**, 351–373. https://doi.org/10.1038/srep440307 (2018).

Acknowledgements

The authors acknowledge collaboration with I. Thiele, E. Siminos, L. Gremillet and meaningful discussions with the members of the PLIONA project. We acknowledge financial support by the Swedish Research Council (VR) and by the Knut and Alice Wallenberg Foundation (KAW). This project has also received funding from the European Research Council (ERC) under the European Union's Horizon 2020 research and innovation programme, under Grant Agreement No. 647121. G. C. is forever grateful to S. M. R. Sebbio for her tireless support and for all the encouraging words, for her warm presence even in the darkest of times.

Author contributions

All authors conceived the experiment and discussed its results. E. S. manufactured and characterised the targets, G. C., Al. P. and An. P. conducted the experiment, G. C. and Al. P. analysed the experimental results, J. F. realised the PIC simulations. G. C. wrote the manuscript. Al. P., J. F., T. F. and C.-G. W. reviewed it.

Funding

Open access funding provided by Lund University.

Competing interests

The authors declare no competing interests.

Additional information

Correspondence and requests for materials should be addressed to G.C.

Reprints and permissions information is available at www.nature.com/reprints.

Publisher's note Springer Nature remains neutral with regard to jurisdictional claims in published maps and institutional affiliations.

Paper IV

Effects of pulse chirp on laser-driven proton acceleration

A. Permogorov, G. Cantono, D. Guenot, A. Persson and C.-G. Wahlström
Manuscript in preparation

Effects of pulse chirp on laser-driven proton acceleration

Alexander Permogorov[1,*], Giada Cantono[1], Diego Guenot[1], Anders Persson[1], and Claes-Göran Wahlström[1]

[1]Department of Physics, Lund University, Lund, SE-22100, Sweden
[*]alexander.permogorov@fysik.lth.se

ABSTRACT

Optimisation and reproducibility of beams of protons accelerated from laser-solid interactions, require accurate control of a wide set of variables, concerning both the laser pulse and the target. Among the former ones, the chirp and temporal shape of the pulse reaching the experimental area may vary because of spectral phase modulations acquired along the laser system. Here, we present an experimental study where we investigate the influence of the laser pulse chirp on proton acceleration from ultrathin (10 nm and 100 nm thick) flat foils, while minimising any asymmetry in the pulse temporal shape. The results show a $\pm 10\%$ change in the maximum proton energy depending on the sign of the chirp. This effect is most noticeable from 10 nm-thick target foils, suggesting a chirp-dependent influence of relativistic transparency.

Introduction

Laser-driven ion acceleration has been theoretically and experimentally studied for about two decades now. Due to their unique emittance and brightness, these sources have been suggested for various applications, from ultrafast radiography to hadron therapy and fast ignition in fusion applications, among others[1,2]. In the most practised acceleration scheme, known as Target Normal Sheath Acceleration (TNSA)[3], an intense laser pulse ($I > 10^{18}$ W/cm^2) irradiates a solid target, and it formes a thin, overdense plasma (having an electron density n_e greater than the critical density $n_c = \varepsilon_0 m_e \omega^2 / e^2$, with m_e and e the electron mass and charge, ε_0 the vacuum permittivity and ω the laser frequency). Electrons on the irradiated side of the target gain energy in the laser field, cross the bulk and exit from the rear surface, forming a charged sheath. As a result, the associated strong electrostatic field ($\sim$ TV/m) ionises water and hydrocarbon contaminants present on the target surface and accelerates the ions in the target normal direction.

One of the main challenges towards the use of TNSA-driven beams in real applications is to improve the conversion from the laser energy to the number and energy of the sheath-forming electrons, and consequently to the maximum energy of the accelerated ions[4]. This generally involves altering the electron dynamics at the front surface of the target, by playing either with the target thickness[5] and morphology[6], or with the laser pulse properties (energy[7], duration[8–10], temporal profile[11–18]). Typically, the presence of a controlled amount of pre-plasma (with density rapidly decreasing below the critical value) at the target surface results in more efficient electron heating, as the laser pulse interacts with a larger volume of plasma electrons and resonant or stochastic absorption processes can take place[19,20]. Such a pre-plasma can be produced by irradiating the target with either a tailored pre-pulse[15–18] or by the ns-long pedestal produced by Amplified Spontaneous Emission (ASE) in chiped-pulse-amplification laser systems[13,14]. In both cases, the energy deposited on target and the duration of the pre-plasma expansion determine the density profile for the main laser-plasma interaction. Optimal proton acceleration is achieved when the target is thick enough that the rear surface is not affected by the formation of pre-plasma on the front one[13].

A modification of this approach is to alter the temporal profile of the main pulse itself. Recent numerical[21,22] and experimental[23,24] works have demonstrated that deviations from an ideal Fourier transform-limited pulse can lead to an increase of the cut-off energies of the laser-accelerated protons. However, there are still ambiguities about which pulse shape, and the related absorption process, optimises the proton acceleration. A laser pulse with fast leading edge penetrates through an ultrathin solid plasma, more than a pulse with a slow leading edge, because the higher instantaneous intensity leads to a lower plasma frequency ($\omega_p \propto (m_e \gamma)^{-1/2}$, with the Lorentz factor γ depending on the normalised amplitude of the laser field $a_0 = eE_0/(m_e \omega c)$). This reduces electron heating at the front surface and has a negative effect on proton acceleration[21]. A similar result on electron heating has also been reported for negatively chirped pulses[25]. On the other hand, a laser pulse with a slow leading edge can gently ionise the target and produce a pre-plasma where absorption of the trailing edge is enhanced[23]. Yet it has been suggested that if a pre-plasma is already present, the ponderomotive force associated with the stronger gradients of a fast rising pulse would result in a better absorption and higher proton energies[22]. Finally, a recent experiment in the PW

regime has reported a 40% enhancement of the maximum proton energy for an unchirped, slow rising pulse, further increased to a 2−fold enhancement if combined with a negative chirp[24].

In this article, we present our experimental results on the effects of laser pulse chirp on protons accelerated from sub-μm-thick flat foils. We made sure that the pulse delivered to the target, at high intensity, was symmetric by carefully monitoring its temporal shape. In this way, we attempted to exclude any influence of the pulse shape and focused only on the role of the chirp. We found that the maximum proton energy depends on the sign of the chirp, indicating a more efficient absorption in the case of a positive chirp. The same trend for the proton energies is observed in both forward (FWD) and backward (BWD) target normal directions. However, for the thicker, 100 nm, target, the enhancement in the FWD direction disappeared, suggesting that relativistic laser-induced transparency (RIT) may play a role, in a chirp-dependent way, for the 10 nm-thick foils[21,26–29].

Results

Thin carbon foils of 10 and 100 nm thicknesses were irradiated at 45° incidence by a p-polarised, 350 mJ, 35 fs laser pulse, with a peak intensity at focus of $\sim 6.5 \times 10^{19}$ W/cm^2. Protons accelerated normally to the target surfaces in the FWD direction were detected by a Thomson Parabola spectrometer, and by a dipole magnet spectrometer in the BWD direction. The light transmitted during the interaction along the laser axis was measured with a Spectralon screen. A schematic illustration of the experimental setup is provided in Methods, figure 4.

Crucial to ensuring that the intense laser pulse interacts with a steep, overdense plasma, we employed a double plasma mirror (DPM) to reduce the intensity of the ASE pedestal below the ionisation threshold of the target. Figure 1(a) shows the contrast ratio measured by a third-order cross-correlator, which reaches 10^{-10} on the 100s-of-ps timescale and 10^{-8} at 1 ps before the main pulse. The intensity rapidly increasing in the region of the coherent pedestal (later than −1 ps), can produce a short-scale length pre-plasma that does not hinder efficient electron heating, and short enough to still allow TNSA in the BWD direction[20,30].

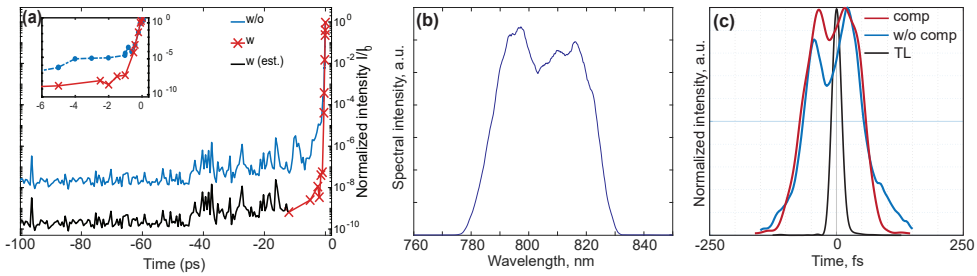

Figure 1. (a) Temporal contrast measured by a third-order cross-correlator, with and without DPM. The inset zooms in the last few ps before the main pulse, after the triggering of the DPM. (b) The spectrum of the laser pulse (c) Temporal shape retrieved by FROG on high-power shots, for a chirped pulse with and without asymmetry compensation and the fully compressed (TL) pulse.

We monitored the shape of the main pulse with a single-shot FROG arranged before the last focusing optic in the experimental chamber. This allowed us to retrieve the temporal shape of the full-energy pulse right before the interaction with the target, and to characterise the pulse in terms of chirp and asymmetry (or skewness).

Chirp is introduced to the laser pulse when it is temporarily stretched, for example, by changing the separation between gratings in the pulse compressor. The chirp parameter can be calculated as $b = \partial^2\varphi(t)/\partial t^2\tau^2$, with $\varphi(t)$ being the temporal phase of the pulse. The value of the chirp parameter is closely related to the pulse duration and to its Fourier transform counterpart – group velocity dispersion (GVD). When the pulse is negatively chirped ($b < 0$), its instantaneous frequency decreases with time. It increases with time in the case of positive chirp ($b > 0$).

A comparison between the fully compressed pulse and chirped ones is presented in figure 1(c). One can note that besides the longer duration, without appropriate corrections the chirped pulse is asymmetric. This is a known consequence of an asymmetric laser spectrum, and imperfections of the optical and mechanical components as well as small alignment errors in the compressor, which means that moving the gratings gives rise to higher order terms in the temporal and corresponding spectral phase[31]. The most relevant spectral phase term is the third order dispersion (TOD, $\propto \partial^3\phi/\partial\omega^3$), which corresponds to the asymmetry of the pulse in the temporal domain. Such asymmetry can be quantified by a skewness parameter[32] $S = m_3/m_2^{3/2}$,

where $m_k = \int_{t_a}^{t_b}(t-t_0)^k I(t)dt / \int_{t_a}^{t_b} I(t)dt$ are the k-th momenta of the pulse, calculated around its centroid t_0. The pulse has a steep leading (or trailing) edge when S is positive (or negative, respectively), while $S = 0$ corresponds to a symmetric pulse.

When the duration of the pulse is changed by moving the gratings of the compressor and the possible changes in the spectral shape are not accounted for, the skewness of the laser pulse varied in the range between -1.0 and 1.8. However, when the sources of potential pulse asymmetry were compensated for, the skewness was reduced to ± 0.3. To restore a symmetric shape, we used an acouto-optic dispersive filter (Dazzler)[33] to introduce a controlled amount of TOD for each grating separation and to make the pulse spectrum symmetric. An example of this compensation for a chirped pulse is given by the red curve in figure 1(c).

Figure 2(a-b) shows the dependence of the maximum proton energy measured in FWD and BWD directions on the laser chirp, for both thicknesses of the foil. Comparable energies along both directions support that the temporal contrast is high enough even for the 10 nm-thick foil to remain essentially unperturbed until the arrival of the main laser pulse (panel (a)). If a pre-plasma is formed at the front surface, its extent is negligible since the acceleration mechanism is similar on both sides of the target[10,30]. The energies obtained from the 10 nm foil are higher than from the 100 nm one (panel (b)), compatibly with the reduced thickness that favours electron recirculation and heating in the laser field[34].

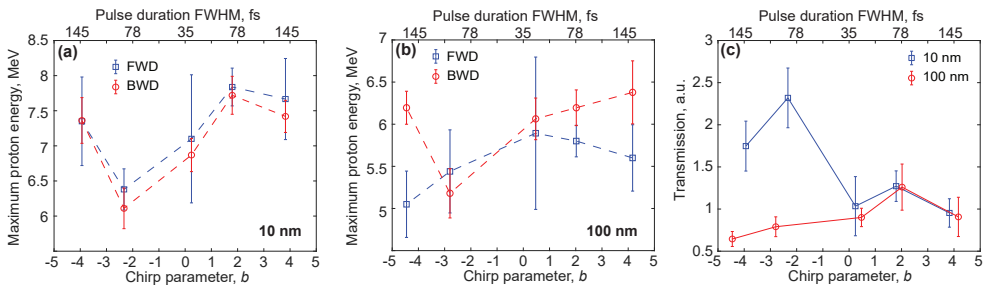

Figure 2. (a, b) Proton cut-off energies in forward (FWD, blue) and backward (BWD, red) directions obtained from 10 nm- (a) and 100 nm-thick (b) carbon foils. (c) Transmitted laser light measured by the Spectralon, for both target thicknesses. In all panels, error bars represent the mean standard error calculated on the average points.

More importantly, from the 10 nm-thick foil we observe a clear effect of the sign of the chirp. On the one hand, the maximum proton energies increase when introducing a positive chirp, with a peak in the FWD direction at 7.8 ± 0.3 MeV, which is 10% more than the average energy measured with a fully-compressed, unchirped pulse ($b = 0$, $\tau \simeq 35$ fs). On the other hand, the FWD cut-off energy decreases by 10% when a moderate negative chirp is used ($b = -3.7$, $\tau \simeq 75$ fs), and it raises again when the chirp is further increased. Remarkably, for the thinnest target the reduction of the laser intensity, due to the increased pulse duration, does not appear to impair the proton acceleration within the range of our scan. While for the 10 nm foil the energies in the BWD direction closely follow those in the FWD direction, we observe a different trend from the 100 nm foil. In this case, the energies show a similar dip for negative chirp, and a small enhancement for positive chirp, only in the BWD direction (corresponding to a -14% and $+2\%$ variation compared to the energy obtained with the unchirped pulse). Along the FWD direction, instead, the maximum energies decrease for longer pulse duration, regardless of the sign of the chirp.

A dependence on both the target thickness and the chirp is also noticeable in the amount of laser light transmitted during the interaction, and presented in figure 2(c). Here, for the thinnest foil we observe a peak in transmission for negative chirp, in correspondence of the same chirp where the proton energy drops. Inversely, the 100 nm foil shows very little variation of the transmitted light for all the investigated values of chirp.

Discussion

Our experimental results show that laser-driven proton beams are affected by the chirp of the laser pulse, and that the maximum energy depends on the sign of the chirp. For extremely thin targets (10 nm), such signature is equally visible in the FWD and BWD direction, and it is found to correlate with the amount of light transmitted through the target. However, the dependence on the chirp of the maximum energy in the FWD direction and of the transmission vanishes when the target thickness is increased to 100 nm. In this section, we discuss possible physical mechanisms that may be related to these experimental observations.

We already mentioned that similar trends of the proton energies in the BWD and FWD direction suggest a similar acceleration mechanism on both sides of the target. From the results with the 10 nm-thick foil, it appears that a more efficient

heating (hence absorption of the laser energy) occurs on the front side when chirp is applied (except for $b = -3.7$). The fact that the chirp-dependence is not observed with the 100 nm-thick foil indicates that the thickness plays a role in the generation of the accelerating sheath at the rear surface of the target. This is more evident when we applied the largest amounts of chirp ($b \approx \pm 4.5$), and we obtained higher energies in the BWD direction compared to those in the FWD direction. There, the combination of electron propagation through the thicker target and of the reduced laser intensity determines the broad, symmetric shape of the blue curve in figure 2(b). On the front side of the target, electrons extracted from the front-surface plasma retain the dependence on the chirp, accelerating the protons with a trend similar to the one observed with the 10 nm-thick foil.

As of the details about how the sign of the chirp affects absorption and proton acceleration from the thinnest target, speculations become more challenging. An important consideration is that the effect of the chirp on the proton energies, although not negligible, is smaller than what is obtained when varying the pulse shape. Previous experiments, in fact, reported large energy enhancements when a pulse with a slow leading edge was used instead of a symmetric one (+70% in Tayyab *et al.*[23], and +40% in Ziegler *et al.*[24]). In the first case, the skewed shape was the result of not compensating the high order terms of the spectral phase when moving the gratings in the compressor. While this caused the effects due to chirp and asymmetry to be entangled, Ziegler *et al.*[24] demonstrated that changing the shape was more effective than changing only the chirp (the proton energy increased by 40% in the first case, versus 20% in the second). For these reasons, a residual asymmetry of the pulse shape of the chirped pulses ($b \approx 4.5$ in figure 1(c)) could dominate over the effect of the chirp.

In addition, working with ultrathin foils pushes the TNSA scheme to the limit of relativistic transparency[26]. It is known that the acceleration of electrons by a relativistically intense laser pulse makes the optical response of the plasma nonlinear. By correcting the electron mass with the Lorentz factor $\gamma = (1 + a_0^2/2)^{0.5}$, the critical density becomes intensity dependent, $n_c \to \gamma n_c$, and the laser pulse can now propagate further inside the plasma, in the region $n_c < n_e < \gamma n_c$. This effect, known as relativistic induced transparency (RIT), becomes important in an ultrathin plasma if $a_0 \gg \pi n_e l/(n_c \lambda)$, being l the target thickness and λ the laser wavelength[35]. This condition indicates that foils below 20 nm of thickness become transparent at laser intensities close to 10^{20} W/cm^2, but additional processes contributing to plasma heating and expansion have been demonstrated to relax this threshold[36,37]. In the experimental context, the target thickness corresponding to the onset of RIT will depend on the angle of incidence, laser polarisation, temporal contrast, etc., giving rise to a space of variables were multiple (hybrid) acceleration mechanisms emerge[26–29]. Numerical simulations have suggested that also the pulse chirp affects the transmission through an ultrathin plasma[21,25,38], even though in some of these studies the changes of the chirp are not sustained by a consistent change of the pulse duration (or of the spectral width).

While the 10 nm-thick foil can become transparent at the intensity used in the experiment, the presence of a chirp-dependent threshold for RIT may explain the dip of the proton energy observed at negative chirp, in conjunction with the peak in transmission measured with the Spectralon. If the foil becomes transparent too early, electrons are not efficiently heated by the most intense part of the laser pulse, and proton acceleration becomes less efficient. A similar effect explains why targets that are too thin undergo RIT and produce low energy protons[27,37]. Note that by calculating the penetration depth of the laser pulse with the formula $l_s = c(\omega_p^2(\gamma)/ - \omega^2(t))^{-1/2}$, where $\omega_p(\gamma)$ is the plasma frequency with the relativistic correction and $\omega(t)$ the pulse instantaneous frequency, depending on the chirp, the difference between the points at $a = \pm 2.7$ is a maximum of only 4%. A better estimation requires evaluating the temporal evolution of the plasma density during the arrival of the pulse, which is even more complex if the target includes some underdense pre-plasma at the irradiated surface[25].

Another aspect worth considering is how the chirp modifies the field that is formed at the front surface of the target by the interference of the incident and reflected laser field[39]. Such a field is a running wave along the target surface, and a standing way along the target normal direction. The resulting electric field is at the base of the "capacitor model" firstly introduced to explain electron heating at the steep surface of an overdense plasma[40]. In recent works, chirped laser pulses have been studied in relation to acceleration mechanisms other than TNSA, which may offer higher conversion efficiencies from laser to ion energies in the newly-available PW regime[41,42]. When the incident laser field is chirped, the nodes of the SW move in time, with the direction determined by the sign of the chirp: toward the target if the chirp is positive, and away from it in the opposite case. It is worth noting that in case of p–polarisation, bunches of electrons cannot be locked in the nodes of the SW and steadily accelerated during the motion of the nodes, as done for example in Magnusson *et al.*[41]. We hence imagine that the motion of the node can only provide a small additional push (or pull) to the electrons that are accelerated by the capacitor field of the SW. Because these electrons are not locked with the nodes, their final direction will depend on the phase they entered the accelerating fields from the plasma[43], and therefore will be either pushed back in the FWD direction, or accelerated away from the target in the BWD direction. This may explain why, if the nodes are moving in a unique direction, the same signature of the chirp is observed along both directions of the target normal axis.

We can calculate the average velocity of the nodes of the SW, for the chirp values used in the experiment. For a gaussian pulse, this is expressed by the first derivative of the instantaneous wavelength, $\partial\lambda/\partial t = B\lambda_0/(1+Bt)^2$, with λ_0 the central wavelength of the pulse and $B = \lambda_0 b/(\pi c \tau^2)$. Then the derivative can be averaged over the duration of the laser pulse. As

shown in figure 3, the variation of the node velocity follows the same trend as the proton energies observed with the 10 nm-thick foil. Clearly, the absolute value of the node velocity cannot correspond to the proton velocity, as their acceleration is first mediated by electrons. Nevertheless, the existence of a similar trend is worth exploring with the assistance of numerical simulations or dedicated experimental works.

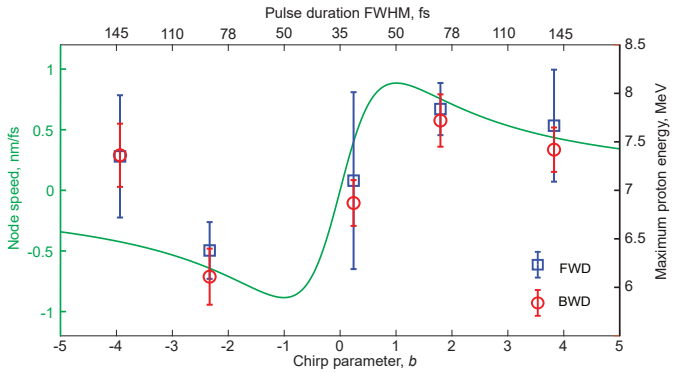

Figure 3. Velocity of the nodes of the SW, as a function of the chirp applied in the experiment (green curve), together with the proton energies detected from the 10 nm-thick foil.

Conclusion

In this study, we focused on the effect of the laser chirp on proton acceleration, by removing higher order terms in the pulse spectral phase originated in the pulse compressor. We found a clear signature of the sign of the chirp on the maximum proton energy and on the transmitted light from a 10 nm-thick foil, while the chirp-dependence was detected only in the BWD-accelerated protons when increasing the target thickness. This indicates that the role of the chirp on energy absorption or electron heating is very subtle, its study requiring ultrathin targets, high temporal contrast and accurate control of the pulse shape over a sub-fs time scale and at high intensity. In this regime, relativistic transparency can take place and give rise to hybrid acceleration mechanisms where unexpected trends in the proton beam energy, profile or direction can arise[26,27]. We have also discussed about the effect of the chip on the standing wave formed in front of the target. The nodes acquire a velocity that depends on the sign of the chirp with the same trend as the measured proton energies. Despite not providing an explanation for the evolution of target absorption or of the accelerating fields, this observation may motivate future numerical and experimental works. In particular, we recommend investigating whether changing the laser polarisation and the angle of incidence would reduce the weight of heating mechanisms that are usual for TNSA, and in turn favour the emerging of other processes. Diagnostics for probing the relativistic transparency, or the emission of proton beams away from the target normal directions, would allow monitoring any transition from TNSA to alternative acceleration mechanisms. Finally, the support from particle-in-cell simulation, able to resolve the details of the electron dynamics during the interaction with the chirped laser pulse, would push the understanding of the underlying physics to a new level.

Methods

Experimental setup

The TW laser at Lund Laser Centre is a chirped pulse amplification system, capable of delivering up to 2 J of energy per laser pulse before compression. The spectrum is centred at a wavelength of 800 nm, with a FWHM of 40 nm. The shortest pulse duration, achieved with a grating-based compressor, is 35 fs. The transport line includes a deformable mirror to remove wavefront aberrations and improve the focusability of the beam. In the present experiment, the p-polarised laser pulse reaching the target had an energy of 350 mJ and it was focused at 45° angle of incidence with a spot size of ~ 3 μm FHWM. The resulting peak intensity was 6.5×10^{19} W/cm^2, corresponding to a normalised field amplitude $a_0 = 6.5$.

We used a double plasma mirror (DPM) to ensure a high temporal contrast of the laser pulse.[44]. The DPM consists of a pair of confocally arranged off-axis parabolic mirrors, with two anti-reflection-coated glass plates placed before and after the focus. The intensity pedestal due to amplified spontaneous emission (ASE) is transmitted through the glass surface, while depositing

energy in it. When the amount of deposited energy has ionised enough electrons so that their density becomes overcritical for the laser wavelength, the remaining pulse is fully reflected. The temporal contrast as measured by a third-order cross-correlator is shown in figure 1(a). It shows that when using the DPM, the intensity of the radiation at -10 ps before the main pulse is reduced by two orders of magnitude. The contrast ratio is better than 10^{-8} until -1 ps before the peak.

The targets consisted of amorphous carbon foils (ACF-Metals) of 10 and 100 nm thickness. Protons accelerated along the normal axis of the target were detected in the FWD direction by a calibrated Thomson Parabola spectrometer, having a micro-channel plate with a phosphor screen as a detector. Protons accelerated in the BWD direction, instead, were dispersed by a dipole magnet and detected by a scintillator screen. The scintillator was wrapped in 12.5 μm-thick Aluminium foil, for light shielding and suppression of the signal from heavier ions. In addition, we placed a scattering Spectralon screen (Labsphere) behind the target, along the laser axis, to measure the intensity of the transmitted laser light. The signal diffused by the screen was detected by a CCD camera equipped with 800 nm-bandpass filter and calibrated neutral density filters. The setup of the experimental chamber is given in figure 4.

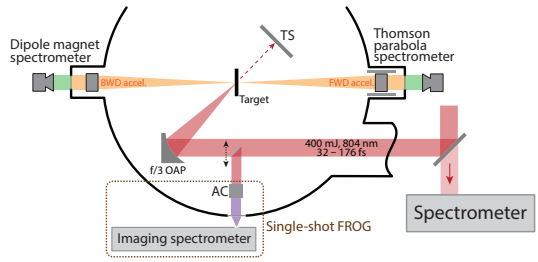

Figure 4. Illustration of the experimental setup. TS denotes the Spectralon screen detecting transmitted laser light, OAP is the focusing off-axis parabola, and AC stands for auto-correlator.

Spectral phase control

Before investigating the effect of the chirp on the accelerated protons, we characterised the shape of the pulse reaching the target with dedicated, high-power shots. To do so, the laser pulse was intercepted before the focusing parabola in the experimental chamber, attenuated by a factor of 35 by reflection from ZnSe and BK-7 wedges and sent to a single-shot second-harmonic autocorrelator (AC in figure 4(a)). Here, the incoming beam was split in two paths with a knife-edge reflective prism, and recombined later on a 300 μm-thick BBO crystal. The non-collinear harmonic signal was then relayed outside the experimental chamber and focused on an imaging spectrometer. The auto-correlator and the spectrometer combined together formed a single-shot FROG[45]. Retrieval of the FROG traces allowed us to reconstruct the temporal and spectral complex envelopes of the laser pulse as it was incident on the target, and to have insight on the necessary adjustments required to make the shape symmetric.

We also used a calibrated, near-infrared spectrometer to measure the laser light leaking from a broad-band dielectric mirror in the experimental chamber. In this way, we could double-check the spectral intensity of the pulse as reconstructed from the FROG trace,and monitor the pulse spectrum in those shots where the FROG was by-passed.

During the experiment we varied the chirp of the pulse, while keeping the temporal shape as symmetric as possible. In the frequency domain, the asymmetry is related to the shape of the spectrum of the laser, and also to the third order term of the Taylor expansion of the spectral phase, third order dispersion (TOD).

We varied the chirp by changing the separation of the gratings in the pulse compressor. With respect to the optimal separation that produces the shortest pulse, increasing the distance between the gratings produces a negatively chirped pulse (instantaneous frequency decreasing with time, $b < 0$). Decreasing the distance produces the opposite effect. The pulse duration increases in both cases, since it is independent from the sign of the chirp ($\tau \propto \sqrt{1+b^2}$). According to the FROG measurements, in the experiment we varied the chirp parameter between ± 4.5, reaching a maximum pulse duration of ~ 140 fs.

We minimised the TOD and adjusted the shape of the spectrum with a Dazzler (Fastlite)[33], a digital programmable acousto-optic modulator that can introduce an arbitrary amount of spectral phase up to the fourth order term in the Taylor expansion, as well as changing the intensity of different parts of the laser spectrum. Since the Dazzler is placed early in the laser system, before amplification and compression, we first measured the pulse TOD with the FROG, and then applied the necessary changes to the pulse spectral phase to minimise the asymmetry. The amount of TOD applied with the Dazzler ranged between ± 15k fs^3, depending on the grating separation. The residual TOD measured by the FROG after shape compensation always

lied between ± 2k fs^3. Note that we restrained from changing the GVD with the Dazzler, because in our case this entailed the risk of damaging the amplifiers later in the laser chain.

References

1. Daido, H., Nishiuchi, M. & Pirozhkov, A. S. Review of laser-driven ion sources and their applications. *Reports on progress physics* **75**, 056401 (2012).
2. Macchi, A., Borghesi, M. & Passoni, M. Ion acceleration by superintense laser-plasma interaction. *Rev. Mod. Phys.* **85**, 751 (2013).
3. Passoni, M., Bertagna, L. & Zani, A. Target normal sheath acceleration: theory, comparison with experiments and future perspectives. *New J. Phys.* **12**, 045012 (2010).
4. Macchi, A. A review of laser-plasma ion acceleration. *arXiv preprint arXiv:1712.06443* (2017).
5. Green, J. S. *et al.* High efficiency proton beam generation through target thickness control in femtosecond laser-plasma interactions. *Appl. Phys. Lett.* **104**, 214101, DOI: 10.1063/1.4879641 (2014). https://doi.org/10.1063/1.4879641.
6. Prencipe, I. *et al.* Targets for high repetition rate laser facilities: needs, challenges and perspectives. *High Power Laser Sci. Eng.* **5**, e17, DOI: 10.1017/hpl.2017.18 (2017).
7. Zeil, K. *et al.* The scaling of proton energies in ultrashort pulse laser plasma acceleration. *New J. Phys.* **12**, 045015, DOI: 10.1088/1367-2630/12/4/045015 (2010).
8. Schreiber, J. *et al.* Analytical model for ion acceleration by high-intensity laser pulses. *Phys. Rev. Lett.* **97**, 045005, DOI: 10.1103/PhysRevLett.97.045005 (2006).
9. Flacco, A. *et al.* Dependence on pulse duration and foil thickness in high-contrast-laser proton acceleration. *Phys. Rev. E* **81**, 036405 (2010).
10. Fourmaux, S. *et al.* Investigation of laser-driven proton acceleration using ultra-short, ultra-intense laser pulses. *Phys. Plasmas* **20**, 013110, DOI: 10.1063/1.4789748 (2013). https://doi.org/10.1063/1.4789748.
11. Nuter, R. *et al.* Influence of a preplasma on electron heating and proton acceleration in ultraintense laser-foil interaction. *J. Appl. Phys.* **104**, 103307, DOI: 10.1063/1.3028274 (2008).
12. Esirkepov, T. Z. *et al.* Prepulse and amplified spontaneous emission effects on the interaction of a petawatt class laser with thin solid targets. *Nucl. Instruments Methods Phys. Res. Sect. A: Accel. Spectrometers, Detect. Assoc. Equip.* **745**, 150–163, DOI: 10.1016/j.nima.2014.01.056 (2014).
13. Kaluza, M. *et al.* Influence of the laser prepulse on proton acceleration in thin-foil experiments. *Phys. review letters* **93**, 045003 (2004).
14. Wang, D. *et al.* Enhanced proton acceleration from an ultrathin target irradiated by laser pulses with plateau ase. *Sci. reports* **8**, 1–7 (2018).
15. Markey, K. *et al.* Spectral enhancement in the double pulse regime of laser proton acceleration. *Phys. Rev. Lett.* **105**, 195008, DOI: 10.1103/PhysRevLett.105.195008 (2010).
16. Brenner, C. M. *et al.* High energy conversion efficiency in laser-proton acceleration by controlling laser-energy deposition onto thin foil targets. *Appl. Phys. Lett.* **104**, 081123, DOI: 10.1063/1.4865812 (2014).
17. Ferri, J. *et al.* Proton acceleration by a pair of successive ultraintense femtosecond laser pulses. *Phys. Plasmas* **25**, 043115, DOI: 10.1063/1.5026391 (2018). https://doi.org/10.1063/1.5026391.
18. Liao, Q. *et al.* Enhanced laser proton acceleration by target ablation on a femtosecond laser system. *Phys. Plasmas* **25**, 063109, DOI: 10.1063/1.5025239 (2018).
19. Mulser, P. & Bauer, D. *High power laser-matter interaction* (Springer, 2010).
20. Chopineau, L. *et al.* Identification of Coupling Mechanisms between Ultraintense Laser Light and Dense Plasmas. *Phys. Rev. X* **9**, 011050, DOI: 10.1103/PhysRevX.9.011050 (2019).
21. Souri, S., Amrollahi, R. & Sadighi-Bonabi, R. Laser-driven proton acceleration enhancement by the optimized intense short laser pulse shape. *Phys. Plasmas* **24**, 053108 (2017).
22. Kumar, S., Gopal, K. & Gupta, D. N. Proton acceleration from overdense plasma target interacting with shaped laser pulses in the presence of preplasmas. *Plasma Phys. Control. Fusion* **61**, 085001 (2019).

23. Tayyab, M., Bagchi, S., Chakera, J., Khan, R. & Naik, P. Effect of temporally modified ultra-short laser pulses on ion acceleration from thin foil targets. *Phys. Plasmas* **25**, 083113 (2018).

24. Ziegler, T. *et al.* Proton beam quality enhancement by spectral phase control of a pw-class laser system. *Sci. Reports* **11**, 1–7 (2021).

25. Yazdani, E., Sadighi-Bonabi, R., Afarideh, H., Riazi, Z. & Hora, H. Electron heating enhancement by frequency-chirped laser pulses. *J. Appl. Phys.* **116**, 103302, DOI: 10.1063/1.4894777 (2014). https://doi.org/10.1063/1.4894777.

26. Poole, P. L. *et al.* Laser-driven ion acceleration via target normal sheath acceleration in the relativistic transparency regime. *New J. Phys.* **20**, 013019, DOI: 10.1088/1367-2630/aa9d47 (2018).

27. Higginson, A. *et al.* Near-100 mev protons via a laser-driven transparency-enhanced hybrid acceleration scheme. *Nat. Commun.* **9**, 724, DOI: 10.1038/s41467-018-03063-9 (2018).

28. Wagner, F. *et al.* Simultaneous observation of angularly separated laser-driven proton beams accelerated via two different mechanisms. *Phys. Plasmas* **22**, 063110, DOI: 10.1063/1.4922661 (2015). https://doi.org/10.1063/1.4922661.

29. Frazer, T. P. *et al.* Enhanced laser intensity and ion acceleration due to self-focusing in relativistically transparent ultrathin targets. *Phys. Rev. Res.* **2**, 042015, DOI: 10.1103/PhysRevResearch.2.042015 (2020).

30. Cantono, G. *et al.* Laser-driven proton acceleration from ultrathin foils with nanoholes. *Sci. Reports* **11**, 1–10 (2021).

31. Squier, J., Barty, C. P., Salin, F., Le Blanc, C. & Kane, S. Use of mismatched grating pairs in chirped-pulse amplification systems. *Appl. optics* **37**, 1638–1641 (1998).

32. Tóth, C. *et al.* Tuning of laser pulse shapes in grating-based compressors for optimal electron acceleration in plasmas. *Opt. letters* **28**, 1823–1825 (2003).

33. Verluise, F., Laude, V., Cheng, Z., Spielmann, C. & Tournois, P. Amplitude and phase control of ultrashort pulses by use of an acousto-optic programmable dispersive filter: pulse compression and shaping. *Opt. Lett.* **25**, 575–577, DOI: 10.1364/OL.25.000575 (2000).

34. Neely, D. *et al.* Enhanced proton beams from ultrathin targets driven by high contrast laser pulses. *Appl. Phys. Lett.* **89**, 021502, DOI: 10.1063/1.2220011 (2006). https://doi.org/10.1063/1.2220011.

35. Vshivkov, V. A., Naumova, N. M., Pegoraro, F. & Bulanov, S. V. Nonlinear electrodynamics of the interaction of ultra-intense laser pulses with a thin foil. *Phys. Plasmas* **5**, 2727–2741, DOI: 10.1063/1.872961 (1998). https://doi.org/10.1063/1.872961.

36. Siminos, E., Grech, M., Skupin, S., Schlegel, T. & Tikhonchuk, V. T. Effect of electron heating on self-induced transparency in relativistic-intensity laser-plasma interactions. *Phys. Rev. E* **86**, 056404, DOI: 10.1103/PhysRevE.86.056404 (2012).

37. Ferri, J. *et al.* Enhancement of laser-driven ion acceleration in non-periodic nanostructured targets. *J. Plasma Phys.* **86** (2020).

38. Vosoughian, H., Riazi, Z., Afarideh, H. & Yazdani, E. Enhancement of proton acceleration by frequency-chirped laser pulse in radiation pressure mechanism. *Phys. Plasmas* **22**, 073110, DOI: 10.1063/1.4926817 (2015). https://doi.org/10.1063/1.4926817.

39. Ferri, J., Siminos, E. & Fülöp, T. Enhanced target normal sheath acceleration using colliding laser pulses. *Commun. Phys.* **2**, 40, DOI: 10.1038/s42005-019-0140-x (2019).

40. Brunel, F. Not-so-resonant, resonant absorption. *Phys. Rev. Lett.* **59**, 52–55, DOI: 10.1103/PhysRevLett.59.52 (1987).

41. Magnusson, J., Mackenroth, F., Marklund, M. & Gonoskov, A. Prospects for laser-driven ion acceleration through controlled displacement of electrons by standing waves. *Phys. Plasmas* **25**, 053109, DOI: 10.1063/1.5026473 (2018). https://doi.org/10.1063/1.5026473.

42. Mackenroth, F. & Bulanov, S. S. Tailored laser pulse chirp to maintain optimum radiation pressure acceleration of ions. *Phys. Plasmas* **26**, 023103, DOI: 10.1063/1.5082604 (2019). https://doi.org/10.1063/1.5082604.

43. May, J. *et al.* Mechanism of generating fast electrons by an intense laser at a steep overdense interface. *Phys. Rev. E* **84**, 025401, DOI: 10.1103/PhysRevE.84.025401 (2011).

44. Dromey, B., Kar, S., Zepf, M. & Foster, P. The plasma mirror—a subpicosecond optical switch for ultrahigh power lasers. *Rev. Sci. Instruments* **75**, 645–649 (2004).

45. DeLong, K., Trebino, R., Hunter, J. & White, W. Frequency-resolved optical gating with the use of second-harmonic generation. *JOSA B* **11**, 2206–2215 (1994).

Acknowledgements

We acknowledge financial support from the Swedish Research Council (VR) and from the Knut and Alice Wallenberg Foundation (KAW).

Author contributions statement

A.P., G.C., and C.G.W. conceived the experiment, A.P., G.C., D.G., and An.Pe. conducted the experiment, A.P. and G.C. analysed the results, G.C. and A.P. wrote the manuscript, all authors reviewed it.

Additional information

The authors declare no competing interests.